

Electronic Thesis and Dissertation Repository

---

12-17-2012 12:00 AM

## Near-Wake Flow Dynamics of a Horizontal Axis Wind Turbine

Pooyan Hashemi Tari, *The University of Western Ontario*

Supervisor: Dr. Horia Hangan, *The University of Western Ontario*

A thesis submitted in partial fulfillment of the requirements for the Doctor of Philosophy degree  
in Civil and Environmental Engineering

© Pooyan Hashemi Tari 2012

Follow this and additional works at: <https://ir.lib.uwo.ca/etd>



Part of the [Aerodynamics and Fluid Mechanics Commons](#)

---

### Recommended Citation

Hashemi Tari, Pooyan, "Near-Wake Flow Dynamics of a Horizontal Axis Wind Turbine" (2012). *Electronic Thesis and Dissertation Repository*. 1033.

<https://ir.lib.uwo.ca/etd/1033>

This Dissertation/Thesis is brought to you for free and open access by Scholarship@Western. It has been accepted for inclusion in Electronic Thesis and Dissertation Repository by an authorized administrator of Scholarship@Western. For more information, please contact [wlsadmin@uwo.ca](mailto:wlsadmin@uwo.ca).

**NEAR-WAKE FLOW DYNAMICS OF A HORIZONTAL AXIS WIND TURBINE**

(Spine title: Near-wake Flow Dynamics of a HAWT)

(Thesis format: Monograph)

by

Pooyan Hashemi Tari

Graduate Program in Civil and Environmental Engineering

A thesis submitted in partial fulfillment  
of the requirements for the degree of  
Doctor of Philosophy

The School of Graduate and Postdoctoral Studies  
The University of Western Ontario  
London, Ontario, Canada

© Pooyan Hashemi Tari 2012

THE UNIVERSITY OF WESTERN ONTARIO  
School of Graduate and Postdoctoral Studies

CERTIFICATE OF EXAMINATION

Supervisor

\_\_\_\_\_  
Dr. Horia Hangan

Co-supervisor

\_\_\_\_\_  
Dr. Kamran Siddiqui

Examiners

\_\_\_\_\_  
Dr. Christian Masson

\_\_\_\_\_  
Dr. Rajiv Varma

\_\_\_\_\_  
Dr. Girma Bitsuamlak

\_\_\_\_\_  
Dr. Ashraf El Damatty

The thesis by

**Pooyan Hashemi Tari**

entitled:

**Near-wake Flow Dynamics of a Horizontal Axis Wind Turbine**

is accepted in partial fulfillment of the  
requirements for the degree of  
Doctor of Philosophy

\_\_\_\_\_  
Date

\_\_\_\_\_  
Chair of the Thesis Examination Board

## ABSTRACT

Experiments have been conducted in a large wind tunnel set-up in order to study the flow structures within the near-wake region of a horizontal axis wind turbine. Particle Image Velocimetry (PIV) has been employed to quantify the mean and turbulent components of the flow field. The measurements have been performed in multiple adjacent horizontal planes in order to cover the area behind the rotor in a large radial interval, at several locations downstream of the rotor. The measurements were phase-locked in order to facilitate the re-construction of the three-dimensional flow field. Acquiring uniform particle distribution in the measurement planes as well as proper calibration for the process of patching the adjacent measurement planes were the major issues influencing the PIV measurements. The results demonstrate the successful implementation of the PIV technique and the associated post-processing to accurately construct the flow field in the near-wake of a HAWT in a large wind tunnel setup.

The mean velocity and turbulence characteristics clearly correlate with the near-wake vortex dynamics and in particular with the helical structure of the flow, formed shortly behind the turbine rotor. The radial velocity is low at the mid section of the blade and increases towards the tip. Close to the rotor and close to the blade tip and root regions the mean and turbulent characteristics of the flow are highly dependent on the azimuth angle of blade due to the tip and root vortices. Further from the rotor, the characteristics of the flow become phase independent. This can be attributed to the breakdown of the vortical structure of the flow, resulting from the turbulent diffusion.

In general, the highest levels of turbulence are observed in shear layer around the tip of the blades, which decrease rapidly downstream. The shear zone grows in the radial direction as the

wake moves axially, resulting in velocity recovery toward the centre of the rotor due to momentum transport.

These findings are important in wind farm studies, where it is essential to determine the region of influence of the wake of each wind turbine, to study the interaction of wind turbines in the farm. The findings are also significant, as they point out that in the far wake region, the turbulent characteristics are independent of azimuth angle of the blade, which suggests the possibility of generating simple and robust wind turbine wake models for wind farm analysis.

In addition to quantification of mean and turbulent velocity field, the capability and limitation of the Blade Element Momentum (BEM) method in predicting axial velocity profiles at the location of the rotor disc has been assessed. For this purpose, the profiles obtained from PIV measurements have been compared with those acquired from the classical BEM method, as well as with the improved method which involves series of corrections, including tip loss, stall delay and thrust coefficient corrections. In general, the comparison shows good qualitative agreement between velocity profiles obtained from PIV measurements and those obtained by BEM method, when the corrections are applied.

Moreover, the PIV results have also been compared with the results obtained from the velocity measurements performed by previous investigators in small wind tunnel set-ups, in order to assess the scaling effects, and in particular the effect of local chord Reynolds number. The tip speed ratio is considered to be similar for all measurement to satisfy the kinematic similarity requirement. The comparison shows that the axial velocity profiles are highly dependent on Reynolds number. This is an important finding in terms of simulating scaled models of wind turbines and wind farms in wind tunnel settings.

**Keywords: horizontal axis wind turbine, wake, wind tunnel experiments, Particle Image Velocimetry, large scale experimental setup, turbulent flow field, phase-locked measurement**

## ACKNOWLEDGEMENTS

I wish to express my profound appreciation and sincere gratitude to my supervisor, Professor Horia M. Hangan, for his thoughtful insights, invaluable advices, stimulating suggestions, as well as his continuous encouragement, patience support and guidance throughout this research.

I gratefully acknowledge my co-supervisor, Professor Kamran Siddiqui, for his support, expert help, thoughtful advices and useful guidelines throughout this research in particular in PIV measurements and data analysis.

I would also like to thank the staff of the Boundary Layer Wind Tunnel Laboratory and the WindEEE Research Institute: Mr. Gerry Dafoe, Mr. Anthony Burggraaf and Mr. Adrian Costache for helping me set up my experiments and also for helping me in technical problems.

My sincere gratitude is also expressed to Wind Energy Strategic Network (WESNet) for providing financial support for this thesis.

I have furthermore to thank my friend, Dr. Arash Naghib Lahouti, for his useful comments and his invaluable help in completing my thesis. I would like to thank my friends and colleagues, Dr. Ashkan Rasouli and Ms. Maryam Refan, for their assistance throughout my experiments and equipment installations, as well as for their practical suggestions. I also wish to thank all of the BLWT graduate students for their assistance in this research.

Lastly, I wish to record my gratitude to my wife, my parents and my brother for their continued love, support and advice and backing me up throughout the four years of my study as a Ph.D. student.

# TABLE OF CONTENTS

<b>CERTIFICATE OF EXAMINATION</b> .....	ii
<b>ABSTRACT</b> .....	iii
<b>ACKNOWLEDGEMENTS</b> .....	vi
<b>LIST OF TABLES</b> .....	x
<b>LIST OF FIGURES</b> .....	xi
<b>NOMENCLATURE</b> .....	xvii
<b>1 Introduction</b> .....	1
1.1 Background.....	1
1.1.1 Governing Parameters.....	3
1.1.2 The Vortical Structure.....	7
1.2 Experimental Approach.....	12
1.2.1 Scaling Effects.....	15
1.2.2 Wind Tunnel Measurements of Full –scale Turbine Rotors.....	17
1.3 Numerical and Aerodynamic Modeling Approaches.....	19
1.3.1 Aerodynamic Modeling Approach.....	20
1.3.1.1 Blade Element Momentum Theory.....	20
1.3.1.2 Actuator Disk/Line model.....	22
1.3.2 Numerical Approach.....	24
1.4 Velocity Measurements using Particle Image Velocimetry (PIV).....	27
1.5 Scope.....	29
<b>2 Preliminary velocity measurements using PIV technique</b> .....	32
2.1 Experimental Set-up.....	32
2.1.1 The three scaled wind turbines.....	33
2.2 Experimental Procedure.....	34
2.2.1 Image processing.....	36
2.3 Results and Discussion.....	40
2.3.1 Axial Velocity.....	41
2.3.2 Radial Velocity.....	43
2.4 Concluding Remarks.....	46
<b>3 Velocity Measurements using PIV Technique- Experimental Procedure</b> .....	48



3.1	Experimental Set-up.....	48
3.1.1	Experimental Equipment.....	50
3.1.1.1	Small Horizontal Axis wind Turbine .....	50
3.1.1.2	Wind Tunnel .....	53
3.1.1.3	Emitter/Detector Device .....	56
3.1.1.4	PIV System .....	56
3.1.1.4.1	Laser.....	57
3.1.1.4.2	Optics.....	57
3.1.1.4.3	Particle Generation System .....	57
3.1.1.4.4	Image Acquisition System .....	61
3.1.1.4.5	Sample Size.....	61
3.1.1.4.6	Error Estimation .....	62
3.2	Experimental Procedure.....	64
3.2.1	Alignment and Calibration.....	67
3.2.2	Phase- lock Technique.....	68
3.2.3	Seeding Process.....	69
3.2.4	Image Acquisition.....	71
3.2.5	Image Processing.....	72
3.2.6	Patching Process.....	75
4	Velocity Measurements using PIV Technique- Results and Discussion.....	76
4.1	The Velocity Field.....	76
4.1.1	Qualitative Analysis of the Velocity Field in the Near-wake Region.....	77
4.1.2	Quantification of the Mean Flow Field in the Near-wake Region.....	82
4.1.2.1	Axial Velocity.....	82
4.1.2.2	Radial Velocity .....	86
4.1.2.3	Comparison with the MEXICO Experiment.....	91
4.1.3	Quantification of the Turbulent Flow Field with the Near-wake Region.....	97
4.1.3.1	Reynolds Stresses and Turbulent Kinetic Energy .....	97
4.2	Comparison with the Blade Element Momentum (BEM) method.....	114
4.3	Scaling effects.....	119
5	Concluding Remarks.....	124
5.1	Conclusions.....	124
5.1.1	Challenges of velocity measurements in the wake of a HAWT in a large wind tunnel set-up.....	124
5.1.2	Mean and Turbulent Flow Field.....	125
5.1.3	Comparison with the Blade Element Momentum (BEM) method.....	128
5.1.4	Scaling Effects.....	129

5.2 Future Work.....	131
REFERENCES.....	132
CURRICULUM VITAE.....	140

## LIST OF TABLES

Table 1-1: The optimal tip speed ratio (Manwell et al., 2002) .....	5
Table 4-1: Specifications of different large- and small-scale wind tunnel set-ups.....	120

## LIST OF FIGURES

Figure 1-1: a) sample of the graph of power coefficient versus tip speed ratio for a high tip speed ratio wind turbine (Manwell et al., 2002). b) Radial profiles of axial velocity as a function of tip speed ratio at  $X=3.34R$  downstream (Vermeulen, 1978). ..... 6

Figure 1-2: a) The process of formation of tip vortex tube on a non-rotational blade b) Schematic of 3D wake structure behind the turbine rotor c) Schematic of top view of the wake structure behind the turbine rotor d) The downstream development of the wake, for high tip speed ratio  $\lambda=7.07$ , obtained from numerical simulation by Troldborg et al. (2009) using iso-surface plots of vorticity. .... 10

Figure 1-3: Development of the wake behind a horizontal axis wind turbine, Numerical Simulation by Troldborg et al. (2009). a)  $\lambda=5.05$ . b)  $\lambda=7.07$ . The figure shows the instantaneous absolute vorticity contours. The light colors are associated to the regions with high vorticity. Figure adapted from Tom (2010) ..... 11

Figure 1-4: Vertical profiles of turbulence intensity at several axial locations downstream of the turbine obtained from wind tunnel measurements and model calculations. The profiles are provided by Smith and Taylor (1991)..... 12

Figure 1-5: Radial profiles of a) normalized axial velocity b) normalized turbulence intensity obtained from PIV measurements performed on a scaled-down model and full scale measurements. The profiles are provided by Whale et al. (1996). Similarity in tip speed ratio was the criterion taken to account to choose the data corresponding to PIV and full scale measurements. The tip speed ratios are  $\lambda_{FS}=3.3$ ,  $\lambda_{PIV}=3.2$  corresponding to full scale and PIV measurements, respectively. .... 17

Figure 1-6: Axial profiles of a) axial velocity and b) radial velocity components obtained from MEXCO measurements. The results are compared with those obtained from numerical simulations (Schepers et al., 2012). .....	19
Figure 1-7: The diagram of the iterative process of the BEM approach (Refan, 2009). $a$ and $a'$ are axial and angular induction factors at a blade element, respectively. $\alpha$ is the incident angle of attack at the corresponding blade element. $C_l$ and $C_d$ are the lift and drag coefficients obtained from the airfoil data at the corresponding blade element. $C_p$ is the power coefficient of the rotor. ....	22
Figure 1-8: Radial profiles of axial velocity for $\lambda=5.8$ and $V_o=10$ m/sec. Dots represents the tip vortex (Sørensen and Shen, 2002).....	24
Figure 1-9: Radial profiles of normalized axial velocity for $\lambda=7.07$ at different axial locations. The results are provided by Troldborg et al. (2007).....	26
Figure 1-10: The overview of the PIV system configuration .....	28
Figure 2-1: Schematic diagram of the experimental set-up.....	33
Figure 2-2: Configuration of the large size wind turbine .....	34
Figure 2-3: a) configuration of the calibration board, b) schematic diagram of the calibration board within the experimental set-up.....	36
Figure 2-4: A sample of a) PIV image b) corresponding binary image c) raw instantaneous velocity field superimposed to the binary image d) corrected velocity field superimposed to the binary image.....	40
Figure 2-5: Contour plots of normalized axial velocity deficit, for the 5 windows covering the area behind the rotor of the large size wind turbine. The windows are not patched.....	42
Figure 2-6: Profiles of axial velocity deficit at three different axial positions. ....	43

Figure 2-7: Contour plots of normalized radial velocity, for the 5 windows covering the area behind the rotor of large size wind turbine. The windows are not patched.....	45
Figure 2-8: Profiles of radial velocity as a function of radius at three different axial positions. .	45
Figure 3-1: Experimental Set-up.....	50
Figure 3-2: Configuration of the upwind three bladed small HAWT rotor in the test set-up.....	51
Figure 3-3: a) Distribution of chord and twist angle in the span-wise direction, b) Airfoil geometry, c) Blade geometry (from Refan, 2009).....	52
Figure 3-4: Power coefficient versus tip speed ratio obtained from experimental and theoretical results provided by Refan and Hangan (2012) .....	53
Figure 3-5: schematic diagram of BLWT 2 at the Boundary Layer Wind Tunnel Laboratory, Western University .....	54
Figure 3-6: Vertical Profiles of normalized mean speed and turbulence intensity. Mean speed is normalized by a reference wind speed of 7.8 m/sec. Turbulence intensity at each height is normalized by the corresponding mean speed.....	55
Figure 3-7: Configuration of the E/D device (top and front view).....	56
Figure 3-8: Configuration of Laskin nozzle-type particle generator.....	58
Figure 3-9: Schematic drawings of the field of PIV measurements .....	66
Figure 3-10: Positioning of the turbine rotor in the reference angular position using the digital inclinometer. ....	69
Figure 3-11: Seed generators within the test set-up.....	71
Figure 3-12: a, b) An Instantaneous image pair, c) Corresponding binary image, d) Corresponding instantaneous velocity field obtained at $X=1.02R$ downstream of turbine in the 4 <sup>th</sup> tile for the blade azimuth angle of 45°. The vector map is superimposed to the contour map of vorticity normalized by the rotor angular velocity. ....	74

Figure 4-1: Streamlines of instantaneous velocity field behind the rotor for  $105\text{cm} < X < 120\text{cm}$  downstream of the turbine. Streamlines are presented for  $30^\circ$  azimuth angle. The streamlines are superimposed to instantaneous contour plots of vorticity normalized by rotational speed of rotor. The location of tip vortex in each instantaneous plot is shown by a red arrow.....79

Figure 4-2: Streamlines of mean velocity field behind the rotor for  $105\text{cm} < X < 120\text{cm}$  downstream of the turbine for eight different azimuth angles of the blade:  $0^\circ$ ,  $15^\circ$ ,  $30^\circ$ ,  $45^\circ$ ,  $60^\circ$ ,  $75^\circ$ ,  $90^\circ$  and  $105^\circ$ . The streamlines are superimposed to contour plots of mean radial velocity normalized by reference wind speed.....81

Figure 4-3: Contours of mean axial velocity deficit ( $-[1-U/U_{\text{ref}}]$ ) behind the rotor for  $0.96 < X/R < 1.08$  for three different azimuth angles of the blade: a)  $45^\circ$ , b)  $60^\circ$ , c)  $90^\circ$  ..... 83

Figure 4-4: Radial profiles of axial velocity deficit for eight azimuth angles of blade a) at  $X=R$ , b) at  $X=2R$ , c) Axial Profiles of axial velocity deficit for four azimuth angles of blade at  $r=1.05R$ .....86

Figure 4-5: Contours of the normalized radial velocity for  $0.96 < X/R < 1.08$  downstream the turbine for three different azimuth angles of the blade: a)  $45^\circ$ , b)  $60^\circ$ , c)  $90^\circ$  ..... 88

Figure 4-6: Radial profiles of normalized radial velocity for eight azimuth angles of blade at a)  $X=R$  b)  $X=2R$ .....89

Figure 4-7: Axial profiles of normalized radial velocity at a)  $r=0.45R$  b)  $r=0.85R$  c)  $r=1.05R$  for eight azimuth angles.....90

Figure 4-8: Comparison of the cross wind profiles of non-dimensional axial velocity deficits (a) and radial velocity (b) from the present experiments and the results obtained from the MEXICO experiment. The tip speed ratios, at which the experiments were performed, are 5.67 and 6.67 for UWO and MEXICO, respectively. .... 93

Figure 4-9: Comparison of the circumferential profiles of non-dimensional (a) axial velocity deficits and (b) radial velocity between the present profiles corresponding to  $X=R$  and the profiles obtained from MEXICO experiment corresponding to  $X=0.2R$ . The tip speed ratios, at which the simulations were performed, are 5.67 and 6.67 for UWO and MEXICO, respectively.....96

Figure 4-10: Contour plots of normalized  $U_{rms}$  at  $0.96 < X/R < 1.08$  downstream of the turbine for eight different azimuth angles of the blade: a)  $0^\circ$ , b)  $15^\circ$ , c)  $30^\circ$ , d)  $45^\circ$ , e)  $60^\circ$ , f)  $75^\circ$ , g)  $90^\circ$ , h)  $105^\circ$ .....100

Figure 4-11: Radial profiles of normalized  $U_{rms}$  at a)  $X=R$  b)  $X=R$  for  $0.4 < r/R < 0.9$  c)  $X=2R$ ..101

Figure 4-12: Contours of normalized  $U_{rms}$  at  $1.96 < X/R < 2.08$  downstream the turbine for: a)  $15^\circ$ , b)  $60^\circ$ , c)  $90^\circ$ . ..... 102

Figure 4-13: Contour plots of normalized  $V_{rms}$  for three azimuth angles of the blade at  $0.96 < X/R < 1.08$  downstream of the turbine: a)  $15^\circ$ , b)  $45^\circ$ , c)  $75^\circ$ ..... 105

Figure 4-14: Radial Profiles of normalized  $V_{rms}$  at  $X=R$  downstream the turbine for eight different azimuth angles of the blade..... 106

Figure 4-15: Contour plots of normalized  $\overline{u'v'}$  for three azimuth angles of the blade at  $0.96 < X/R < 1.08$  downstream of the turbine: a)  $15^\circ$ , b)  $45^\circ$ , c)  $75^\circ$ ..... 107

Figure 4-16: Radial Profile of normalized  $\overline{u'v'}$  at  $X=R$  downstream of the turbine for eight different azimuth angles of the blade..... 108

Figure 4-17: Contour plots of normalized TKE for three azimuth angles of the blade at  $0.96 < X/R < 1.08$  downstream the turbine: a)  $15^\circ$ , b)  $45^\circ$ , c)  $75^\circ$ ..... 111

Figure 4-18: Radial profiles of normalized TKE at  $X=R$  downstream for eight different azimuth angles of blade. .... 112



Figure 4-19: Axial profiles of normalized TKE at a)  $r=1.05R$ , b)  $r=0.85R$ ..... 113

Figure 4-20: Radial profiles of normalized axial velocity acquired from PIV measurements and BEM Modeling. The profiles are obtained at the same tip speed ratio. The profiles acquired from BEM modeling are generated at the location of the rotor disk. .... 118

Figure 4-21: Radial profiles of normalized axial velocity acquired from different experiments presented in Table 4-1, a)  $X < R$  b)  $X > 2R$ ..... .123

## NOMENCLATURE

$A$	Area
$B$	number of Blades
$R$	rotor radius
$C_d$	airfoil drag coefficient
$C_l$	airfoil lift coefficient
$C_p$	power coefficient
$C_T$	thrust coefficient
$a, a'$	axial and angular induction factors
$F$	Prandtl correction factor
$c$	chord length
$r$	radial coordinate
$X$	axial coordinate
$\theta$	azimuth angle of blade
$U_{ref}$	reference wind speed
$U_d$	axial velocity at rotor disc
$U, V$	mean axial and radial velocity
$U_{rms}, V_{rms}$	root mean square of axial and radial velocity
$u, v$	axial and radial components of velocity
$u', v'$	axial and radial components of fluctuating velocity
$\lambda$	tip speed ratio
$\lambda_r$	local tip speed ratio
$Re_c$	local chord Reynolds number
$\omega$	Vorticity
$S_t$	Stokes number

$\tau_p$	response time of a seeding particle
$\tau_f$	characteristic time scale of fluid flow
$\tau_{fD}$	time scale of macroscopic fluid motion
$\tau_{f\Lambda}$	time scale of integral-scale turbulent motions
$\tau_{f\lambda}$	time scale associated with Kolmogorov scale
$\rho$	density of air
$\rho_p$	density of particle
$d_p$	diameter of particle
$\mu$	dynamic viscosity of air
$\nu$	kinematic viscosity of air
$l$	macroscopic characteristic length of the flow
$u_D$	macroscopic characteristic velocity of the flow
$\Lambda$	integral length scale
$h$	smallest geometric length scale in the flow
$\lambda_k$	Kolmogorov length scale
$u_\lambda$	Kolmogorov velocity scales
$\varepsilon$	turbulent dissipation rate
$k$	Turbulent Kinetic Energy (TKE)
$n$	sample size
$\sigma_x$	standard deviation of velocity
$e$	maximum allowed error

# 1 Introduction

## 1.1 Background

The need for renewable energy sources to lessen dependence on hydrocarbons and reduce carbon dioxide (CO<sub>2</sub>) emissions is becoming increasingly urgent because of high concerns in regard to the oil and gas supply security and climate change. In this regard, wind energy is considered as one of the cleanest renewable power sources in the world. In 2008, wind energy provided only approximately 1.0% of total U.S.A. electricity generation. However, recently a goal has been defined by the U.S. Department of Energy (DoE) to meet the target of 20 percent of U.S.A. total electricity generation from wind energy by 2030. To achieve this goal, it is estimated that 300 gigawatts capacity is needed based on the total wind power capacity in U.S.A. (Schreck et al., 2008). In addition, similar to DoE, the Canadian Wind Energy Association (CanWEA) has set-up a strategic vision to ensure wind energy supplies 20 percent of the country's demand by 2025 (CanWEA., 2008). It should be taken in account that in order to achieve this capacity, the number of the typical power generation of 2.0 MW wind turbine that need to be installed in onshore wind farms is in the order of 100,000. Therefore, fluid dynamics of the wake, micro-siting and array effects of wind turbines can be identified as significant research topics needed for wind resource characterization and wind power generation (Schreck et al., 2008).

The majority of the wind turbines today in use are horizontal axis wind turbines (i.e. horizontal main shaft) with one, two or three blades. Hence, most of the recent studies are focused on this type of turbines. Behind the HAWT, a wake is formed. This rotating wake is slightly larger in diameter than the turbine and it becomes broader as the wake trails downstream. The wake is characterized by reduced wind speeds and increased levels of turbulence (Manwell et al., 2002;

Burton et al., 2001). Therefore, the study of the rotating wakes behind horizontal axis wind turbines is of ultimate importance in order to minimize power losses in wind farms due to interference effects. In addition, such a study can also be of interest from the point of view of fundamental fluid dynamics research due to the strong three-dimensional features and the complexity arising from unsteadiness and large levels of turbulence.

From the point of view of spatial structure of the flow, the wake of a horizontal axis wind turbine can be divided into two separate regions: near wake and far wake. The near wake region, which is the subject of the present study, is approximately one diameter downstream of the turbine (Vermeer et al., 2003). The far wake region is the region downstream the near-wake region. The flow structure within the far wake region can be considered independent of the blade geometry and therefore it is Re independent (Vermeer et al., 2003). The near wake flow field, however, is influenced by the rotor angular velocity and the geometry of the blade. The blade passage causes upstream flow retardation and forces the air passing through the rotor to rotate in the opposite direction. In addition, the blades generate tip vortices which significantly influence the wind turbine aerodynamics and can be considered as an important source of noise generation and blade vibration (Massouh and Dobrev, 2007).

Flow characteristics of the turbine wake are initiated in the near-wake region and convected downstream, in the far wake (Vermeer et al., 2003). In particular, in this region, near wake, the turbulence energy is generated due to the large velocity gradient in the annular shear zone separating the inner core of the wake from the ambient flow (Crespo et al. 1996). The turbulent wake of the upstream wind turbines in a wind farm can cause dynamic loads for downstream wind turbines. This can reduce the lifetime of the turbine rotors. In addition, the downstream turbines are subjected to lower velocity wind resulting in the decrease of power production.

Hence, comprehensive information of the flow field in this region including mean flow characteristics, vortical flow structure and turbulence characteristics can be used to improve the design of the rotor and the blade geometry, consequently increasing the turbine efficiency and also to improve wind turbine wake models used in wind farm design.

### 1.1.1 Governing Parameters

The tip speed ratio is the non-dimensional parameter which characterizes the kinematics of the wake development. This ratio is the relationship between angular velocity of the rotor and the reference wind speed. The ratio is computed using the relation,  $\lambda = \frac{\Omega R}{U_{ref}}$  where  $\Omega$  is the rotational speed of the rotor,  $R$  is the radius of the rotor and  $U_{ref}$  is the free stream wind velocity. The tip speed ratio is an influential parameter in regard to power generation. For slow rotation of the rotor, the wind can pass undisturbed through the gaps between the blades. On the other hand, for high rotational speed, the rotor acts as a solid disk. Therefore, this ratio need be adjusted in order to obtain optimum rotor efficiency. For a given rotor, the optimum speed ratio is a function of the number of the blades, displayed in Table 1-1 (Manwell et al., 2002). It can be observed that the larger the number of blades, the slower the wind turbine needs to rotate for optimal efficiency. Figure 1-1 (a) displays a typical graph of power coefficient versus tip speed ratio for a three bladed horizontal axis wind turbine. The peak of the curve corresponds to the optimal ratio. In theory, the maximum achievable value of power coefficient is equal to  $C_p = 0.593$ , known as Betz limit (Betz, 1919), for the case of an ideal wind turbine. The limit occurs when the derivative of the power coefficient obtained from linear momentum theory is equal to zero (Burton et al., 2001). At off-design conditions, lower tip speed ratios and higher tip speed ratios, the power coefficient decreases. For lower tip speed ratios, airfoil angles of attack are high

leading to stall conditions. At high tip speed ratios, the axial induction factor is very high and angles of attack are small and therefore, drag begins to predominate. Note that the axial induction factor,  $a$ , is the fractional reduction in axial wind speed between the upstream flow and the plane of the rotor disc and is defined as follows:

$$a = \left(1 - \frac{U_d}{U_{ref}}\right) \quad 1.1$$

where,  $U_d$  is the axial velocity at the rotor disc.

Besides aerodynamic forces and power coefficient, the tip speed ratio indicates the flow structure of the turbine wake, since mean as well as turbulent components of the flow are highly influenced by this ratio. Figure 1-1 (b) shows the radial profiles of axial velocity as a function of tip speed ratio. It can be seen that in the mid-section of the blade, the axial velocity deficit increases as the ratio increases (see also Krogstad and Adaramola, 2012). The reason can be attributed to the fact that for higher tip speed ratios, the wind turbine behaves more like a rotating disc, and thus the decrease in axial velocity at the central part of the rotor is higher.

One of the crucial parameters affecting the rotor performance as well as the near-wake flow structure is Reynolds number, computed using relation,  $Re_c = \frac{c}{\nu} \cdot \sqrt{U_{ref}^2 + (\Omega r)^2}$  where,  $Re_c$  is the local chord Reynolds number,  $c$  is the local chord length and  $r$  is the local radius of the blade. The Reynolds number is indication of the state of the boundary layer flow over the modeled blade, in particular regarding the stall angle and turbulent transition. Therefore, the flow structure within the near-wake region can be influenced by the variation of Reynolds number. However, one can assume that the effect of the Reynolds number is negligible in the far wake (Whale et al., 1996). The Reynolds number of most of the wind tunnel measurements does not exceed 300,000 (Vermeer et al., 2003), which is lower than typical full-scale Reynolds number of a typical

HAWT which is in the range of  $5 \times 10^5$  and  $10 \times 10^6$  (Manwell et al., 2003). This causes scaling effects which will be discussed later in section 1.2.1.

Number of blades	Optimal tip speed ratio
8-24	1
6-12	2
3-6	3
3-4	4
1-3	>4

Table 1-1: The optimal tip speed ratio (Manwell et al., 2002)



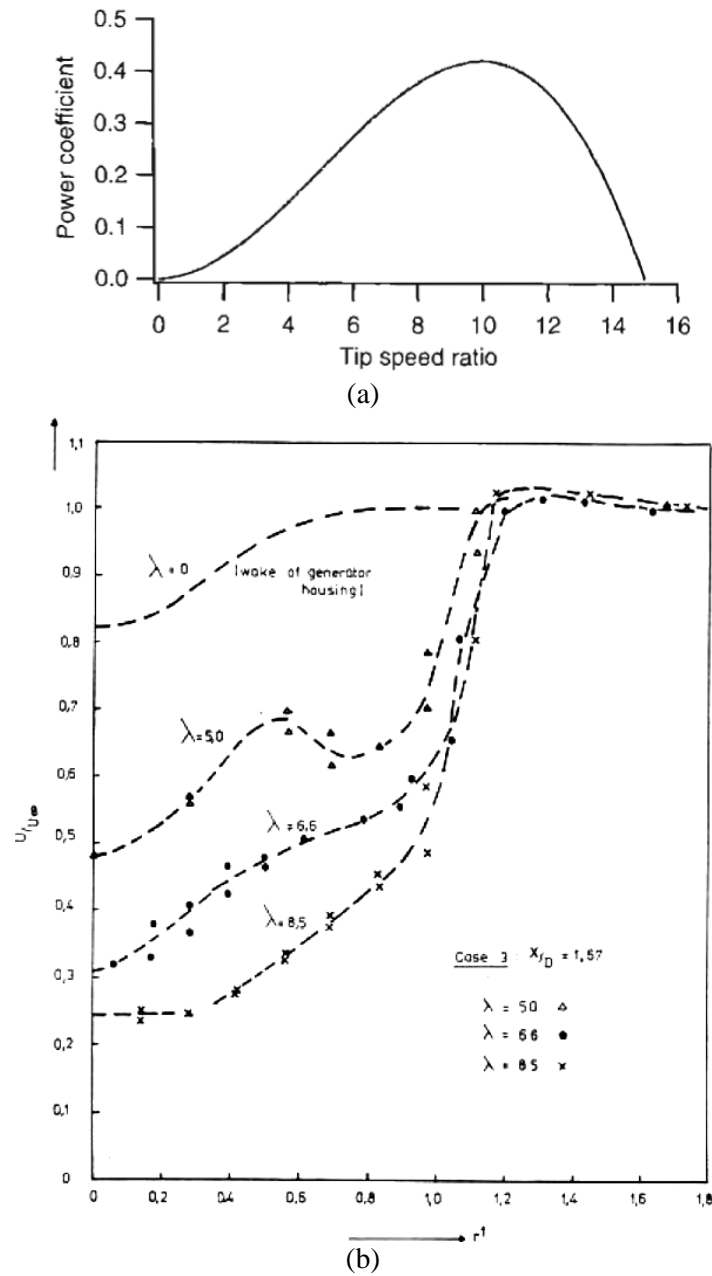


Figure 1-1: a) sample of the graph of power coefficient versus tip speed ratio for a high tip speed ratio wind turbine (Manwell et al., 2002). b) Radial profiles of axial velocity as a function of tip speed ratio at  $X=3.34R$  downstream (Vermeulen, 1978).

### 1.1.2 The Vortical Structure

The near wake region is characterized by a vortex structure resulting from the interaction between the upstream flow and the vorticity sheets generated at the blades and convected downstream. Schematics of this wake vortex topology are presented in Figure 1-2. In general, the trailing vorticity results from the variation of the circulation along a typical blade with finite span. The location at which the circulation is forced to zero indicates the termination of the vortex sheets, which occurs at the root and tip of each blade in case of wind turbine (Whale, 2000). The vortex sheets are trailing downstream in a helical pattern. These vortex sheets tend to roll up, shortly downstream of the rotor (see Figure 1-2 (a)). According to Figure 1-2 (b) and (c), two major vortex tubes can be observed originated from the blade: the vortex helix from the blade tips and from the roots with the helical motion in the reversed direction of the rotation of the rotor (Schepers et al., 2012). The inclination angle of the helical trajectories is a function of the tip speed ratio. For high tip speed ratios, the inclination angle of the vortex tube is small and the layer, encompassing the tip vortices, can be considered as an annular shear zone separating the flow within the wake from the ambient flow (Gomez et al., 2005; Vermeer et al., 2003; Grant and Parkin, 2000). Figure 1-2 (d) displays the formation of the annular shear zone downstream of the turbine, for the case of high tip speed ratio.

The tip speed ratio also determines how the helical trajectories of tip and root vortices convect downstream (Whale et al., 2000; Troldborg et al., 2009). For low tip speed ratios, the helical vortex trajectories survive longer downstream distances due to the rapid wake convection by the free stream flow (see Figure 1-3 (a)). However, for high tip speed ratios, the vortex structure survives only limited distances downstream (Fletcher and Brown, 2010). In turbulent wake, related to high tip speed ratios, the vorticity squeezes within the shear layer and causes the tip

and root vortices to break down into smaller eddies (see Figure 1-2 (d) and Figure 1-3 (b)). This also causes the wake contraction happening in 3-5 rotor radii downstream of the turbine (Troldborg et al., 2009; Whale et al., 2000; Whale and Anderson, 1993).

Two main mechanisms drive the wake structure downstream, convection and turbulent mixing (Vermeer et al., 2003). Most of turbulence generation within the wake occurs in the near wake region within the annular shear layer where the flow is dominated by the vortex structure with large velocity gradients (Vermeer et al., 2003).

Figure 1-4 displays the vertical profiles of turbulence intensities obtained from wind tunnel measurements and model calculations at several axial locations downstream of the rotor (Smith and Taylor, 1991). The tip speed ratio at which the profiles are obtained is  $\lambda=4.0$ . It can be observed that closer to the rotor, the profiles have two peaks (at upper and lower parts of the profiles) within the shear zone which are associated to tip vortex structure. The peaks are not symmetric with respect to the rotor axis due to the asymmetry of the inflow resulting from upstream boundary layer. As the wake convects downstream, it can be seen that the shear layer diffuses while the maximum only remains at the upper part. In other words, the location of maximum turbulence intensity is “remembered” by the flow downstream. This behavior has been also found by previous investigations including field measurements (Magnusson et al., 1996; whale, 1996; Helmis et al., 1995; Papadopoulos et al., 1995; Hojstrup, 1990) and numerical simulation using RANS (Crespo et al., 1996; Kasmi and Masson, 2008) and LES (Jimenez et al., 2007). Since most of the aforementioned results are for axial distances larger than (or equal to)  $1D$ , it can be inferred that in the near-wake,  $X < D$ , the turbulent behavior of the flow is largely dominated by the vortical flow structure corresponding to the blade tip region compared to the root region and hub area.

The shear layer grows as it moves axially downstream until it reaches to the axis of the wake at a certain axial location (2 to 5 rotor diameter (Vermeer et al., 2003)) at which the wake is completely developed. This growth is mainly resulted from the turbulent diffusion in the shear layer (Vermeer et al., 2003; Crespo and Hernandez, 1996). Turbulent diffusive forces are mostly associated to the Reynolds stresses which are much larger compared to the molecular forces within the turbine wake (Sanderse et al., 2011). Figure 1-2 (c) shows the manner at which the shear layer thickens causing downstream wake development and wake expansion. As the wake convects downstream, the turbulent kinetic energy decreases, although the maximum values of turbulent components still occur in the annular shear layer (Vermeer et al., 2003).

The schematic of the wake vortex topology, presented in Figure 1-2 ((b), (c)), will serve as the underlying structure for the discussion of the mean and turbulent wake field results in chapter four.

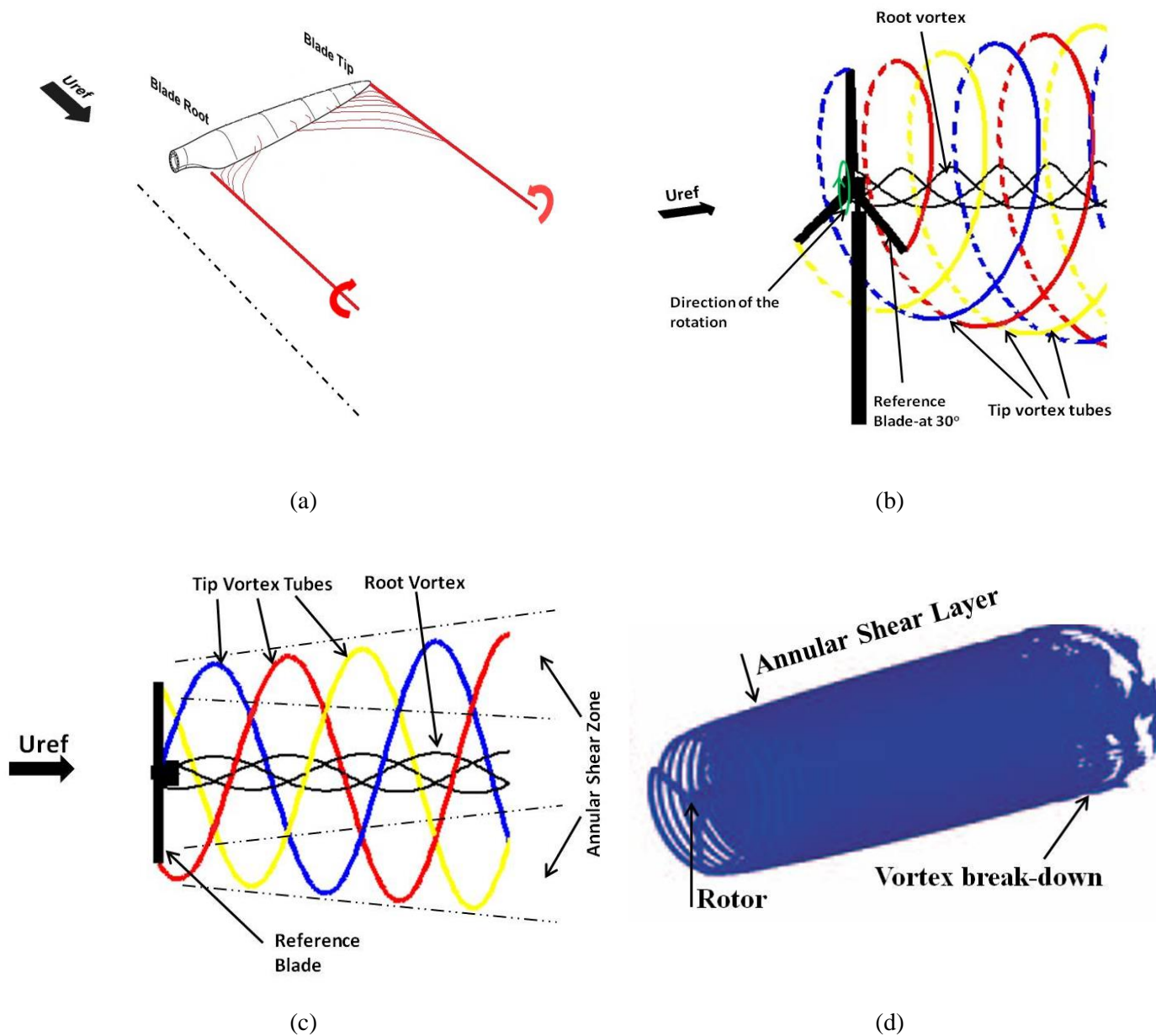
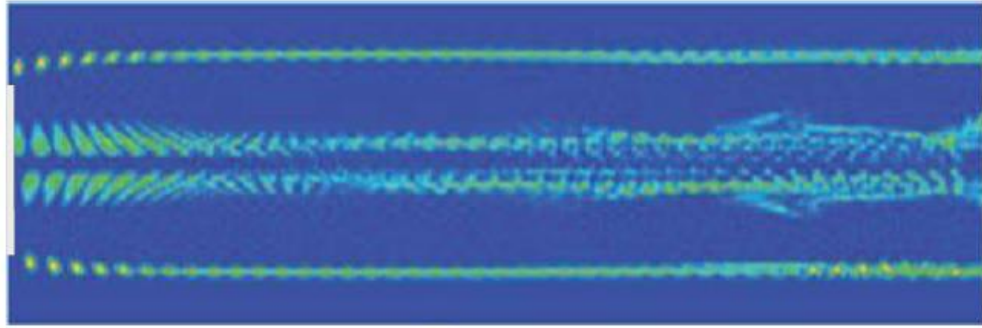
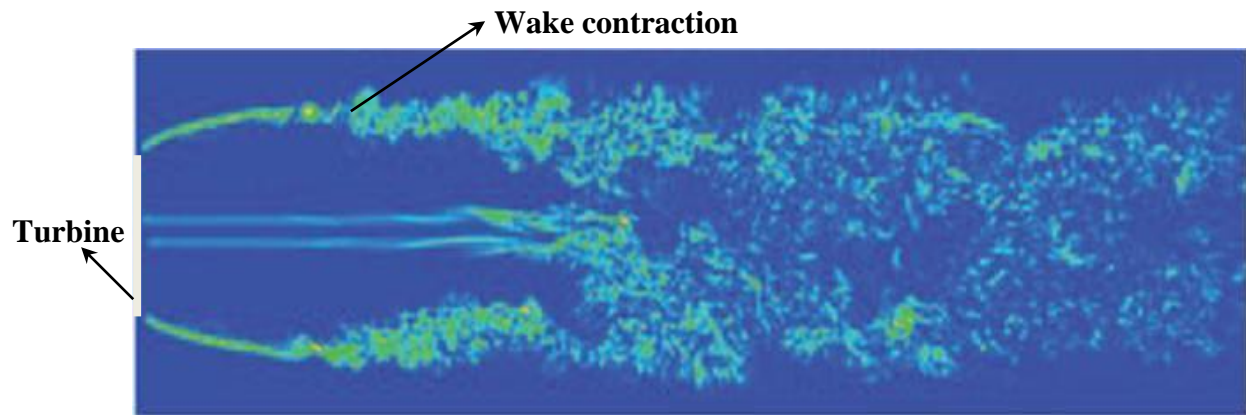


Figure 1-2: a) The process of formation of tip vortex tube on a non-rotational blade b) Schematic of 3D wake structure behind the turbine rotor c) Schematic of top view of the wake structure behind the turbine rotor d)

The downstream development of the wake, for high tip speed ratio  $\lambda=7.07$ , obtained from numerical simulation by Troldborg et al. (2009) using iso-surface plots of vorticity.



(a)



(b)

Figure 1-3: Development of the wake behind a horizontal axis wind turbine, Numerical Simulation by Troldborg et al. (2009). a)  $\lambda = 5.05$ . b)  $\lambda = 7.07$ . The figure shows the instantaneous absolute vorticity contours. The light colors are associated to the regions with high vorticity. Figure adapted from Tom

(2010)

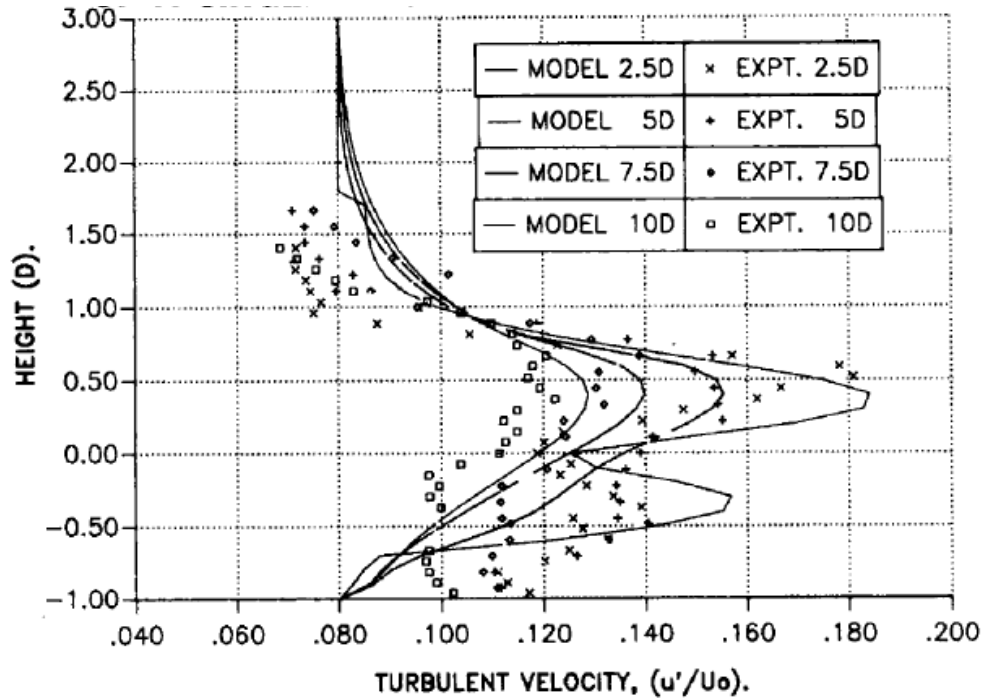


Figure 1-4: Vertical profiles of turbulence intensity at several axial locations downstream of the turbine obtained from wind tunnel measurements and model calculations. The profiles are provided by Smith and Taylor (1991).

## 1.2 Experimental Approach

A number of experimental investigations have been previously carried out to quantify the flow field within the wake region including field tests and wind tunnel experiments. Wind tunnel measurements have the advantage of repeatability with experiments being performed under controlled test conditions. On the other hand, experiments performed in most wind tunnel facilities have the following limitations:

- The presence of the atmospheric boundary layer (ABL): in most wind tunnel measurements, the turbine is exposed to uniform upstream flow. However, actual wind turbines in fields are exposed to the upstream ABL.

- Upstream turbulence levels: in most wind tunnel measurements, the upstream turbulence levels are smaller compared to the field situation.
- Blockage: for actual turbines in fields, the wake can expand freely. However in wind tunnel measurements, the walls surrounding the modeled turbine can influence the wake flow, in particular they can disturb the expansion of the wake which can affect the performance of the rotor.

In addition most of the wind tunnel studies were performed at relatively low Reynolds numbers (lower than the full scale Reynolds number by a factor of 100 to 1000). A detailed overview of these studies can be found in Vermeer et al. (2003). Various techniques, such as flow visualizations, hot-wire anemometry, LDA (Laser Doppler Anemometry) and PIV (Particle Image Velocimetry) have been implemented for several small wind/water tunnel studies, where the model wind turbine rotor diameter ranges between 20 cm and 1.2 m.

Grant et al. (1991, 1998) used PIV to track the tip vortices at radial positions behind the rotor, and to determine the vortex convection downstream. Their results are mostly related to quantifying the tip vortex structure, rather than determination of the mean and turbulent components of the flow. Krogstad and Adaramola (2012) performed velocity measurements using Pitot-static tube in the wake of a small horizontal axis wind turbine with a diameter of 0.90 m. They have analyzed the effect of the tip speed ratio on the average axial velocity profiles at different axial locations downstream of the turbine. The focus of their measurements was only on the mean flow field at axial distances larger than one diameter which is almost out of the near wake region. Tom (2010) experimentally investigated the mean and turbulent flow fields in the near wake region of a model horizontal axis wind turbine (HAWT) with 0.15 m rotor diameter, using PIV. The tip speed ratio ( $\lambda$ ) ranged from 3.5-4.25. The velocity fields were obtained in



horizontal planes at three vertical positions to study the wake effects due to blades along, support tower and blades, and tower alone. The axial extend of the measurement region was between  $0.15 D$  upstream to  $0.7 D$  downstream. Phase-averaging was conducted based on rotor's angular configuration through an in-house algorithm. The results showed flow acceleration adjacent to individual blades, and localized region of low momentum due to flow separation. The enhancement of Reynolds stress was observed immediately downstream of blades and tower, which was argued as the indicator of enhanced turbulent kinetic energy (TKE) production.

PIV experiments were carried out on a two-bladed turbine model with the rotor diameter of 1.25 m by Xiao et al. (2011). The measurements were performed in vertical planes covering the near-wake region immediately behind the turbine in the axial direction. The study was focused on establishing a database of the initiation and development of the tip vortices. Therefore, no comprehensive information regarding mean and turbulent characteristics of the flow was provided. Also note that the turbine used by Xiao et al. (2011) is a two bladed turbine which is less conventional compared to the three bladed turbines.

Yang et al. (2011) and Dobrev et al. (2008) conducted flow field measurements using PIV technique to quantify the development of the turbulent vortex and flow structures in the wake of small wind turbine models with rotor diameters of 0.5m and 0.127m, respectively. They also reconstructed the flow field immediately downstream of the rotor. Chamorro et al. (2012) provided a scale-by-scale energetic description of the flow at various locations downwind of the turbine in a small wind tunnel set-up using hot wire anemometer.

The overall drawback of the abovementioned experiments is that they are mostly conducted at relatively low Reynolds numbers compared to the full scale phenomena which consequently

results in scaling effects (Vermeer et al., 2003; Whale et al., 1997). These effects will be discussed in the next sub-section.

### **1.2.1 Scaling Effects**

One of the main issues in wind tunnel measurements, which have the advantage of controlled flow conditions, are the scaling effects. There are three types of scaling: geometric scaling, kinematic scaling and dynamic scaling. The experimental simulation can represent the full-scale phenomena if the similarity is achieved in all abovementioned scaling. Since most of typical wind tunnels have the limitation of size, the modeled wind turbine is scaled down from a full-scale rotor. The geometric scaling is the ratio between dimensions. Hence, the geometric similarity is achievable if the geometric ratios between different dimensions of the turbine are set to be equal. The kinematic scaling, the ratio between the velocities, can be obtained in a wind tunnel set-up by equalizing the ratios of velocities. In the case of a wind turbine, this can be satisfied by setting the tip speed ratio of the model equal to the full-scale rotor.

The similarity in dynamic scaling, the ratio between forces, is achievable by setting Reynolds numbers to be equal. However, due to the small size of the typical modeled turbines (smaller than full-scale turbine by a factor of 100 to 1000), as well as the limitation of achievable wind speed in most wind tunnel facilities, the similarity in Reynolds number cannot be satisfied, resulting in scaling effects.

Whale et al. (1996) performed PIV measurements within the near-wake region behind a small horizontal axis wind turbine. They compared the mean velocity and turbulence characteristics of the scaled-model flow against the experimental data provided by full-scale measurements in the field. The scaled-model was a replica model from the actual turbine at the approximately 1/100 scale. The Reynolds number at which the PIV measurements were conducted is lower than the

full scale flow by a factor of 1000. The data obtained from PIV tests and full scale measurements were chosen based on the similarity in tip speed ratios. Hence, it was assured that the kinematic scaling is satisfied and thus Reynolds number is the only influential parameter.

Figure 1-5 displays the radial profiles of normalized axial velocity and turbulence intensity acquired from PIV tests and full scale data. The tip speed ratios at which the profiles are acquired are  $\lambda_{FS}=3.3$ ,  $\lambda_{PIV}=3.2$  corresponding to PIV and full scale measurements, respectively. It can be seen that the shape of the profiles obtained from PIV tests and full scale measurements are different. For axial velocity, the full scale profiles are wider and more homogenous in the middle part of the wake compared to the PIV profiles (see Figure 1-5 (a)). For turbulent intensity, especially in the wake center, the profiles show a better agreement in trend, though not in magnitude (see Figure 1-5 (b)). Overall the profiles of turbulence intensities do not match well. According to Whale et al. (1996), the reason can be attributed to scaling effects, particularly the difference in Reynolds numbers, and the meandering of the full scale wake.

It can be inferred that the shortcoming of the characterization of turbine wake in small wind tunnel set-ups, is the scaling effects, mostly associated to the difference in Reynolds numbers between the wind tunnel tests and full scale measurements. The scaling effects will be quantitatively discussed in chapter four (see 4.3).

On the other hand, full-scale experiments, mostly field testing, have higher measurement uncertainties due to the wind shear, turbulence, and upstream wind conditions in both direction and magnitude (Vermeer et al., 2003). Therefore, a more reliable and accurate approach is to characterize the wake field of large scale turbine rotors through wind tunnel measurements. However, this approach is very expensive due to the cost of the corresponding model as well as the need for a large wind tunnel facility in order to reduce the blockage effects. Only two such

experiments have been conducted so far to measure the wake flow region. The specifics of these experiments are presented in the next section.

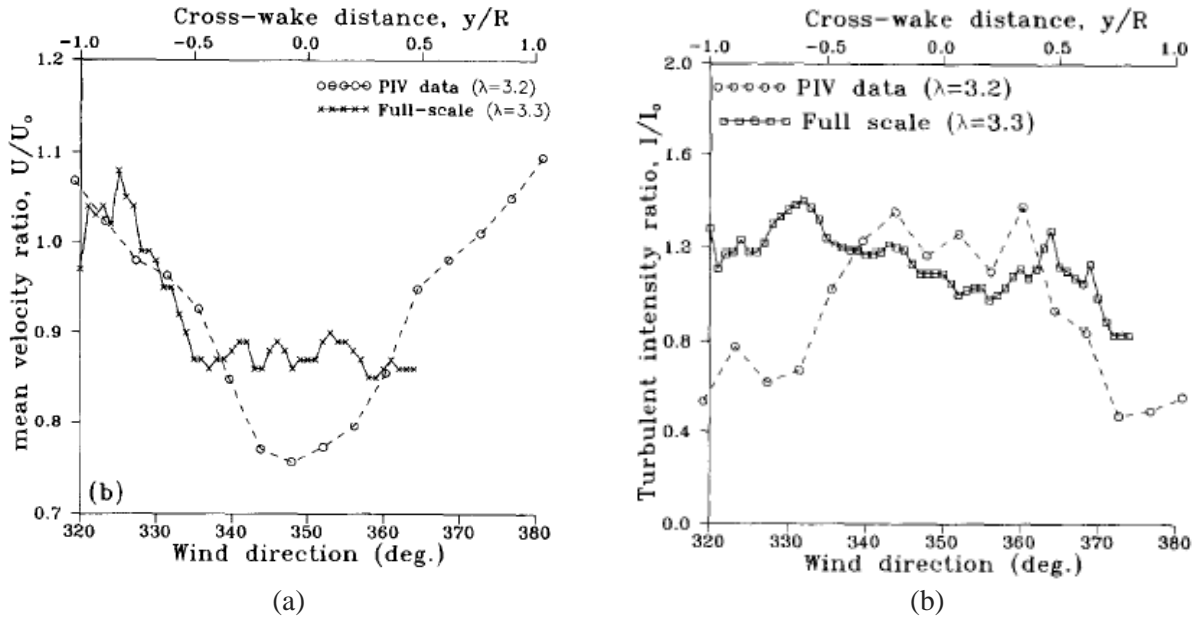


Figure 1-5: Radial profiles of a) normalized axial velocity b) normalized turbulence intensity obtained from PIV measurements performed on a scaled-down model and full scale measurements. The profiles are provided by Whale et al. (1996). Similarity in tip speed ratio was the criterion taken to account to choose the data corresponding to PIV and full scale measurements. The tip speed ratios are  $\lambda_{FS}=3.3$ ,  $\lambda_{PIV}=3.2$  corresponding to full scale and PIV measurements, respectively.

### 1.2.2 Wind Tunnel Measurements of Full –scale Turbine Rotors

To date only two experiments have been carried for large-scale turbine rotors in large wind tunnel set-ups. The NREL experiments, that were performed at the NASA-Ames wind tunnel (Schreck 2002), and the MEXICO experiments conducted at the DNW German-Dutch wind tunnels (Snel et. al. 2007).

The NREL measurements were performed on an actual two bladed rotor with the diameter of 10.1m. The model to tunnel area ratio was 1 to 10.8. The maximum rated power of the machine

was 19.8 kW with the design tip speed ratio of 8. The rotational speed of the rotor was set to 71.6 rpm and the local chord Reynolds number was  $Re_c=350,000$  at 0.75R of the blade. The measurements were mainly restricted to blade aerodynamic load and blade pressure distribution, with no emphasis on the wake measurements.

The MEXICO measurements were considered as a complementary experiment for the NREL in the sense that a three bladed rotor was used and wake measurements were targeted. The generic rotor had a diameter of 4.5 meter. The model to tunnel area ratio was 1 to 3.8 and therefore blockage effects were involved. The MEXICO project included measurements of blade load as well as the pressure distribution over the blade. In addition, near wake measurements were carried out using PIV technique in order to quantify the flow characteristics in the near-wake region. Throughout the velocity measurements, the rotational speed of the rotor was set to 424.5 rpm and the upstream wind speed varied between 10-30 m/sec. The design tip speed ratio was  $\lambda=6.67$  corresponding to  $U_{ref}=14.9$  m/sec. This leads to a local chord Reynolds number of  $Re_c=200,000$  at 0.6R of the blade. The axial profiles of axial and radial velocity components, immediately upstream and downstream the rotor, are presented in Figure 1-6 (a) and (b). The profiles are obtained at  $r=0.8R$  m for the case of zero azimuth angle of the blade and free stream wind speed of 14.9 m/sec. In each graph the profiles obtained from MEXICO experiment are compared with the results acquired from the numerical simulation performed by Schepers et al. (2012). It is obvious that the axial velocity drops at the rotor location due to the energy extracted by the turbine from the upstream wind. It can also be observed that radial velocity gains its highest values close to the rotor location and it decreases rapidly to the free stream level within a diameter downstream of the rotor (see Figure 1-6 (b)). Discrepancies between experiments and simulations are observed mostly in the downstream wake region.

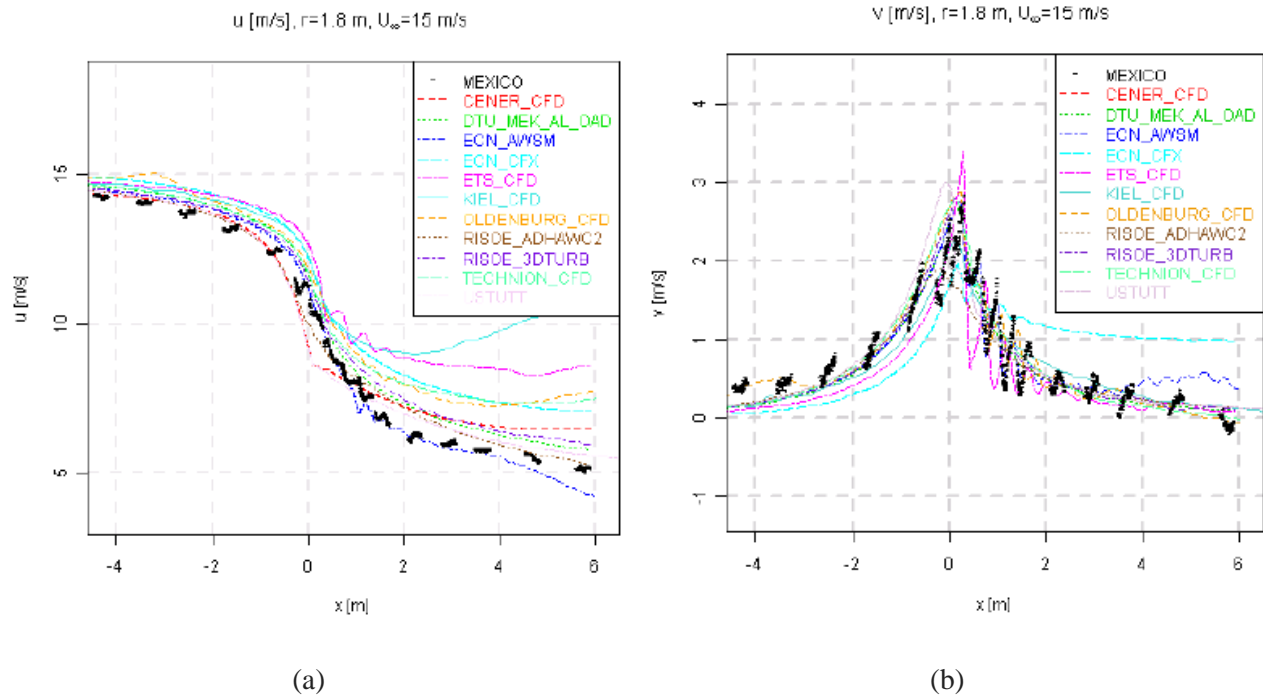


Figure 1-6: Axial profiles of a) axial velocity and b) radial velocity components obtained from MEXICO measurements. The results are compared with those obtained from numerical simulations (Schepers et al., 2012).

The results of the MEXICO project have been only partially analyzed and are mostly presented in the form of mean velocity profiles, with no emphasis on the turbulence characteristics (Schepers et al., 2012). Therefore, the need for a comprehensive investigation of rotational wakes of full scale models including investigation of the turbulent behavior of the flow in the near-wake region is evident.

### 1.3 Numerical and Aerodynamic Modeling Approaches

In addition to several experimental studies during the last two decades, various computational fluid dynamics methods and aerodynamic modeling were carried out to model the rotor and the wake in order to investigate the flow structure of the rotating wake in the near and far wake

regions, as well as the aerodynamic performance of the turbine (e.g. Sørensen and Kock 1995; Sørensen et al. 1998; Sørensen and Shen 2002; Gómez-Elvira et al. 2005; Troldborg et al. 2007; Ivanell et al. 2009, etc.). Sande et al. (2011) and Vermeer et al. (2003) presented a detailed overview of these studies.

In the following sub-section, two popular approaches in regard to the modeling of the turbine rotors are presented. In the next sub-section, the numerical approaches, which are mainly Computational Fluid Dynamics (CFD) methods used to simulate the rotating wake, are discussed.

### **1.3.1 Aerodynamic Modeling Approach**

The two popular approaches for aerodynamic modeling of wind turbine rotors, discussed herein, are the Blade Element Momentum (BEM) theory and the actuator disk/line model. The specifics of each modeling approach are presented as follows.

#### **1.3.1.1 Blade Element Momentum (BEM) Theory**

The Blade Element Momentum (BEM) theory approach has been the most popular modeling method used to determine the induction factors and aerodynamic forces of the turbine blades for several years, and is still being used routinely by industry (Hansen and Madsen, 2011). The advantage of the theory is the minimal computational time and resources as well as simplicity and ease of implementation (Hansen and Butterfield, 1993).

In the BEM theory, it is assumed that the blade can be analyzed as a number of independent stream tubes; hence, the span-wise flow is neglected. Moreover, there is no radial aerodynamic interaction between elements. The flow is assumed to be axisymmetric. Using the conservation of axial as well as angular momentum and blade airfoil section coordinate data, the induced

velocities and aerodynamic forces are computed based on an iterative solution for  $a$  (axial induction factor) and  $a'$  (angular induction factor). The induction factors are computed using following relations:

$$\phi = (2/3) \tan^{-1} \left( \frac{1}{\lambda_r} \right) \quad 1.2$$

$$\frac{a}{1-a} = \frac{\sigma'}{4F \sin^2(\phi)} (C_l \cos \phi + C_d \sin \phi) \quad 1.3$$

$$a' = -\frac{1}{2} + \frac{1}{2} \sqrt{1 + \frac{4}{\lambda_r^2} a(1-a)} \quad 1.4$$

where,  $\phi$  is the angle of attack of the relative wind speed,  $\lambda_r$  is the local tip speed ratio,  $F$  is the tip loss factor (will be discussed in chapter four, 4.2),  $C_l$  and  $C_d$  are the lift and drag coefficient, respectively. The iterative solution method to compute the induction factors and forces at each blade element using BEM equations is summarized in Figure 1-7.

Note that the results obtained from BEM method are highly dependent on the precision of the lift and drag coefficients (Ebert and Wood, 1997), since the solution is based on blade airfoil section coordinate data. Moreover, it should be taken into account that reasonable accuracy cannot be expected from the BEM method in all cases. These include yawed flow and unsteady aerodynamics situations where more detailed calculation of the velocity induced by wake and wake geometry is needed (Hansen and Butterfield, 1993).

Usually, a series of corrections, such as tip loss, stall delay and thrust coefficient, are added to the classical BEM solution in order to have more appropriate prediction for the modeling. The correction factors will be discussed more in detail in chapter 4 (see 4.2).

Refan and Hangan (2012) employed BEM approach to quantify the induction factors and consequently the power curve of the same wind turbine employed in the present work (see also



Refan (2009)). They have included three different correction factors into the classical BEM method. In chapter four (see 4.2), the accuracy of the BEM approach is quantitatively assessed throughout the comparison between the results acquired by the BEM approach and the present PIV results.

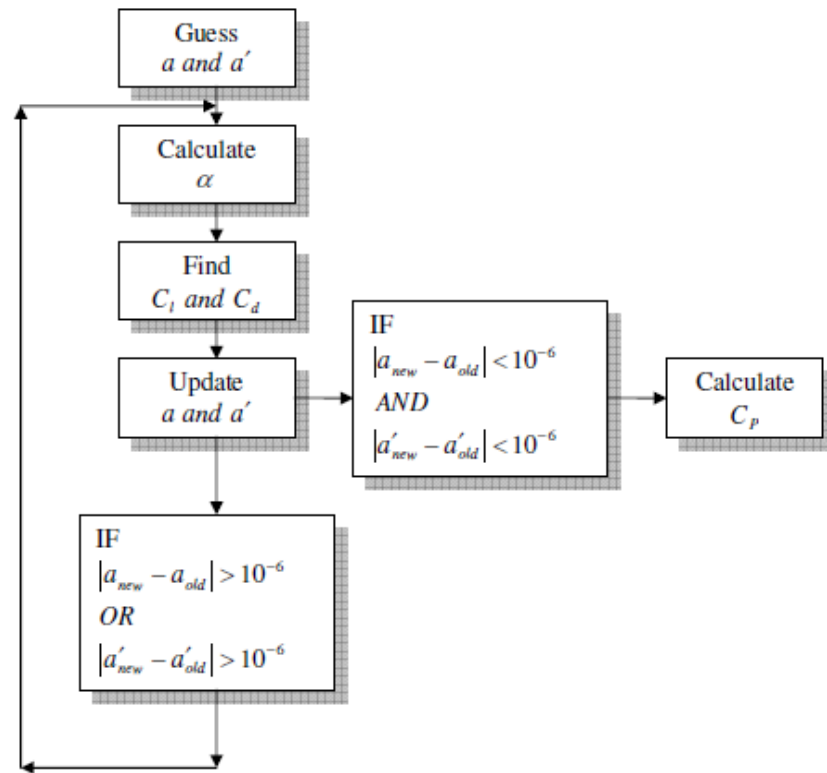


Figure 1-7: The diagram of the iterative process of the BEM approach (Refan, 2009).  $a$  and  $a'$  are axial and angular induction factors at a blade element, respectively.  $\alpha$  is the incident angle of attack at the corresponding blade element.  $C_l$  and  $C_d$  are the lift and drag coefficients obtained from the airfoil data at the corresponding blade element.  $C_p$  is the power coefficient of the rotor.

### 1.3.1.2 Actuator Disk/Line model

Considering the drawbacks of BEM method, a variety of more advanced aerodynamic analysis methods, including the actuator disk (AD) and line (AL) models, and the solution of the complete 3D unsteady Navier-Stokes equations have been developed (Sanderse, 2011; Vermeer

et al., 2003). In the actuator disk/line modeling approaches, instead of modeling the actual turbine, the rotor is simulated using volume forces. The difference between AD and AL models is that in the AD model, the volume forces are considered to be distributed evenly over the rotor disk, while in the AL model, the volume forces are distributed along the lines representing the actual blade positions (Sørensen and Shen, 2002).

Sørensen and Shen (2002) carried out a numerical simulation using AL model in order to study the three dimensional flow fields about a 500kW wind turbine equipped with three blades. In this simulation, the three dimensional Navier-Stokes solver was combined with the actuator line technique. The Navier-Stokes equations, formulated in vorticity-velocity variables, were discretized using finite difference approach. However, according to Shen et al. (2009), the disadvantage of the model is that the flow in a cross section of the blade was simplified, by replacing an airfoil by a point on the actuator line. Therefore, the model had the drawback of representing the flow past an airfoil, as two-dimensional modeling (see also Kasmi and Masson (2008)).

Figure 1-8 displays radial profiles of axial velocity at four different axial locations provided by (Sørensen and Shen, 2002). The tip speed ratio was  $\lambda=5.8$  throughout the simulation with the upstream wind speed of 10 m/sec. It can be inferred that the minimum axial velocity, corresponding to the maximum energy extraction from the wind, occurs at the mid section of the blade. In addition, it is clear that the wake expands as it moves axially. This behavior can be visualized by tracing the dots on the curves representing the tip vortices.

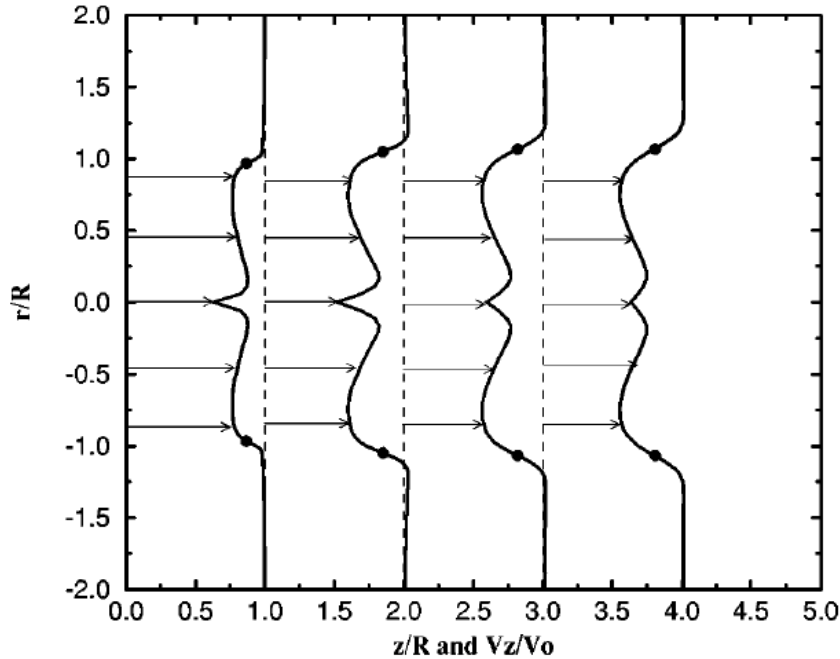


Figure 1-8: Radial profiles of axial velocity for  $\lambda=5.8$  and  $V_o=10$  m/sec. Dots represents the tip vortex (Sørensen and Shen, 2002).

### 1.3.2 Numerical Approach

Regarding modeling of the near or far wake, the major significance in CFD analysis of wind turbine wakes, compared to the abovementioned analytical and aerodynamic modeling approaches, is the simulation of turbulence. A large variety of turbulence models have been used; however, the two most prominent methodologies are Reynolds-Averaged Navier-Stokes (RANS) (e.g. Ammara et al. 2002; Alinot and Masson 2002; Gómez- Elvira et al. 2005; Kasmi and Masson, 2008) and Large Eddy Simulations (LES) (e.g. Jimenez et al. 2007, 2008; Wu and Porté-Agel, 2011; Calaf et al., 2010).

The standard  $k-\epsilon$  and  $k-\omega$  models usually result in too diffusive wakes, meaning the velocity deficit is too small and the turbulent intensity does not show the distinct peaks observed in the experiments (Sandarse et al., 2011). Several adaptations of these models are presently suggested

(Sanderson et al., 2011; Vermeer et al., 2003) to improve the modeling and therefore the availability of turbulent field experiments for benchmarking is critical. LES have the advantage of better handling of unsteady, anisotropic turbulent flows dominated by large-scale structures and turbulent mixing but they still need to be validated against experimental data to assess the modeling errors resulting from blade approximation and inflow conditions.

Troldborg et al. (2007) combined the large eddy simulation with an actuator line technique to simulate the wake of a wind turbine operating in a uniform flow. The rotor diameter of the turbine is 61.2m. The optimal tip speed ratio of the rotor is  $\lambda=7.07$ . The results are presented for different tip speed ratios at several axial locations downstream of the turbine. Samples of the instantaneous vorticity contours were shown in Figure 1-3 which depicted the development of the wake downstream of the turbine for different tip speed ratios (see also Figure 1-2 (d)). Note that the shortcomings associated to actuator line technique can be still applied to this simulation. Figure 1-9 shows the axial velocity profiles acquired from the numerical simulation conducted by Troldborg et al. (2007), at several axial locations downstream. Similar to the results provided by Sørensen and Shen (2002), it can be seen that the maximum power extraction from the wind is happening in the median to tip part of the blade section. However, the comparison of profiles reveals that the results have discrepancies in magnitude for  $z/R < 3$  where the results acquired by Troldborg et al. (2007) show larger velocity deficits. Also, the profiles do not match in the central part of the wake neither in trend nor in magnitude.

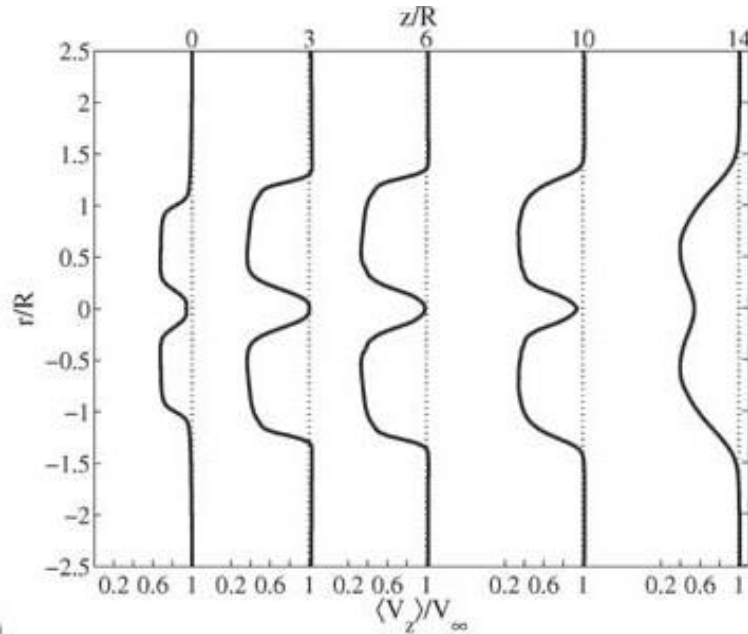


Figure 1-9: Radial profiles of normalized axial velocity for  $\lambda=7.07$  at different axial locations. The results are provided by Troldborg et al. (2007)

The results provided by NREL for the aerodynamic loading and pressure distribution over the blade, were used to validate the CFD results. One of the conclusions was that the methods in which the full N-S equations were solved are the best method to simulate the chordwise pressure distribution (Sørensen et al., 2002). Similarly Bechmann and Sørensen (2009) favorably compared their near wake simulations with the mean axial and radial components of velocity from the MEXICO experiment. There is now a need for turbulent field validation of these simulations through comparison with well conducted wind tunnel experiments.

## 1.4 Velocity Measurements using Particle Image Velocimetry (PIV)

Particle Image Velocimetry (PIV) is a non-intrusive technique facilitating velocity measurement of gas or liquid flow fields at many positions at one instance of time. One can conduct the velocity measurement with high spatial resolution using high resolution cameras as well as time resolved measurements using high speed systems. The PIV measurement is compatible with flow speeds ranging from very low speed flow ( $\mu\text{m/s}$ ) to supersonic flows. Moreover, the PIV method can provide both the instantaneous velocity vector fields and the statistics of the velocity field of a turbulent flow by taking a sufficiently large number of image pairs.

In most of the cases using PIV technique, a laser light sheet is generated by emitting a laser beam throughout a cylindrical lens. The thickness of the light sheet can be adjusted using a spherical lens. Afterwards, the flow is seeded by particles using an aerosol or particle generator, and these particles are illuminated by a laser light sheet. The camera is usually placed in front of the light sheet with its axis perpendicular to the light plane. A timing unit provides synchronization between the laser pulse emission and image capturing. One image pair is recorded when the flow is illuminated twice within a short time interval which depends on the mean velocity of the flow, the size of the imaging area, the size of the interrogation window and the correlation scheme (Adrian et al., 1991). The image couples are transferred to a computer to be processed by an image processing software. Velocity vector fields are acquired by cross-correlating the interrogation window in one image to the search region in the other image in two dimensions. Note that the proper distribution of tracer or seed particles within the measurement region is very crucial for reliable estimates of flow velocities using this technique. Figure 1-10 depicts the overview of a typical PIV system.

The accuracy of the PIV measurements can be influenced by a number of parameters such as the size of the seeding particles, seeding concentration, illumination source, recording device, synchronization between the illumination, acquisition and recording systems, and an appropriate choice of the different calculation parameters of the cross correlation analysis (Adrian et al., 1991).

Specifics of different components of the PIV system used in present study are presented in chapter four. Also, the uncertainties associated to the present PIV measurements will be analyzed in detail.

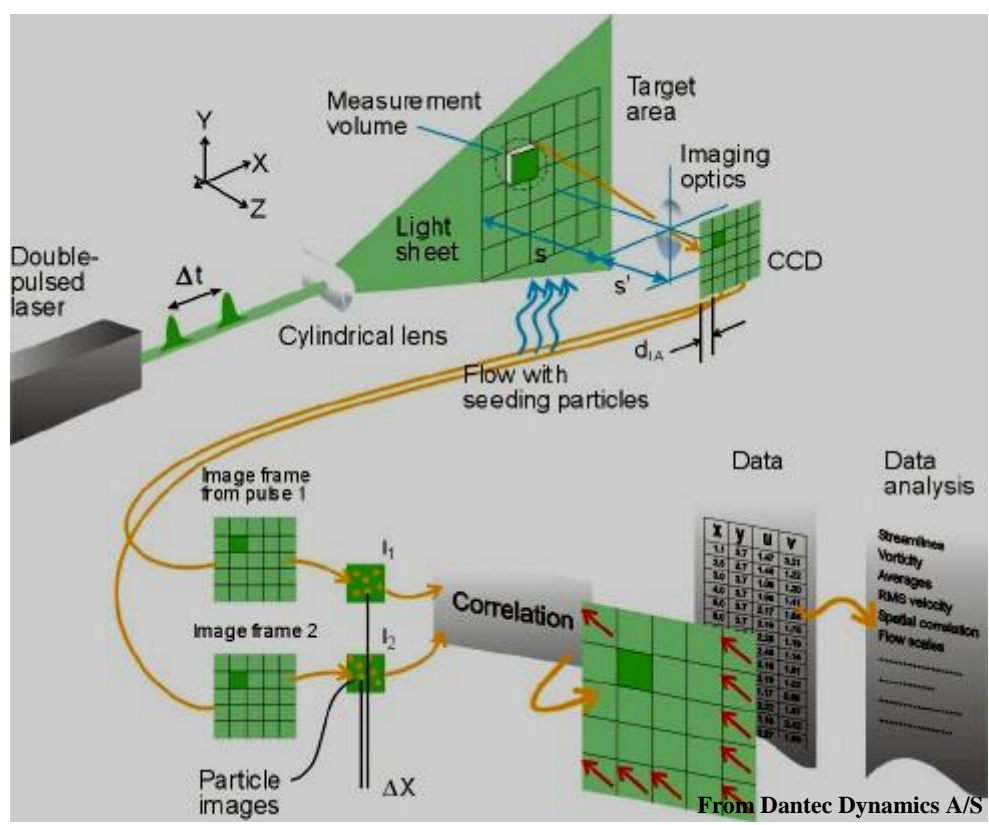


Figure 1-10: The overview of the PIV system configuration (From Dantec Dynamics A/S)

## 1.5 Scope

Experiments in controlled conditions and Computational Fluid Dynamics (CFD) are two principle tools in the study of the rotating wake behind HAWTs. CFD simulations have the advantage of providing data in the entire 3D volume; however, they still need to be validated against experimental data to assess the modeling errors resulting from blade approximation and inflow conditions. Therefore, the use of accurate wind tunnel data is indispensable.

Given the high uncertainties in full scale measurements and the scaling effects in small experimental set-ups, well conducted experiments in large wind tunnel facilities are critically important (Vermeer et al., 2003). To date only two such experiments have been conducted to measure the wake flow region. National Renewable Energy Laboratories (NREL) conducted experiments at the NASA-Ames wind tunnel (Schreck, 2002), and the MEXICO project experiments were conducted at the German-Dutch wind tunnel (Snel et al., 2007). The results of the NASA- Ames experiments refer mostly to measuring the aerodynamic loads and pressure distribution around the blades. The wake results of the MEXICO experiment have been only partially analyzed and are mostly presented in the form of mean velocity profiles with no insight yet in the turbulence characteristics (Schepers et al., 2012). Therefore, there is a stringent need for complementary and comprehensive large wind tunnel investigations of rotational wakes of wind turbines in terms of investigating the turbulent behavior of the flow in the near-wake region.

In the present research, PIV technique has been employed in a large wind tunnel set-up to measure the flow field behind a horizontal axis wind turbine in the near-wake region. The performance of the same wind turbine in terms of power curve and applicability of the BEM model have been previously studied by Refan and Hangan (2012). The phase-locked PIV



measurements are performed in several horizontal planes at two axial locations downstream of the turbine rotor.

Phase-locked PIV measurements, in large wind tunnels, are associated to several challenges including synchronization, seeding, and assembling the measurement area from smaller measurement windows. Therefore, there is a need to develop a robust method to obtain reliable measurements within the region of interest. Herein, it is aimed to investigate and determine PIV's capability to provide accurate velocity measurements within a rotating wake of a horizontal axis wind turbine and, to address the challenges associated with the implementation of the PIV technique in a large wind tunnel setup.

The second objective of the present research is to quantitatively study the flow structure within the near-wake region of a HAWT in terms of mean and turbulent components of the flow. The data acquired from phase-locked PIV measurements can provide unprecedented insight into the physics of the flow in a rotating wake, in particular the convection and dissipation of the tip vortex structure downstream. This can be used to advance the understanding of the flow structure of rotating wakes with implications to wake interference, wind farm optimization and numerical modeling validation.

In chapter two, the preliminary measurements of the wake of smaller wind turbines using PIV technique are presented. The chapter is concluded with the summary of findings used to improve the final measurements.

In chapter three, the experimental set-up of phase-locked PIV measurements is described. The test bed HAWT is introduced. The specifics of PIV system and the wind tunnel are presented in detail. Afterwards, the challenges and issues associated to phase-locked PIV measurements in

horizontal planes are discussed. The approaches adopted to resolve the corresponding issues are presented throughout the experimental procedure.

Chapter four encompasses three sections. In the first section, the results of phase-locked PIV measurements including mean and turbulent components of the flow are presented. Also, the physical phenomena associated to the flow structure within the near wake region are described. In the next section, the capability of the BEM theory approach is quantitatively investigated. The chapter ends with a quantitative assessment of the scaling effects.

Finally in chapter five, conclusions and recommendations as well as suggestions for future work are presented.

## 2 Preliminary velocity measurements using PIV technique

Preliminary velocity measurements are performed using Particle Image Velocimetry (PIV) technique in order to quantify the wake characteristics of three scaled horizontal axis wind turbines. The main objective of these preliminary measurements is to measure the flow field of the rotating wake and overcome the limitations of the conventional PIV measurement techniques in the case of velocity measurements within the wake of a wind turbine inside a large wind tunnel. The challenges can be summarized as follows:

- Covering a sufficiently large region behind the turbine within the wake to extract appropriate results.
- Introducing seeding particles properly into the flow field.

The results and the lessons learned from the experiments described in this chapter are used to design the final experiments described in Chapter 3 and 4 in which the wake characteristics are quantified in detail.

This chapter includes three sections. In the first section, the experiment set-up is described. In the next section, the experimental procedure is described. Finally, the results and analysis are presented.

### 2.1 Experimental Set-up

The experiments have been conducted at the low speed test section of the Wind Tunnel 2 in Boundary Layer Wind Tunnel Laboratory, at the University of Western Ontario. Figure 2-1 shows the schematic diagram of the experiment set-up. Velocity measurements are performed in

horizontal planes immediately behind the turbines. As shown in Figure 2-1, the seeding particles are introduced locally upstream the turbine rotor.

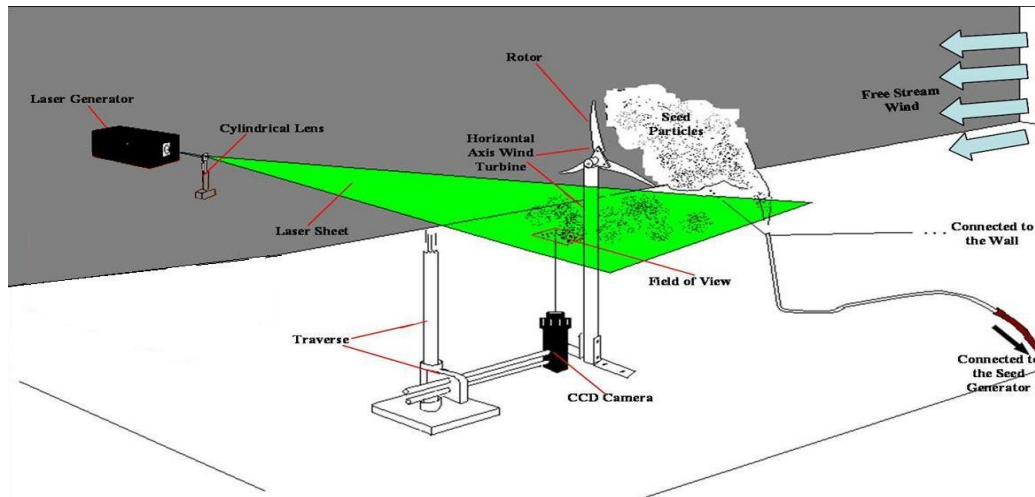


Figure 2-1: Schematic diagram of the experimental set-up

In the following sub-section, the specifications of the three model wind turbines are presented. The specifications of the other components of the experimental equipment, including the wind tunnel, PIV system, data acquisition system, etc., are presented in Chapter 3, since similar equipment were used in both sets of experiments.

### 2.1.1 The three scaled wind turbines

The velocity measurements were conducted for three different sets of turbine blades that correspond to the rotor diameters of 51.4 cm, 77 cm and 104 cm. Figure 2-2 shows the largest horizontal axis wind turbine. The blades, made of PVC, were connected to a wooden triangular hub at the center of the rotor. The average chord lengths of the blades for three different configurations are 5 cm, 4.2 cm and 2.83 cm corresponding to the large, medium and small rotors, respectively. The rotors were mounted on a metal post (shown in Figure 2-2). The height of the post was similar for the three rotors.



Figure 2-2: Configuration of the large size wind turbine

## 2.2 Experimental Procedure

The tests were carried out in the Boundary Layer Wind Tunnel Laboratory at the University of Western Ontario. The test section is 4m high, 5m wide and 52m in length. The wind speed corresponding to each turbine configuration was set in such a way to have similar Reynolds numbers (computed based on the chord length of the blade). Hence, the average wind speeds for the three configurations were 7.2, 4.9, and 4.1 m/s corresponding to the large, medium and small rotors, respectively. The tip speed ratio can be computed using  $\lambda = \frac{\Omega R}{U_{ref}}$ . The rotational speeds

for the three configurations were 340, 160, 215 rpm, respectively and consequently, the corresponding tip speed ratios were 1.27, 1.29 and 2.9, respectively. The PIV measurements were performed in horizontal planes, behind the rotor at a vertical position equivalent to the height of the post plus 44% the rotor radius where the post height is 101.2 cm. The vertical

positions for the three configurations were 114.0 cm, 118.4 cm and 124.1 cm above the ground level, respectively. Due to the limited size of the measurements window of the PIV equipment, a row of side-by-side windows was used to cover the entire measurement area with adequate resolution. The number of windows for the three configurations is 3, 4, and 5, respectively. A technique similar to the one used by Dobrev et al. (2008) was applied to patch the windows (the technique is described more in detail in Chapter 3). The length and width of the each window is 13 cm and 9.75 cm, respectively. A grid created on a wooden board was used as the calibration target for accurate determination of the location of the corresponding windows. Figure 2-3 (a) presents the configuration of the calibration board. The windows on the board were labeled by numbers: 1 to 5. The fifth window represents the region behind the hub. An overlap of 0.5 cm between each two windows was considered in order to patch the windows. Figure 2-3 (b) shows the schematic diagram of the calibration board within the experiment set-up with respect to the turbine rotor. Based on the mean free stream velocity inside the wind tunnel, the time interval between two laser pulses was determined. The wind speed was obtained from the Pitot-static tube located at the height of the rotor hub, 5 meter upstream the turbine to make sure it is out of the influence of the turbine. The time interval was determined based on an average pixel displacement which is  $\frac{1}{4}$  of the size of the interrogation window. In the present measurements, the size of the interrogation window is  $32 \times 32$  pixels resulting in an average pixel displacement of 8. During each experiment, the time interval was adjusted to obtain a pixel displacement of 8 in the region of interest by checking the velocity vectors for a few sample image pairs. The time interval was set 120  $\mu$ sec for large and medium wind turbines, and 80  $\mu$ sec for small turbine. 900 image pairs were captured at each window location at a capture rate of 15 image pairs per second.

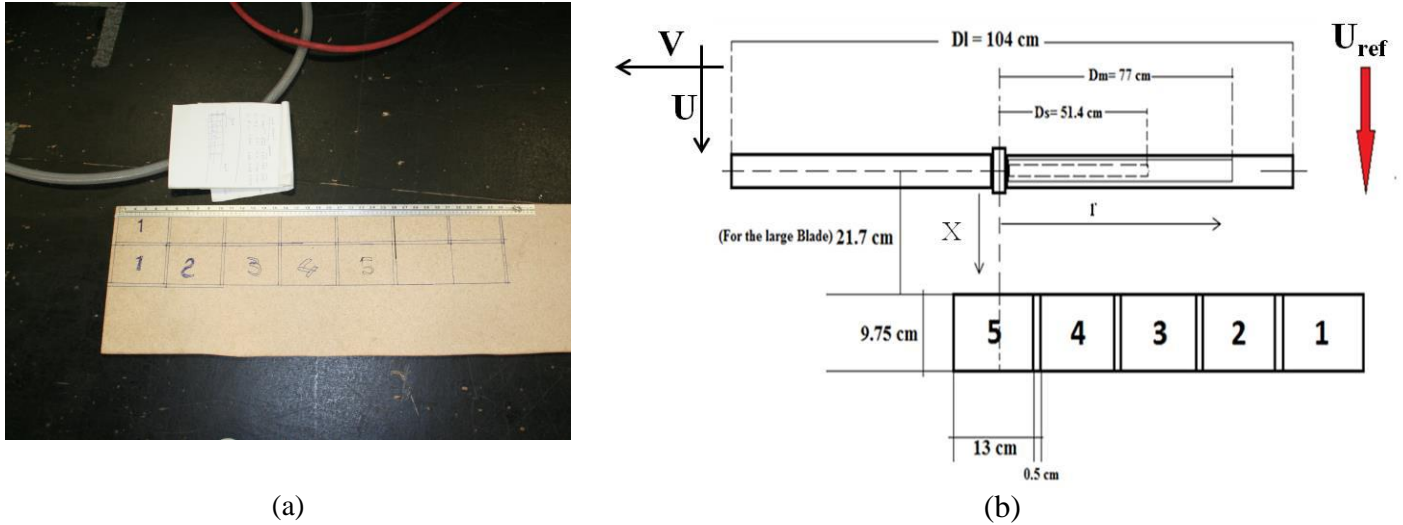


Figure 2-3: a) configuration of the calibration board, b) schematic diagram of the calibration board within the experimental set-up

### 2.2.1 Image processing

The method used to extract the velocity vectors in the multi frame single exposure PIV is the cross correlation (Raffel et al., 1998). The size of the interrogation region was set equal to  $32 \times 32$  pixels and the size of the search region is set equal to  $64 \times 64$  pixels. In order to increase the number of velocity vectors, a 50% window overlap was used. Therefore, 7326 velocity vectors were generated in each measurement window. The raw vector fields were produced using the commercial software Insight<sup>®</sup>. At the next step, corrections were applied to remove invalid vectors. Since the post-processing stage is identical to the final velocity measurement, the process is described in detail in chapter 3. In the following paragraph, the process of resolving the issues, specifically associated with this preliminary measurement, is presented.

In the present study, the particle distribution in images was non-uniform for two reasons:

1. The seeding particles were introduced into the flow locally upstream of the wind turbine (see Figure 2-1),

2. The rotation of the turbine blades broke down the jet of particles emitted from the particle generator into clouds of non-uniform seeding. Therefore, in all images, there were regions with very poor seeding, which needed to be identified and consequently eliminated before the images were processed to generate vectors. This procedure was challenging, since the location and extent of these regions changes in each snapshot.

In an image obtained from PIV measurement, there are regions in which particle density and illumination is adequate, and therefore the grey-scale value is relatively high. On the other hand, due to the illumination of fewer particles in the regions with low or negligible particle density, the gray-scale values in these regions are low. Using this feature of the images, a scheme developed by Siddiqui et al. (2008) was employed to detect the regions with low seeding density automatically and exclude them in further analysis. In the first step of this procedure, by adjusting the upper and lower gray-scale limits, the gray-scale values of the image were re-scaled and therefore, the signal-to-noise ratio of the image was enhanced. The analysis of the gray-scale distribution, in a subset of images from the given dataset, was used to set the limits. Note that for the given dataset, the upper and lower limits kept constant. In the next step, a binary image was created from the corresponding gray-scale image by applying a threshold. The gray-scale values higher than or equal to the threshold were assigned a value of 1 (the white regions in Figure 2-4 (b)), representing the regions with adequate particle density. The pixels/search windows with gray-scale values lower than the threshold, were assigned a value of 0 (the black regions in Figure 2-4 (b)), indicating the regions with insufficient seed particle density. The gray-scale values in the regions with very low seed density were analyzed in order to set a threshold. This threshold was kept constant for the entire dataset of a given experimental run. To remove the noise, a set of morphological operations were performed in two sequences. In the first

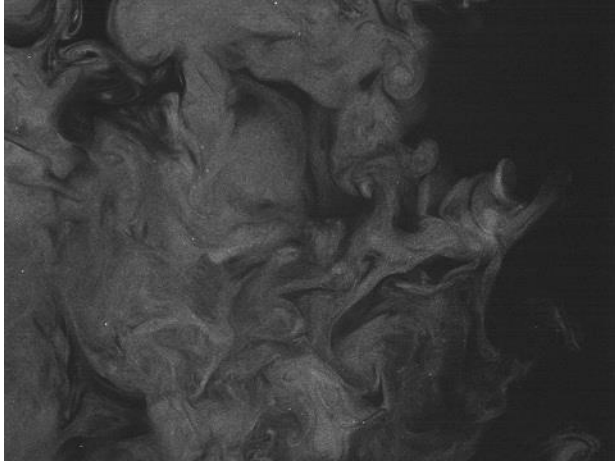


sequence, using a square mask of  $10 \times 10$  pixels, a dilation operation followed by an operation which closes the “holes” within the object was performed. This procedure was followed by an erosion operation. In the second sequence, erosion, dilation and closing holes operations were applied by using a square mask of  $20 \times 20$  pixels. Figure 2-4 (a) and (b) display a binary image and the corresponding original image. It can be clearly seen that the regions with low particle density are correctly detected.

In the next step, the spurious vectors, associated with the regions with insufficient particle density in the raw velocity fields, were eliminated using the binary images as a mask. That is, in a given raw velocity field, all velocity vectors within the black regions of the corresponding binary image were assigned as NaN, as a convenient way to mark the variables for further consideration. It should be mentioned that the regions with sufficient particle density (white regions) also have occasional spurious or invalid vectors. Using a scheme developed by Siddiqui et al. (2001), the spurious vectors in these regions were identified and then corrected by applying a local median test as well as a global filtration. Spurious vectors, located in the neighborhood of a low particle density region, were corrected by considering only the neighboring vectors in the region with adequate particle density in the median test. It has been observed that the spurious vectors within the regions with adequate particle density are less than 5% of the velocity vectors. Figure 2-4 (c) and (d) shows the raw instantaneous velocity vector field and the corrected one, corresponding to the image shown in Figure 2-4 (a).

In the final step, the velocity calibration was performed using a MATLAB program to convert the particle displacements to velocity (m/sec). Initially, the calibration ratio corresponding to each tile of the calibration board (i.e. the image scale in mm/Pixel), was determined using the calibration images. Thereafter, the calibration ratio and the time interval between the two consecutive images in a pair

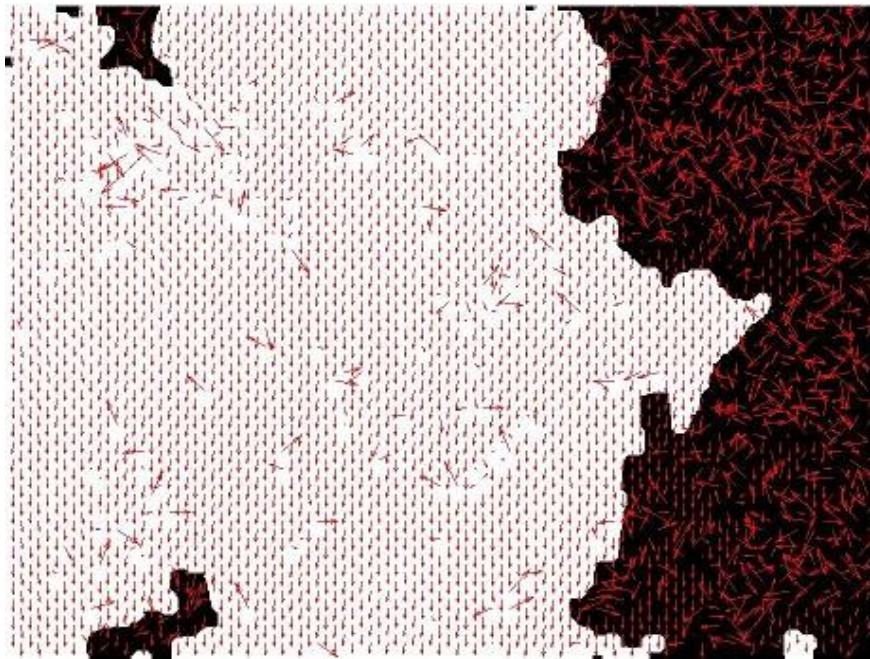
were input into the program to convert the particle displacement fields (in pixel per interval), obtained from the image processing stage, to velocity fields (in m/sec).



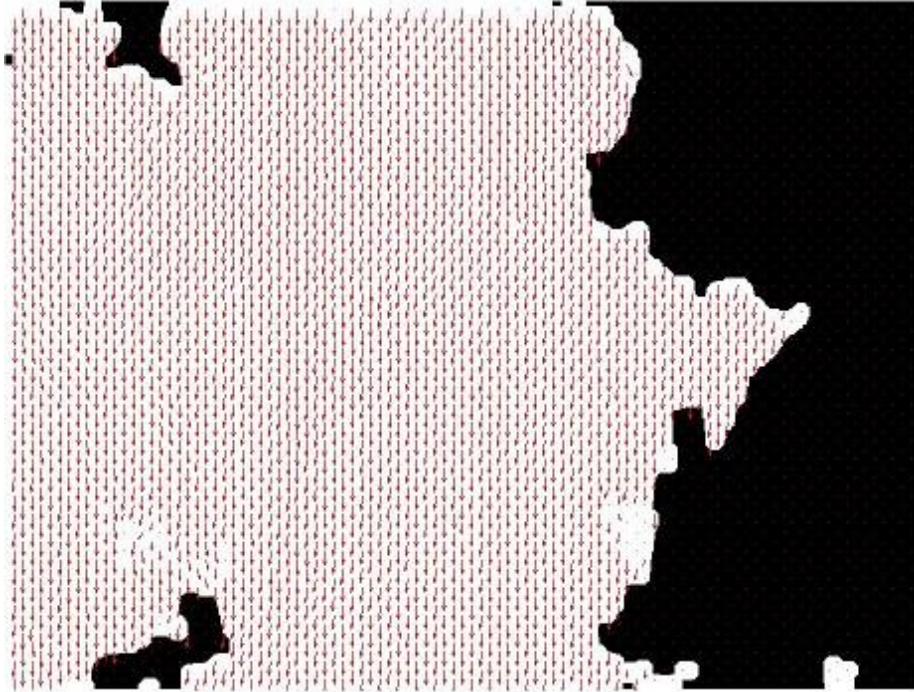
(a)



(b)



(c)



(d)

Figure 2-4: A sample of a) PIV image b) corresponding binary image c) raw instantaneous velocity field superimposed to the binary image d) corrected velocity field superimposed to the binary image.

## 2.3 Results and Discussion

In the next subsection, following characteristics are presented.

- Distribution of mean axial velocity deficit
- Distribution of mean radial component of velocity
- Radial profiles of mean axial velocity deficit and radial velocity

The mean flow components were obtained at each grid point by averaging the data obtained from the instantaneous velocity fields. Note that the measurements were not phase-locked.

It should be also mentioned that depending on the number of the images (out of 900) in which there have been valid vectors for a given location, the mean values at each location is based on a

different number of data points (snapshots). Therefore, one can argue that the validity of the mean value for different points across the flow field is not uniform. This can be considered as a significant point of concern about this methodology, which reduces the reliability of the statistics. In order to avoid this issue, in the final measurements (see Chapter 3), it is guaranteed that the seeding particles are distributed uniformly within the measurement area.

As we will discuss in the following paragraphs, due to the differences in the scale and configuration of the scaled wind turbines, as well as the uncertainties caused by non-uniform seeding, the results of these experiments do not provide a full/complete representation of the characteristics of the wake of a large scale wind turbine. Therefore, we limit the scope of this section to the results from the experiments involving the largest scaled wind turbine, as a representative case.

### **2.3.1 Axial Velocity**

Figure 2-5 shows the contour plots of time-averaged non-dimensional axial velocity deficit,  $-(1-U/U_{\text{ref}})$ , where  $U$  is the time-averaged velocity. The area behind the rotor is covered by a row of five windows, as shown in Figure 2-3 (b).  $r/R$  represents the non-dimensional radial position where  $r$  is the radial position measured from the center of the rotor and  $R$  is the radius of the turbine rotor.  $X/R$  represents the normalized axial position where  $X$  is the axial distance from the rotor plane. The windows are presented un-patched in order to see how consistent the results are from one window to the other one.

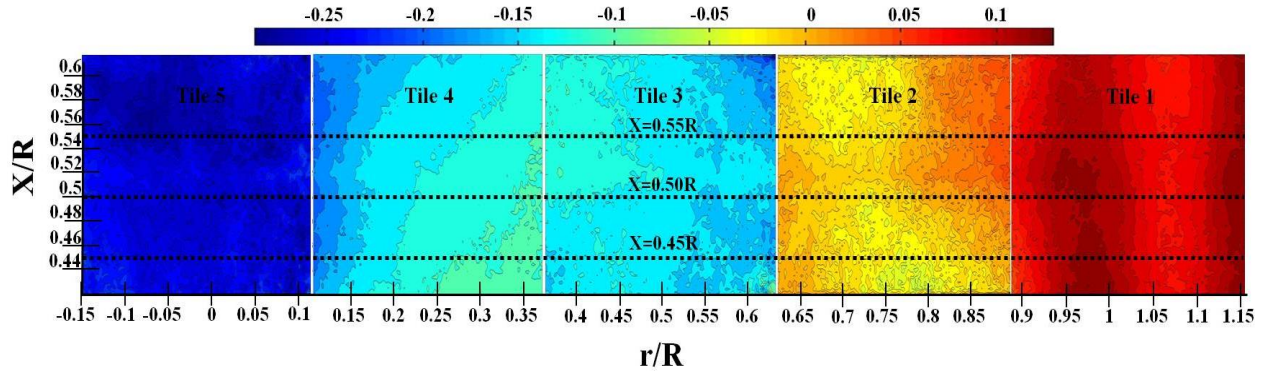


Figure 2-5: Contour plots of normalized axial velocity deficit, for the 5 windows covering the area behind the rotor of the large size wind turbine. The windows are not patched.

As shown in Figure 2-5, there exists flow retardation where the axial flow is less than the free stream wind speed in the region close to the center of the rotor. This behavior is in contrast with the results provided by previous investigations ((Magnusson, 1999; Sørensen and Shen, 2002; Watters and Masson, 2007) where the maximum flow retardation occurs at the median to tip part of the blade section. Farther from the center, the axial velocity increases, and close to the tip of the blade,  $r/R \sim 0.8$ , the flow accelerates. It can also be seen that the full recovery of the axial velocity occurs at  $r/R < 1$  indicating that the wake does not expand. This is also in contrast with the behavior observed by previous investigations (Vermeer et al., 2003; Sørensen and Shen, 2002).

As shown in Figure 2-5, it can be seen that the changes between all windows are approximately consistent. However, there is an inconsistency between tile 3 and the two neighboring tiles. In order to assess this behavior, the profiles of axial velocity deficit as a function of radius for three different axial locations ( $X/R = 0.45, 0.50, 0.55$ ) are plotted (see Figure 2-6). A technique similar to the one used by Dobrev et al. (2008) and Xiao et al. (2011) was applied to patch the windows. For this purpose, the mean velocity at each point within the overlap region between two adjacent

tiles was set equal to the average of the velocity values at that point within the two neighboring tiles. It can be inferred that overall, the axial velocity is increasing from the center of the rotor toward the tip at all three different axial positions. However, the presence of two large discontinuities (at  $r/R \sim 0.6$  and  $\sim 0.9$ ), corresponding to the third and second tiles, in all three curves is obvious. This can be attributed to the low number of good vectors remaining from the procedure of generation of binary images and exclusion of bad vectors at the edges of the tiles.

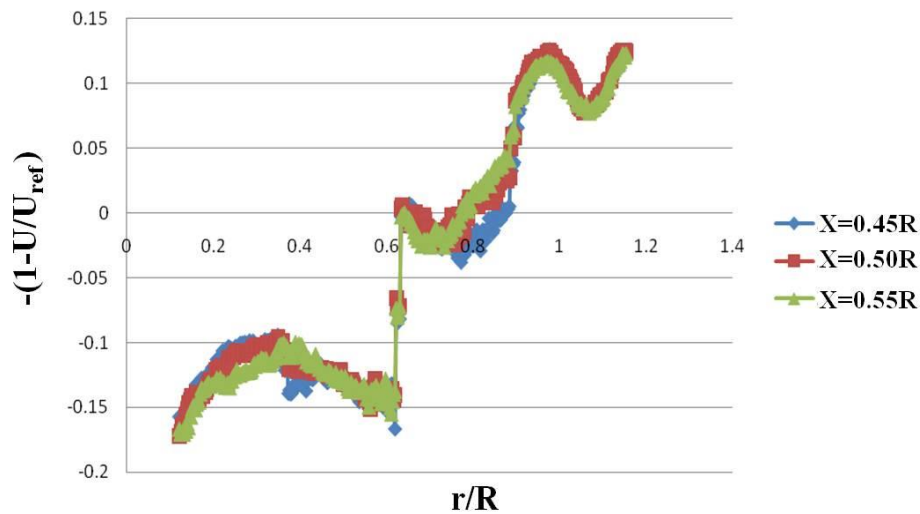


Figure 2-6: Profiles of axial velocity deficit at three different axial positions.

### 2.3.2 Radial Velocity

Figure 2-7 presents contour plots of non-dimensional radial component of velocity,  $V/U_{ref}$ , where  $V$  is the time-averaged crosswind component of velocity. Close to the center of the turbine rotor, the velocity is negative and the air flows toward the rotor axis. The velocity magnitude reaches to zero at  $r/R \sim 0.36$ . After this point, the crosswind component increases and gets the highest value at  $r/R \sim 0.7$ . This outward flow direction, close to the blade tip, explains that the wake has a tendency to expand. However, one can expect that the radial velocity should be positive very close to the tip,  $r/R \sim 1$ , in order to justify the expansion of the wake. In the present case, the

radial velocity tends towards zero at  $r/R \sim 0.8$  and becomes very small at  $r/R \sim 1$ . This behavior, similar to the one observed for the axial velocity, indicates that in contrast with previous investigations (Vermeer et al., 2003; Sørensen and Shen, 2002), the wake of the rotor does not expand.

Similar to the contour plots corresponding to axial velocity deficit, the largest discontinuity from one tile to another, appears at the boundaries of the third tile. This can be explained by the fact that the number of good vectors remaining from the procedure of generation of binary images and exclusion of bad vectors is very low at the edges of the tile. This can be attributed to the poor seeding distribution in the corresponding window during the measurements. Therefore, the average velocity, at the regions where tile 3 is patched to the neighboring tiles, is not consistent with tile 4 and tile 2. Besides improving the particle distribution, another solution for this issue can be to increase the overlap between two windows.

Figure 2-8 displays the profiles of radial component of velocity as a function of radius at three different axial locations ( $X/R = 0.45, 0.50, 0.55$ ). The graph confirms previous conclusions inferred from the profiles of axial velocity as well as the contour plots of both axial and crosswind component of velocity. It can be observed that close to the tip region, at  $r/R \sim 0.7$ , the radial velocity is positive indicating an outward flow. The velocity reaches zero at  $r/R \sim 0.8$  and become very small at  $r/R \sim 1$ . Overall, this behavior does not indicate the expansion of the wake. Moreover, the presence of a large discontinuity (at  $r/R \sim 0.6$ ), corresponding to the third and second tiles, in all three curves is obvious.

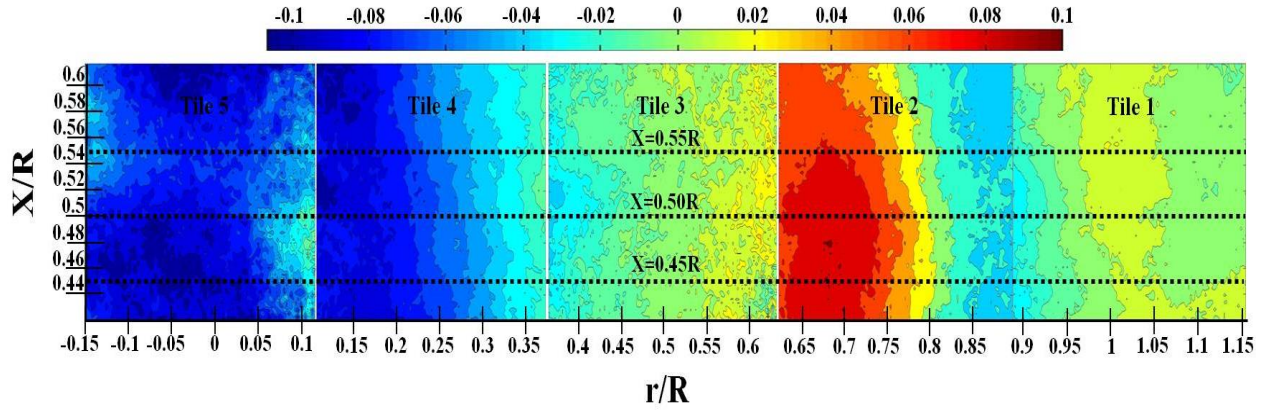


Figure 2-7: Contour plots of normalized radial velocity, for the 5 windows covering the area behind the rotor of large size wind turbine. The windows are not patched.

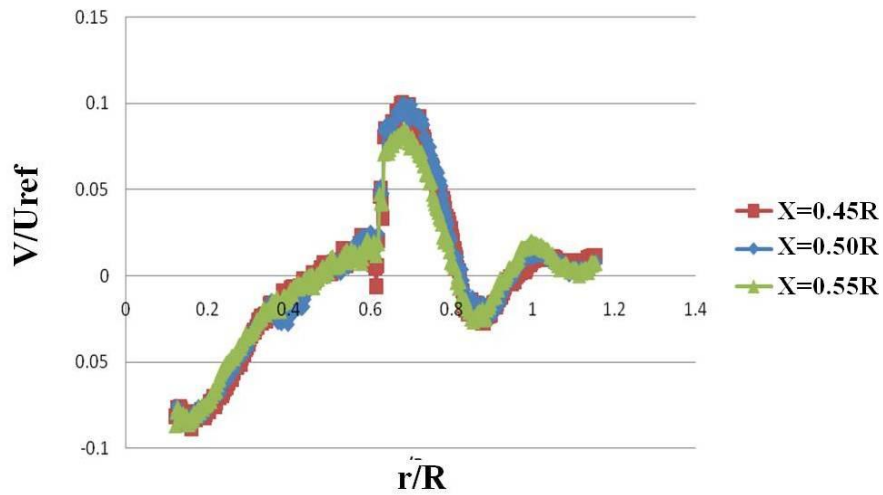


Figure 2-8: Profiles of radial velocity as a function of radius at three different axial positions.



## 2.4 Concluding Remarks

The procedures and results presented in this chapter were used as a basis to experiment and understand the challenges associated with PIV measurements in the near wake of a wind turbine, in a large wind tunnel set-up. These findings can be summarized as follows:

- The particle distribution was non-uniform within the images since a jet of seeding particles were introduced into the flow locally and consequently broke down into clouds of non-uniform seeding. The regions with poor seeding were identified and consequently eliminated using binary images. The procedure of generation of binary images and exclusion of bad vectors results in low number of good vectors at the edges of the tiles, appearing as inconsistencies in velocity profiles and contour plots. In addition, depending on the number images in which there have been valid vectors for a given location, the mean values at each location is based on a different number of data point. Therefore, the validity of the mean value for different points across the flow field is not uniform. It can be concluded that to resolve the issues associated with seeding, the particles need be introduced in a more consistent manner to guarantee the uniform particle distribution within the measurement area.
- The overlap region between two neighboring tiles was set to be five percent of the radial length of each tile. According to the results, velocity profiles and contour plots, the overlap between the tiles should be increased in order to obtain proper consistency between two neighboring windows.
- Preliminary velocity measurements were performed at fixed horizontal locations. Since the measurements were not phase-locked, the results only provide a time averaged flow field within the corresponding fields of view. This is confirmed by the velocity contour

plots where no dominant flow structures, in particular tip and root vortex structures, were appeared in the velocity fields. However, the flow structure within the near wake region is highly influenced by the tip and root vortex structure and therefore it is expected to be highly phase dependent. In order to re-construct the phase-averaged three dimensional flow field from the planes at fixed axial locations, phase-locked measurements should be performed.

These findings were employed as a basis for another velocity measurements within the near-wake region of a HAWT in a large wind tunnel set-up, described in Chapter 3.

### **3 Velocity Measurements using PIV Technique- Experimental**

#### **Procedure**

In this chapter, the experimental procedure, conducted to quantify the velocity field within the near-wake region of a small horizontal axis wind turbine (HAWT), is presented. Particle Image Velocimetry (PIV) is the technique employed for velocity measurements. Herein, the objective is to assess the application of the PIV technique in flow investigation in a large wind tunnel set-up. There are significant challenges regarding the phase-locked PIV measurements in a large wind tunnel set-up, in particular in the case of velocity measurements within the rotating wake of a wind turbine. The challenges include the seeding process, the process of calibration, the method to cover a large measurement area downstream of the turbine, the synchronization between image capturing system and laser light generator and the rotation of the turbine, to phase-lock the flow with the measurements, and the patching process. Throughout the following sections, the above-mentioned issues and challenges associated with the PIV measurements are discussed. Moreover, the approaches adopted to resolve the issues are presented.

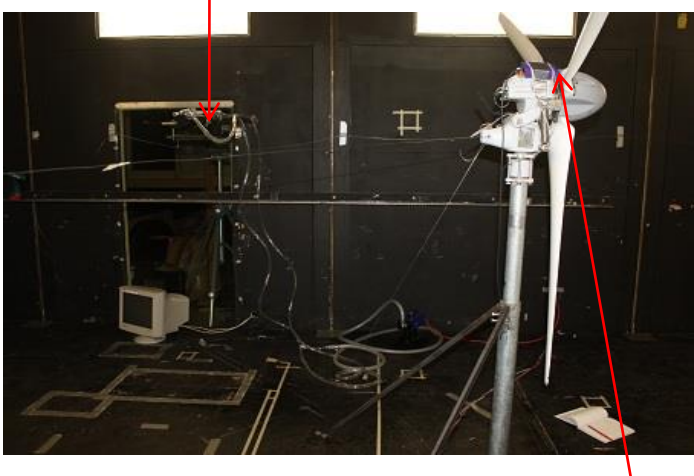
The chapter includes two sections. In the first section the experimental equipment and test setup are described. In the second section, the experimental procedure is illustrated.

#### **3.1 Experimental Set-up**

PIV measurements were performed in horizontal planes downstream a small horizontal axis wind turbine. The results are used to determine radial and axial velocity vectors. The set-up is mounted at the low speed test section of Wind tunnel 2, at the Boundary Layer Wind Tunnel Laboratory, at Western University. Figure 3-1 shows the schematic diagram of the experiment

set-up. All components of the PIV system, except the camera and particle generators, were set up outside of the wind tunnel to avoid any flow disturbances. Therefore, the laser sheet was emitted through a glass window (see Figure 3-1(a) and (b)). A small Emitter/Detector (E/D) device, as shown in Figure 3-1 (a), was mounted on the top of the turbine nacelle, used to phase-lock the measurements (see 3.1.13 for more details).

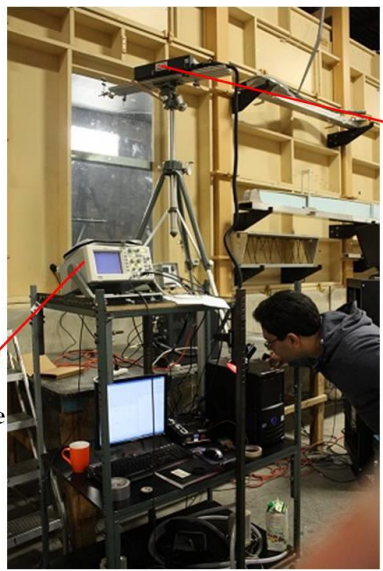
**Laser Generator**



**E/D Device**

(a)

**Digital  
Oscilloscope**



**Laser  
Generator**

(b)



(c)

Figure 3-1: Experimental Set-up

### 3.1.1 Experimental Equipment

The specifications of each component of the experimental set-up are provided in the following sub-sections.

#### 3.1.1.1 Small Horizontal Axis Wind Turbine

The wind turbine used in this study is an upwind, three bladed small horizontal axis wind turbine with the rotor diameter of 2.2 meter. Figure 3-2 displays the turbine rotor in the test section. According to manufacturer's report, the turbine has a rated power output of 900 W at 12.9 m/sec and a peak power output of 1200 W at 17 m/sec. The wind turbine has an eight-pole synchronous generator with 900 rpm synchronous speed in a 60 Hz electrical network. Also, the wind turbine has a control panel which includes all necessary power management, conversion, and diversion load safety circuits.



Figure 3-2: Configuration of the upwind three bladed small HAWT rotor in the test set-up

Each blade of the turbine is 0.91 m in length. The root and tip chords are 12.7 cm and 5.4 cm in length, respectively. The specifications of the blade, including the distribution of the chord and the twist angle in the spanwise direction, airfoil geometry at different blade sections and the blade geometry, are presented in Figure 3-3. While the tip region of the blade ( $0.58 \leq r \leq 1.1$ ) is designed using a thin airfoil in order to achieve high lift to drag ratio, the root region ( $0.12 \leq r \leq 0.57$ ) is designed using a thick airfoil due to structural strength considerations.

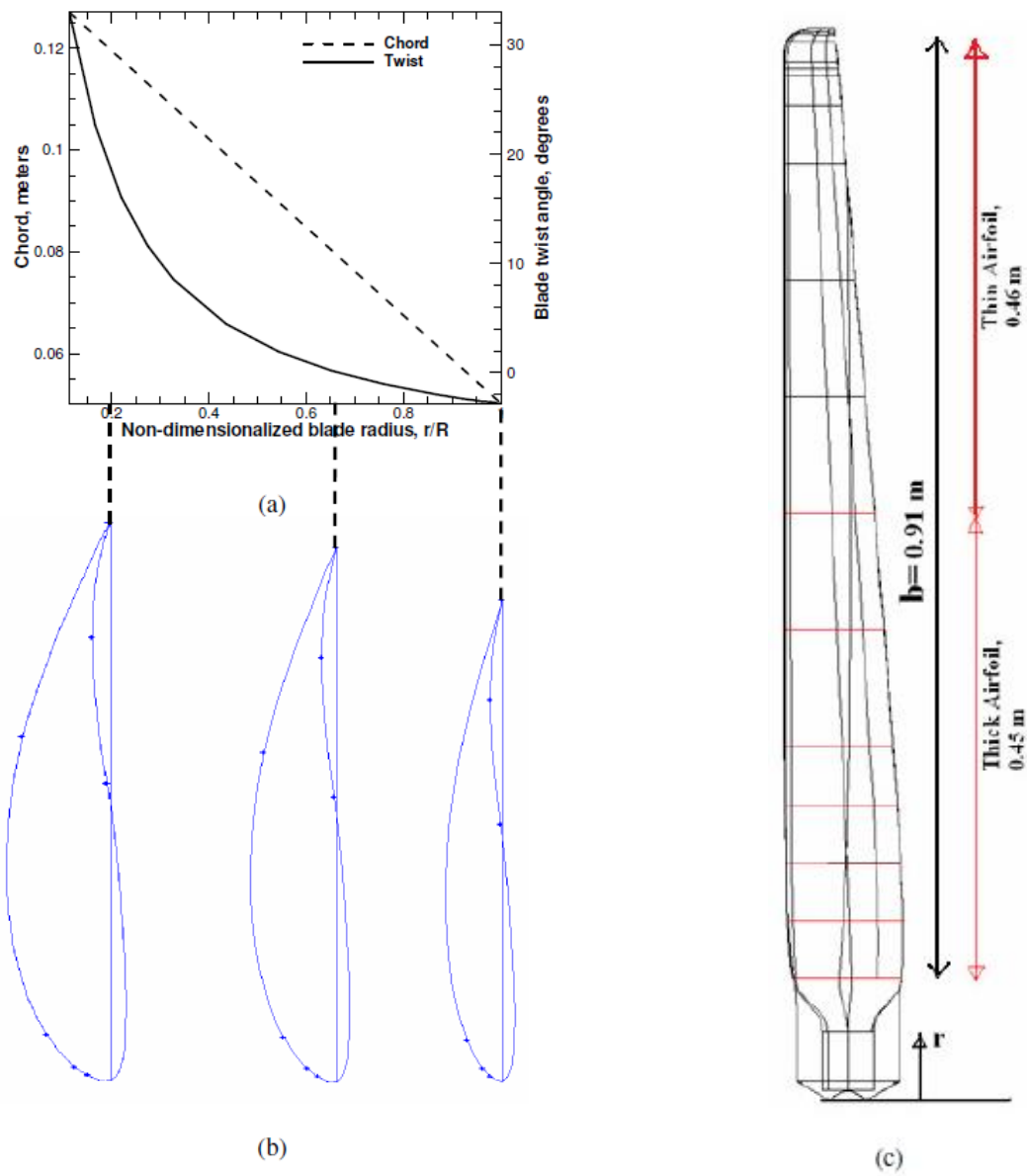


Figure 3-3: a) Distribution of chord and twist angle in the span-wise direction, b) Airfoil geometry, c) Blade geometry (from Refan, 2009).

Figure 3-4 shows the power coefficient of the HAWT rotor versus tip speed ratio obtained from the theoretical and experimental results provided by Refan and Hangan (2012). It can be observed that the optimal tip speed ratio corresponding to the maximum power coefficient is

about 5, as predicted by the BEM theory (Refan and Hangan, 2012). The experimental results correspond to the off-design operational condition ( $\lambda > 5$ ) of the turbine.

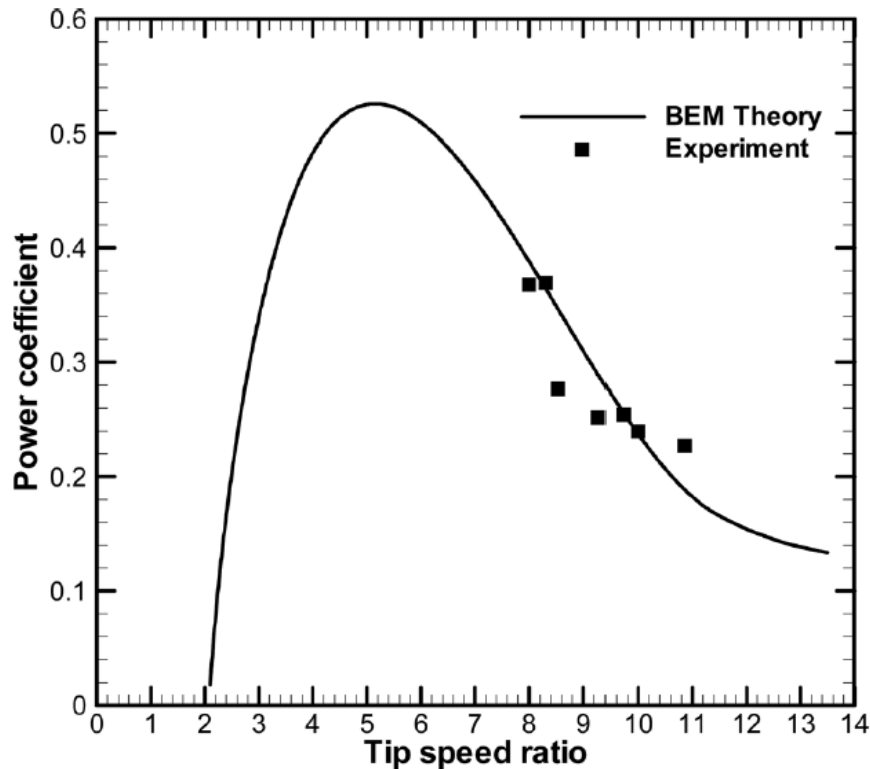


Figure 3-4: Power coefficient versus tip speed ratio obtained from experimental and theoretical results provided by Refan and Hangan (2012)

More information regarding the blade specifications, measurement of aerodynamic forces, measurement of power output and prediction of the power output using the BEM theory can be found in the work of Refan (2009).

### 3.1.1.2 Wind Tunnel

Velocity measurements are performed in the Boundary Layer Wind Tunnel 2 (BLWT 2) at the Western University. Wind Tunnel 2 is a closed-loop tunnel with two test sections, a low speed and a high speed one. Figure 3-5 shows the schematic diagram of BLWT 2. The experiments are



performed in the low speed test section of the wind tunnel. The test section is 4m high, 5m wide and 52m in length. A maximum wind speed of 36km/h (10m/s) can be produced in this section. The average wind speed through the measurements is set to be 4.12 m/sec. The turbine rotor was installed 11 meter downstream of the test section. The distance between the turbine post and lateral walls are 2.5 meter. Vertical profiles of axial velocity and turbulence intensity in the tunnel at the location of the turbine are shown in Figure 3-6. The profiles were obtained using a Cobra probe in the tunnel without the turbine. As shown in Figure 3-6, the boundary layer thickness at the location of the wind turbine is about 1 meter. The freestream turbulence intensity is approximately 2% at the height of the rotor hub.

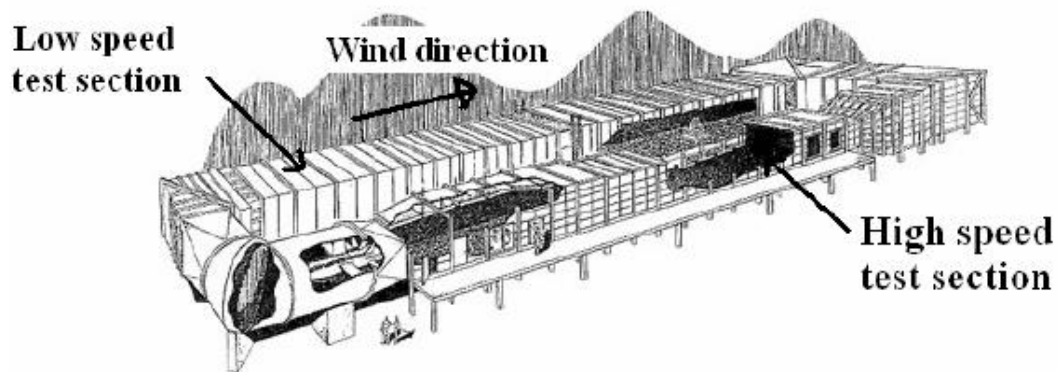


Figure 3-5: schematic diagram of BLWT 2 at the Boundary Layer Wind Tunnel

Laboratory, Western University

The rotor performance can be influenced by the possibility of free expansion of the wake, since the rotor inflow and the wake structure are mutually dependent. In other words, disturbed expansion of the wake can affect the performance of the rotor. Therefore, in wind tunnel measurements, especially in case of a wind tunnel with a closed test section, the blockage ratio should be kept at a minimum to reduce this effect. The blockage ratio is defined as the ratio of the model's frontal area to the local area of the tunnel test section. In the case of the wind

turbine, the blockage ratio is defined as the ratio between the rotor disk area and the cross section area of the tunnel test section. According to Vermeer et al. (2003), the blockage ratio in different wind tunnel measurements varies between 1 to 125 to 1 to 1 in previous studies, where for the latter, it is clear that undisturbed expansion of the wake is not possible. In the present study, the blockage ratio in the low speed test section of the wind tunnel is 1 to 5.3. It should be noted this value is based on a conservative calculation because the solidity of the rotor, (i.e. the ratio of the area of the blades to the swept area) is relatively small ( $\sigma' = 0.039$ ) (Refan and Hangan, 2012).

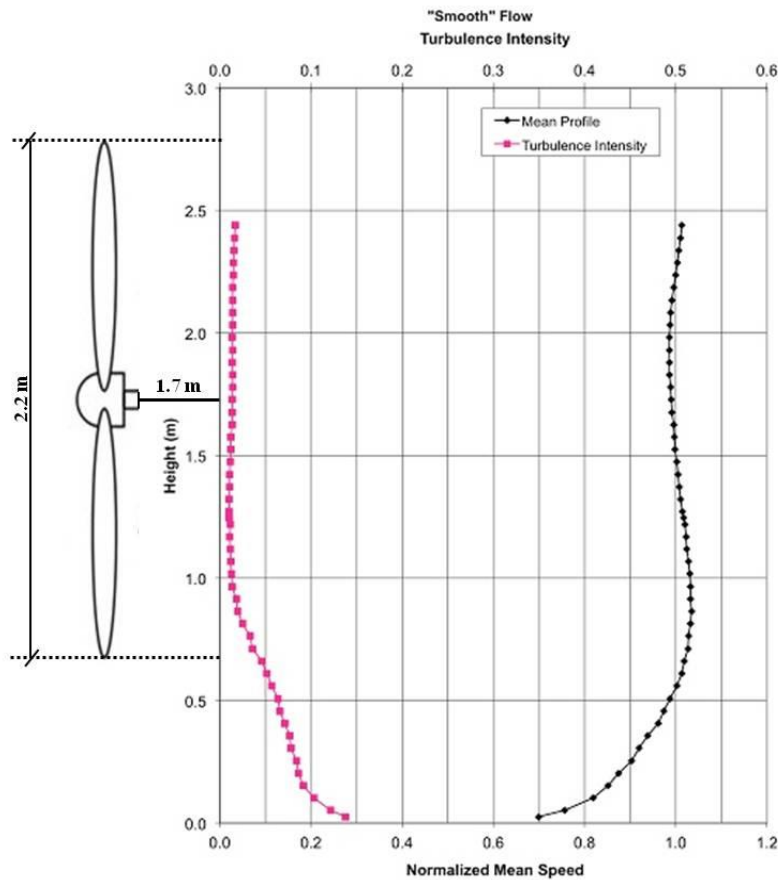


Figure 3-6: Vertical Profiles of normalized mean speed and turbulence intensity in the tunnel. Mean speed is normalized by a reference wind speed of 7.8 m/sec. Turbulence intensity at each height is normalized by the corresponding mean speed.

### 3.1.1.3 Emitter/Detector Device

A small Emitter/Detector (E/D) circuit is manufactured and used for generating the triggering signal for the phase-locked PIV measurements. Figure 3-7 displays the configuration of the E/D device. The circuit output is a pulse signal with 5 Volt amplitude. The circuit is installed in a small box in order to be mounted on top of the turbine nacelle immediately behind the rotor. A small red LED emits the light. The detector is installed next to the emitter (See Figure 3-7). The light emitted by the LED is reflected by a small mirror, mounted at the back of on one of the blades. Once the light is detected by the detector, the circuit generates an output signal. This signal is used for two purposes. First it is used as a trigger signal for the PIV system for phase-locked measurements (Details can be found in 3.2.2). Secondly, the output signal is utilized to compute the rotational speed of the rotor using digital oscilloscope. Since the mirror reflecting the light is attached to the blade, the frequency of the output signal is identical to the rotational frequency of the rotor.

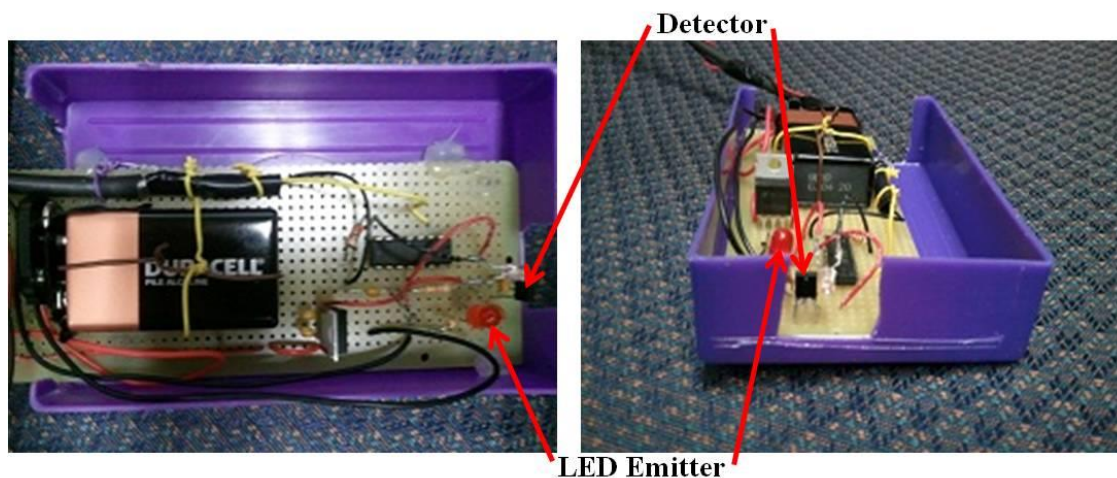


Figure 3-7: Configuration of the E/D device (top and front view).

### 3.1.1.4 PIV System

The specifications of the components of the PIV system are provided in following subsections. Figure 3-1 displays the configuration of the PIV set-up.

#### *3.1.1.4.1 Laser*

A dual Continuum Minilite-PIV 25mJ Nd:YAG laser generator with the maximum repetition rate of 15 Hz was used to create a laser beam with a wavelength of 532 nm. This repetition rate is compatible with a special Camera with a 30Hz image recording rates. Therefore, fifteen vector fields per second can be recorded.

#### *3.1.1.4.2 Optics*

A cylindrical lens was used to create a laser light sheet using the laser beam. A laser sheet with the thickness of 2mm (22 pixels) was used to minimize the error due to the out of plane motion of the particles. Considering the adequate thickness of the laser sheet for the experiment, no spherical lens was used to focus the laser light sheet.

#### *3.1.1.4.3 Particle Generation System*

To perform the PIV measurements, the flow under investigation needs be seeded with particles. A Laskin nozzle-type atomizer was used to generate seeding particles. The particle generator is designed and manufactured at the Boundary Layer Wind Tunnel Laboratory. As shown in Figure 3-8, a circular cylinder container filled with olive oil forms the main part of the particle generator. A Laskin-type nozzle connected to pressurized air supply is inserted in middle of the cylinder and the outlet of the generator is connected to tubing to introduce the particles (the uniform mixture of the air and olive oil droplets) into the flow in the tunnel test section. In the present experiments, two different generators are used, a small generator with the pressure limit of 40 psi and a large one with the pressure limit of 100 psi. The difference between these two generators is in the rate of the particle-laden flow that can be generated.



Figure 3-8: Configuration of Laskin nozzle-type particle generator

The Laskin nozzle-type particle generator generates olive oil particles with an average diameter of  $1 \mu\text{m}$ . The Stokes number characterizes the ability of the seeding particles to follow the fluid flow. The Stokes number is defined as follows:

$$S_t = \frac{\tau_p}{\tau_f} \quad 3.1$$

where  $\tau_p$  is the response time of a seeding particle, and  $\tau_f$  is any characteristic time scale of the fluid flow (Loth, 2000). The particles can be assumed to follow the fluid flow with the same velocity at any instance, when the Stokes number is much smaller than unity, meaning that the time required for the particle to assume the velocity of the fluid is negligible. In case of Stokes values closer to unity, the time lag between particle velocity and fluid velocity is no longer negligible. For  $S_t > 1$ , flow fluctuations will not affect the velocity of the particle. For the latter cases, the particle size is no longer appropriate for PIV measurements (Loth, 2000).

The response time of the particle,  $\tau_p$ , can be computed using the following relation (Loth, 2000):

$$\tau_p = \frac{\rho_p d_p^2}{18\mu} \quad 3.2$$

where  $\rho_p$  and  $d_p$  are density and diameter of the seeding particles, respectively.  $\mu$  is dynamic viscosity of fluid. In the present study, the particles are made of light olive oil with an average diameter of  $1 \mu\text{m}$ . The density of olive oil particles is  $\rho_p = 800\text{kg/m}^3$ . Air is the working fluid whose viscosity is considered to be  $1.98 \times 10^{-5} \text{ Kg/msec}$ . By substituting these values in equation (3.2), the response time is approximately equal to  $\tau_p = 2.25 \times 10^{-6} \text{ sec}$ .

Usually, three characteristic time scales are considered to determine the Stokes number, which are,  $\tau_{fD}$ , the time scale of macroscopic fluid motion,  $\tau_{fE}$ , the time scale of integral-scale turbulent motions, and  $\tau_{f\lambda}$ , the time scale associated with Kolmogorov scale.

The macroscopic time scale can be estimated using the following relation:

$$\tau_{fD} = \frac{l}{u_D} \quad 3.3$$

where  $l$  and  $u_D$  are the macroscopic characteristic length and velocity of the flow, respectively (Loth, 2000). In the present velocity measurements,  $u_D = U_{ref} = 4.12 \text{ m/sec}$ . The macroscopic characteristic length is defined based on the average chord length and therefore,  $l = 0.09 \text{ m}$ .

Thus the macroscopic time scale was estimated to be,  $\tau_{fD} = 0.022 \text{ sec}$ .

Substituting these values, the Stokes number is  $S_t = 1 \times 10^{-4}$ , which is much smaller than unity.

This indicates that the seeding particles can follow the macroscopic fluid motions with negligible lag.

An estimation value for the time scale associated with the integral-scale can be obtained using following relation:

$$\tau_{f\Lambda} = \frac{\Lambda}{u_{rms}} \quad 3.4$$

where  $\Lambda$  is the integral length scale and  $u_{rms}$  is the root square mean of characteristic velocity (Loth, 2000). The integral length scale, for an order of magnitude analysis similar to the one presented here, can be estimated to be  $0.35h$  (Piiro et al., 2003).  $h$  is the smallest geometric length scale in the flow. In the present measurements, this can be assumed as the smallest section of the blade (the tip). This leads to the value of  $h = 0.054\text{m}$  and the corresponding integral length scale of  $0.0189\text{ m}$ .  $u_{rms}$  value of  $1.8\text{ m/sec}$  is considered, which is the maximum value of  $u_{rms}$  in the tip region. Substituting these values in Eq. 3.4, the integral scale time is approximately equal to  $\tau_{f\Lambda} = 0.0105$ , resulting in a Stokes number of integral scale equal to  $S_t = 2.1 \times 10^{-4}$ . This number is much smaller than unity and therefore it can be assumed that the seeding particles can follow the integral-scale turbulent fluid motions with negligible lag.

The Kolmogorov scale is the scale of the smallest structures in a turbulent flow. The time scale associated with this scale can be estimated using the relation defined as follows:

$$\tau_{f\lambda} = \frac{\lambda_k}{u_\lambda} \quad 3.5$$

where,  $\lambda_k = \left(\frac{\nu^3}{\varepsilon}\right)^{1/4}$  and  $u_\lambda = (\nu\varepsilon)^{1/4}$  are the Kolmogorov length and velocity scales, respectively.  $\nu$  is the kinematic viscosity, and  $\varepsilon$  is the turbulent dissipation rate (Loth, 2000).

An estimation for  $\varepsilon$  and  $\nu$  can be acquired using the following equation (Piiro et al., 2003):

$$\varepsilon = \frac{u_{rms}^3}{\Lambda} \quad 3.6$$

Substituting the values, the turbulent dissipation rate is estimated to be  $\varepsilon = 3.09 \times 10^2 \text{ m}^2/\text{s}^3$ . This results in values of  $6 \times 10^{-5} \text{ m}$  and  $0.265 \text{ m/sec}$  for  $\lambda_k$  and  $u_\lambda$ , respectively. Therefore, the Kolmogorov time scale is found to be  $2.3 \times 10^{-4}$ . This leads to a Stokes number of 0.01. This

value can be assumed to be closer to unity compared to values obtained for other aforementioned cases. Hence, one can infer that in present velocity measurements, the particle size is not appropriate to follow the smallest turbulent fluid motions associated with the Kolmogorov scale.

#### *3.1.1.4.4 Image Acquisition System*

A monochrome camera (JAI CV-M2), with a frame rate of 30 fps, is used to image the flow for PIV measurements. The resolution of the camera is 1600×1200 pixels with a CCD chip size of 1inch. To obtain the best PIV resolution for the desired size of imaging area, a lens with focal length of 50mm is installed on the camera. The camera is connected to a PC which is equipped with a frame grabber card (DVR Express, IO Industries, London, ON, Canada) acquiring 8-bit images at a rate of 30 fps. The trigger output of the frame grabber is connected to the input gate of the synchronizer which is in turn triggered by the signal from the emitter/detector circuit. The frame grabber is connected to the camera via a Camera Link cable. The Camera Link cable transfers the data and controls the imaging trigger of the camera.

To control the timing of the laser pulses, a camera-laser synchronizer is used. This synchronizer is a four channel pulse/delay generator (555-4C, Berkeley Nucleonics Corporation, San Rafael CA). The synchronizer (timing unit) generates triggering signals both for the camera and the lasers, using an external triggering signal generated by the E/D circuit. Using pulse generator, the interval time between the two laser pulses is set.

#### *3.1.1.4.5 Sample Size*

To perform statistical analysis of the flow properties, the determination of an appropriate sample size of PIV recordings was essential. The sample size (n) in the present experiments is defined by the number of PIV velocity fields (image pairs). Since the velocity data has a normal



distribution, the sample size, with 95% confidence interval, can be calculated based on the following equation:

$$3.7$$

where  $n$  is the sample size,  $\sigma_x$  is the standard deviation and  $e$  is the maximum allowed error ( $e=\pm 0.08$  m/s) with 99.7% probability (Hamburg, 1970).

The azimuthally averaged axial velocity value in the near wake region of the rotor was considered to calculate the appropriate sample size. The standard deviation of the sample for measurements was 0.9 m/sec which is the average values of  $u_{rms}$  at  $r=1.05R$ . This value is obtained from the averaging the root mean square of axial velocity in the radial direction at  $X=R$  downstream of the turbine within the last window corresponding to the tip region (the highest standard deviation is expected in this region). Substituting these values into the above equation, the sample size was found to be  $n = 1140$  for measurements. In the experiments, the sample sizes were taken as  $n = 2000$ .

#### 3.1.1.4.6 Error Estimation

In PIV measurements, the main sources of error are the lack of accuracy in temporal and spatial measurements which can be combined and regrouped in terms of error due to the diameter of seed particles, density of particles, velocity gradients, out of plane motion of particles, dynamic range of grey-scale images, peak-locking and interpolation of velocity vectors (Cowen and Monismith, 1997).

To compute the largest error, the velocity gradients from the raw PIV data were considered. The

largest mean velocity gradients were calculated,  $\frac{\partial u}{\partial y} = 0.033$  and  $\frac{\partial v}{\partial x} = 0.008$  pixel/pixel. These

values are obtained in the last window corresponding to the tip region where the largest velocity

gradients occur. Using figure 5(e) in Cowen and Monismith (1997), the error associated with the velocity gradients are computed for RMS error and were found to be approximately  $\varepsilon_u = 0.10$  and  $\varepsilon_v = 0.04$  pixels.

In the present study, the size of the seeding particles is about  $1 \mu\text{m}$  (or 0.01 pixel); however, the area occupied by the image of the particle is one pixel and the exact position of the particle cannot be resolved. The error associated to the particle diameter of one pixel is estimated using figure 5(a) in Cowen and Monismith (1997) which is 0.06 pixels. However, this is the smallest size of particle provided by Cowen and Monismith (1997). Therefore, this error is scaled to the smaller particle size of 0.01 pixels. The variation of bias (peak-locking) error and RMS error as a function of particle diameter is provided by figure 13 in Prasad et al. (1992). According to this figure, the error corresponding to a particle size of 0.007 pixels are two times larger than those of one pixel particle diameter. Center of mass peak fitting is the scheme used by Prasad et al. (1992) which is subjected to relatively high peak-locking errors. However, in the present study, a three-point Gaussian peak fitting scheme, which is less susceptible to peak-locking (Cowen and Monismith, 1997), was used. According to Siddiqui (2002), the increase in error for this case can be approximated to be 50%. Hence, the error associated with the gradients can be modified by considering the error due to the particle size and therefore,  $\varepsilon_{u-dp} = 0.15$  and  $\varepsilon_{v-dp} = 0.06$  pixels.

The error related to the out-of-plane particle motion was estimated by computing the largest in-plane displacements (excluding the stream-wise velocity component). The out-of-plane particle velocity is not expected to be larger than the maximum of  $v$  or  $w$  (instantaneous velocity components), because the plane of velocity measurements were parallel to the free stream flow. The maximum value of instantaneous radial velocity was 0.98 m/sec or 1.96 pixels. Considering

the laser sheet thickness, approximately 2mm (or 22 pixels), the out-of-plane motion error is neglected.

The AGW averaging error is computed using figure 5(f) in Cowen and Monismith (1997). In this figure, AGW averaging error is plotted versus dynamic range. The dynamic range, defined as the difference in mean maximum particle intensity level and the mean background intensity level, is 121. In case of 8-bit CCD cameras it ranges from 100 to 150 counts. The error associated to this range is approximately,  $\varepsilon_{AGW} = 0.08$  pixels.

For each velocity component, the total error can be computed by summing the aforementioned errors. Therefore,  $\varepsilon_{uT} = 0.23$  and  $\varepsilon_{vT} = 0.14$  pixels. For a velocity vector, the total error is equal to  $\varepsilon_T = 0.27$  pixels or  $\varepsilon_T = 0.135$  m/sec. Considering the maximum mean velocity in the measurement plane, 4.12 m/sec, the total error is equal to 3.3%.

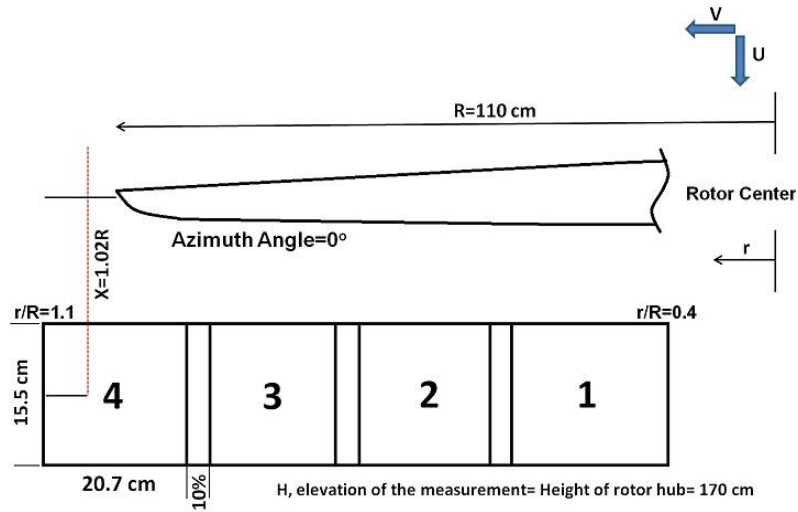
### 3.2 Experimental Procedure

The PIV measurements were performed in horizontal planes, behind the rotor at a vertical position corresponding to the center of the rotor (170 cm from the tunnel floor). In the measurements, the tail of the turbine nacelle was fixed using steel wires to prevent yaw motion of the rotor. Measurements were performed at two downstream locations ( $X=1.02R$  and  $X=2.02R$ ). The schematic drawing of the fields of the PIV measurements are displayed in Figure 3-9.

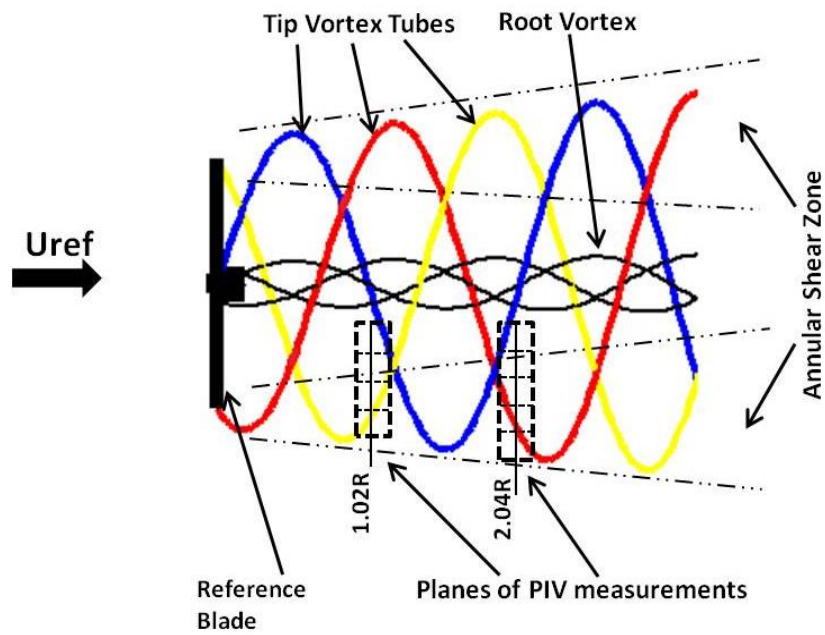
Throughout the measurements, the components of the PIV system, including the laser generator, synchronizer and the PC, were kept outside of the tunnel in order to avoid any flow modifications in the region of interest. The camera and particle generators were mounted inside

the tunnel, outside of the estimated region affected by the wake of the rotor, to have minimum effect on the flow (See Figure 3-1).

The wind speed of the tunnel was set to 4.12 m/sec. The average wind speed of the free stream flow was measured using a Pitot-static tube mounted 5 meter upstream of the turbine. The rotational speed was measured using a digital oscilloscope. The probes of oscilloscope were connected to the ground connection and the generator output to measure the frequency of the generator output. Also, another channel of the oscilloscope received the signal generated by the E/D device (See 3.1.13). Using the frequency of these signals, which were the same, the rotational speed was computed. The rotational speed of the turbine was set at 202 rpm resulting in a tip speed ratio of 5.67 and the local chord Reynolds number of 93,000 at 0.6R. According to Refan and Hangan (2012), the thrust coefficient on the rotor at the corresponding tip speed ratio is  $C_T = 1.06$ . The tip speed ratio is set in such a way that the turbine performs in the mode of the maximum power output based on the power curve shown in Figure 3-4. For this purpose, the rotational speed of the rotor is controlled by applying a series of electrical loads to a circuit which is connected to the 3-phase generator output of the turbine rotor. More details on the wind turbine itself and the electrical controls can be found in Refan and Hangan (2012).



(a)



(b)

Figure 3-9: Schematic drawings of the field of PIV measurements

### 3.2.1 Alignment and Calibration

During the calibration, the laser head and the camera lens were adjusted in such a way that the camera lens axis was perpendicular to the light sheet. Also the light sheet thickness was checked to be approximately 2 mm and be perpendicular to the ground plate of the apparatus. This process was repeated for each of the two lasers independently because of the possible misalignment of lasers, however, no significant misalignment of the two components of the laser was observed. Moreover; the position of the camera was set to obtain the proper imaging area.

The region of interest for the flow measurements at each upstream and downstream location was 80 cm  $\times$  15 cm. Due to camera resolution and spatial restrictions, the flow fields in this region cannot be measured in a single window. Thus, a row of four radially distributed measurement windows were used to cover the region of interest at each axial location (see Figure 3-9). The dimensions of the each measurement window were 20.7 cm in the radial direction and 15.5 cm in the axial direction. It should be noted that the relative position of the windows (tiles) is crucial in order to obtain continuous and reliable results in the entire region of interest. In other words, an overlap area should exist between each two neighboring windows. This overlap is used in the post-processing stage to patch the windows. The overlap area should have a proper size in order to acquire continuous flow field at boundaries of the two adjacent PIV measurement planes. Preliminary measurements were carried out in the windows with the overlap area of less than 4% of the radial size of each window. The acquired results showed discontinuity within these regions. Therefore, the overlap between the windows was set equal to 10% of the radial size of each window to obtain better continuity in the velocity components. To accurately determine the fields of measurements with the corresponding overlap regions, a calibration board of the same size as the entire region of interest was manufactured and used (See Figure 3-1 (c)). The

measurements in each window have to be performed at the same height from the tunnel floor. To guarantee this criterion, the board had to be mounted at the same height from the tunnel floor for the measurements in each window. For this purpose, the calibration board was installed at the bottom of a table with adjustable height. Prior to each set of data acquisition within each window, the table was placed at the exact location of the previous measurements. Afterwards, a calibration image was recorded to reference the particular measurement window with respect to the adjacent windows, which is required in post-processing of the vector fields and patching the windows.

### **3.2.2 Phase- lock Technique**

Since the PIV measurements were performed in planes at fixed spatial locations, in order to extract phase information and compute phase-averaged characteristics, the measurements needed to be phase-locked. Hence, a phase-locking technique was employed using a photo emitter/detector (E/D) device. The device was mounted at a fixed location on the top of the turbine nacelle immediately behind the rotor (See Figure 3-1 (a)). A small mirror was installed at the back of one of the blades. Every time the corresponding blade passed the E/D device, it provided a trigger signal for the PIV system. Measurements at different blade azimuth angle were made by defining an appropriate time delay between the trigger signal from the device and the signal provided by the synchronizer to trigger the laser and camera. The time delay was calculated based on the rotational speed of the rotor. Using this method, eight angular positions of the blade between 0 and 105 degrees with an increment of 15 degrees were covered at each measurement window for two axial locations. It should be mentioned that the 0 degree corresponds to the position at which one of the blades is at a horizontal position in the right hand

side of the hub from the front view (see Figure 3-9 and Figure 3-10). The blade angle of zero was set using a digital inclinometer (see Figure 3-10).

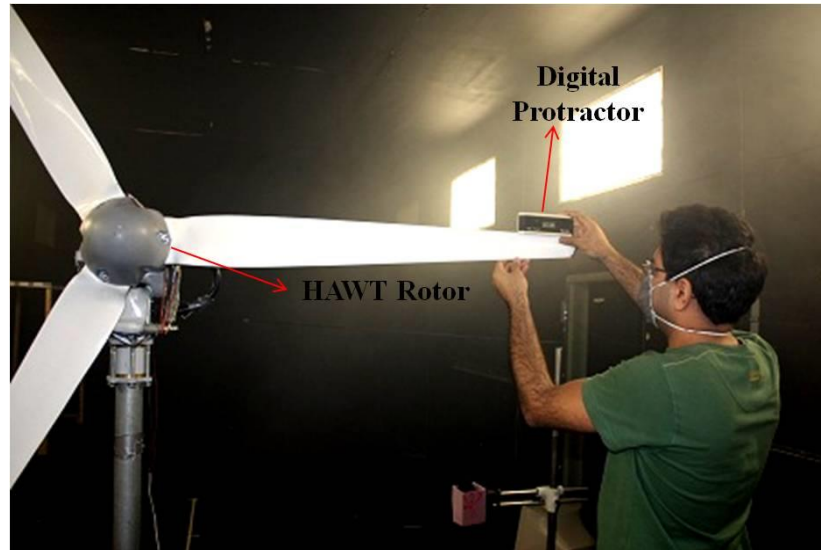


Figure 3-10: Positioning of the turbine rotor in the reference angular position using the digital inclinometer.

### 3.2.3 Seeding Process

One major challenge of PIV measurements in a large-scale wind tunnel is the proper particle distribution. For the present PIV measurements, the dimensions of the measurement area are typically in the range of 10–20 cm and the proper particle distribution within this region becomes a major challenge. Areas of low particle density within the measurement area result in inaccurate estimation of the flow velocity.

Siddiqui et al. (2008) used the PIV technique for wind mapping in complex topographies in a large wind tunnel setup. The particles were introduced to the flow locally. They developed and implemented a scheme to detect and remove the regions with low particle density in each image pair. This method is adequate where the region of the interest is of the same order as the PIV



frame size (typically 10-20 cm). We implemented this technique in the previous chapter and found out that this technique fails to produce acceptable results, due to inconsistent statistics, and failure of the patching technique due to low particle density in the overlap regions.

Several approaches were applied to guarantee that the particles are uniformly distributed with appropriate density within the measurement window resulting in high signal-to-noise ratio of the PIV images. Through the preliminary measurements, the particles were introduced to the flow locally at different axial locations upstream as well as downstream of the turbine. The PIV images revealed that the particles were not distributed uniformly particularly at the edges of the images which are the crucial regions in patching the adjacent PIV windows. This resulted in discontinuities in the acquired flow field within the patching zones.

This issue could be overcome by filling the whole tunnel with olive oil particles. Due to very large dimensions of the wind tunnel (total volume equal to approx. 2000 m<sup>3</sup>), seeding the entire air circulating through the wind tunnel was a challenge. Consequently, two large capacity seed generators were used to fill the entire wind tunnel (See Figure 3-11)). However, the acquired images showed that uniformity of the seed distribution was not satisfactory due to the large velocity gradient behind the turbine as well as rapid dispersion of the olive oil particles because of highly turbulent nature of the flow. Therefore, to improve the seed distribution, an additional T-shaped seed distributor was placed upstream of the turbine to introduce seed particles locally (See Figure 3-11)). Using the three particle generators, it was assured that the particle distribution within the images was uniform.



Figure 3-11: Seed generators within the test set-up

### 3.2.4 Image Acquisition

For each experiment, after the calibration of the system, the particle generators were turned on and the wind tunnel was set to run at the desired wind speed. Few sample images were taken and processed prior to the final image acquisition in order to ensure adequate  $\Delta t$ , particle density, illumination, focus, etc. A total of 4,000 images (2,000 image pairs) were acquired for each run corresponding to the combination of one measurement window and one angular position of the blade. For each run, the time interval between the two laser pulses was adjusted based on the preliminary measurement of the mean velocity within the wake. Typically, the time intervals varied between 140 and 300  $\mu\text{sec}$ . Since the CCD camera was looking upwards, the flow direction within the images is from top to the bottom. A sample of the instantaneous image pair is displayed in Figure 3-12 (a).

### 3.2.5 Image Processing

The TSI Insight software was utilized to perform the image analysis and extract the raw velocity fields using the cross correlation technique for each interrogation window. The interrogation window was set to be  $48 \times 48$  pixel with an overlap of 50%. The uncertainty in the velocity measurement was computed for the case with the largest velocity gradients, following the procedure described in section 3.1.1.4.6. This provides a conservative estimate of the velocity errors in the present study. The uncertainty in the velocity measurements was estimated to be about 3.3% of the free stream velocity.

Figure 3-12 presents an example of the instantaneous velocity field at the tip of the blade (4<sup>th</sup> tile in Figure 3-9 (a)) for the  $45^\circ$  azimuth angle, at  $X=1.02R$  downstream of the rotor. Although the particle distribution was uniform within all images, stripe-shaped regions with low laser light intensity were found to exist in the images (see Figure 3-12 (a, b)). This can be attributed to the very small air bubbles trapped within the glass window of the tunnel through which the laser beam was transmitted. The poor signal-to-noise-ratio in low laser light intensity regions generated spurious vectors. Since the spatial position of the stripe regions is fixed in the entire dataset, locating their coordinates was a simple task. For each measurement tile, a binary image was created based on the corresponding image pairs. Figure 3-12 (a) and (b) displays an instantaneous PIV image pair, and the corresponding binary image is shown in Figure 3-12 (c). The black stripes in the binary image represent the regions with low light intensity. In the next step, these binary images were used to remove the false vectors that were associated with the stripe regions. That is, in a given raw velocity field, all velocity vectors that were located in the black regions in the corresponding binary image were assigned as NaN (not-a-number). The spurious vectors in the white (non-stripe) regions were identified using statistical median and

global outlier filters (Siddiqui et al., 2001), and were replaced by the local median vector. Note that the NaN regions were not considered in the spurious vector correction scheme. The velocity field after spurious vector correction is shown in Figure 3-12 (d). The instantaneous vector map is superimposed on the contour plot of vorticity normalized by the rotor angular velocity. The vorticity is computed using the relation,  $\omega = \frac{\partial v}{\partial X} - \frac{\partial u}{\partial Y}$  considering counter clockwise rotation as positive. Note that in the present study,  $v$  and  $u$  are radial and axial components of velocity, respectively and  $X$  and  $Y$  represent axial and cross-wind directions, respectively. The vector map corresponds to the region representing the tip area. Therefore, one can expect to observe a tip vortex. Both the image pairs and the velocity/vorticity plot clearly depict the tip vortex. This tip vortex tends to wander within the window of measurement due to its intermittent behaviour. Qualitative assessment of this behaviour of tip vortex is presented in Chapter 4. The process of removing false vectors is performed for all experimental runs at both axial locations and all eight azimuth angle of the turbine blade. In general, it was found that less than 1% of the velocity vectors in the white regions were spurious.

In the final step, the velocity calibration is performed using a MATLAB program to convert the particle displacements to velocity (m/sec). Initially, the calibration ratio corresponding to each tile of calibration board, image scale (in mm/Pixel), is determined using the calibration images. Thereafter, the calibration ratio and the time interval (in  $\mu\text{sec}$ ) are input into the program to convert the particle displacement fields (in pixel per delta t), obtained from the image processing stage, to velocity fields (in m/sec).

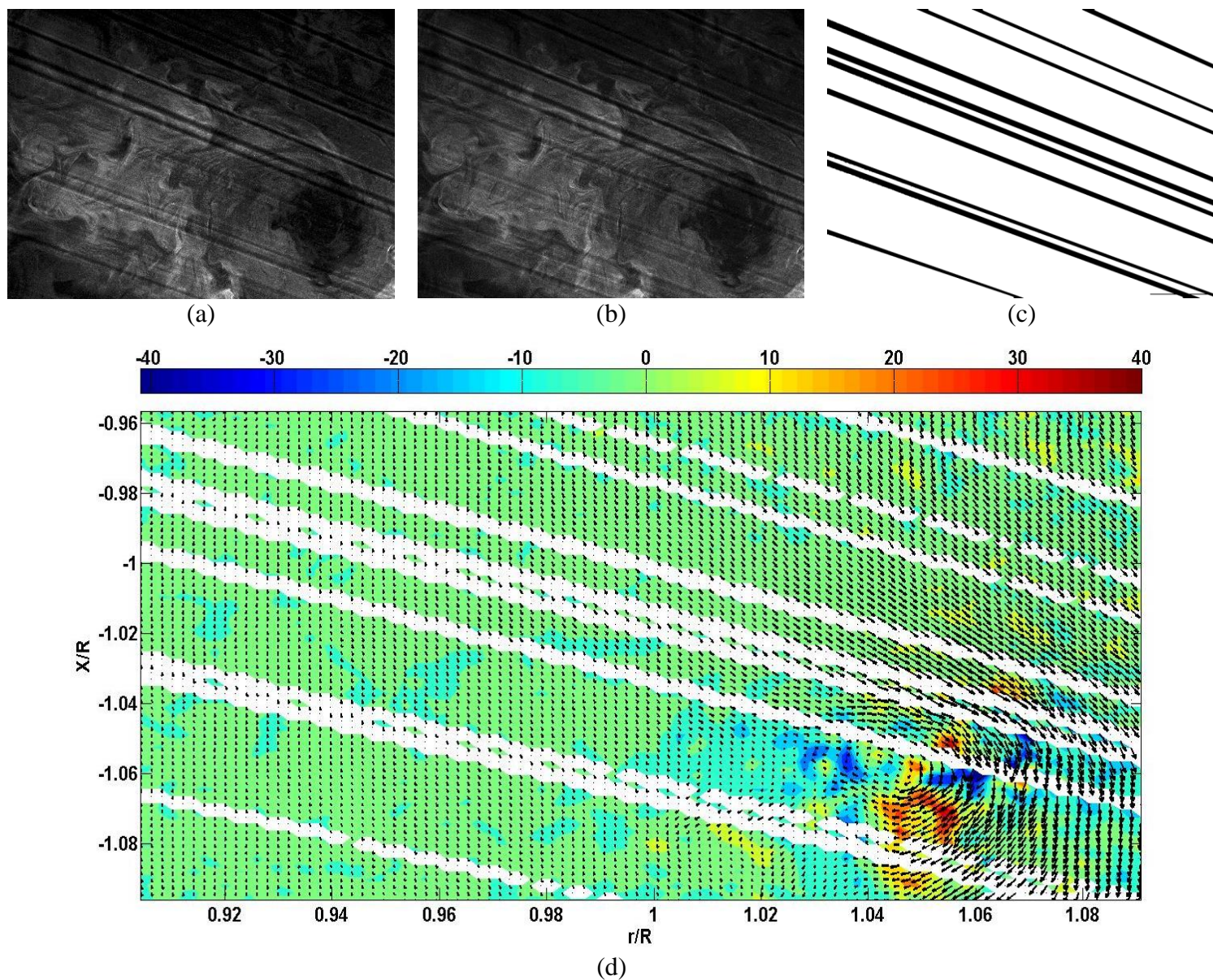


Figure 3-12: a, b) An Instantaneous image pair, c) Corresponding binary image, d) Corresponding instantaneous velocity field obtained at  $X=1.02R$  downstream of turbine in the 4<sup>th</sup> tile for the blade azimuth angle of  $45^\circ$ . The vector map is superimposed to the contour map of vorticity normalized by the rotor angular velocity.

### 3.2.6 Patching Process

A technique similar to the one used by Dobrev et al. (2008) and Xiao et al. (2011) was applied to patch the measurement windows. The mean velocity as well as time-averaged turbulence characteristics at each point within the overlap region of two adjacent tiles is computed by averaging the values of the corresponding parameter within the corresponding tiles. Using this method, one can have a proper assessment of the flow structures of the rotating wake, since the velocity field of the entire measured area can be presented at one large window. At each axial location, a patched window is generated for each azimuth angle. Samples of patched windows can be found in the next Chapter where the results including velocity fields and contour plots related to different characteristics are presented (see e.g. Figure 4-3). Note that the patched windows are only generated for the time-average characteristics. The tiles need to be synchronized in order to produce instantaneous patched windows.

## **4 Velocity Measurements using PIV Technique- Results and Discussion**

In this chapter, the results acquired from the velocity measurement within the near-wake region of the HAWT using the PIV technique are presented. The main objectives of the measurements and the analysis presented in this chapter are:

- To quantify the flow characteristics including mean and turbulent components of the velocity field.
- To study the flow structure, particularly the vortex structure within the rotating wake shortly downstream of the turbine.
- To assess the validity/limitations of the Blade Element Momentum (BEM) Theory
- To tackle scaling effects arising from variation of local chord Reynolds number

The chapter includes three sections. The first section presents the results in terms of mean and turbulent flow fields. The mean flow results are compared with those provided by previous investigators, particularly the MEXICO experiment (Schepers et al., 2012).

In the second section, an assessment of the validity and limitations of the BEM theory to estimate the flow field within the near wake region is presented.

In the final section, scaling effects are studied with the focus on the influence of local chord Reynolds number on the rotating wake flow field.

### **4.1 The Velocity Field**

The calibrated velocity components were determined based on the velocity vector fields obtained from the image processing procedure described in Chapter 3, using a Matlab program.

The results regarding the mean and turbulent flow components are presented in the form of contour plots and radial and axial profiles. All velocities and turbulence characteristics are normalized by the free stream/ reference wind speed ( $U_{ref}$ ) and all dimensions are normalized by the rotor radius ( $R$ ).

#### 4.1.1 Qualitative Analysis of the Velocity Field in the Near-wake Region

Figure 4-1 presents streamlines of instantaneous velocity field at the tip of the blade (4<sup>th</sup> tile in Figure 3-9 (a),  $100\text{cm} < r < 120\text{cm}$ ) for  $105\text{cm} < X < 120\text{cm}$  downstream of the rotor. The streamlines are superimposed to instantaneous vorticity contour plots. The vorticity is computed using the same relation described in section 3.2.5. As already discussed in 3.2.5, the tip vortex wanders within the measurement window. In Figure 4-1, the streamlines of the instantaneous velocity field is presented for the  $30^\circ$  azimuth angle, since for this angle the wandering vortex tends to remain mostly within the window of measurements. In each instantaneous velocity field, the location of the center of the tip vortex is shown with a red arrow. Since the measurements are phase-locked (see Chapter 3 for the process of phase-locking), the time interval between each two image pair is associated with the rotational speed of the turbine. The time interval between two instantaneous velocity field is calculated using the rotational speed of the rotor, 202 rpm (3.67 Hz or 0.297 sec), and is equal to  $t = 0.297$  sec. In addition, in each instantaneous velocity field, NaN (not-a-number) data points within the stripe regions are replaced by a value obtained from averaging the data points surrounding the corresponding point.

As shown in Figure 4-1, the location of the core of the tip vortex in each snapshot is associated with the highest values of vorticity. Moreover, it can be observed that tip vortices mostly form at  $r > 100$  cm ( $r/R > 1$ ). This indicates the wake expansion, since the tip vortices are generated at the



radial positions larger than radius of the rotor showing an increase in the width of the wake. Overall the instantaneous velocity fields clearly depict the intermittent (wandering) nature of the tip vortex.

Due to this intermittent behavior of the tip vortices, time-averaged vorticity field do not provide a clear picture of the vortex. Figure 4-2 presents the streamlines of mean velocity field at the tip region (4<sup>th</sup> tile in Figure 3-9 (a),  $100\text{cm} < r < 120\text{cm}$ ) for eight different blade azimuth angle for  $105\text{cm} < X < 120\text{cm}$  downstream of the turbine. The streamlines are obtained based on radial velocity and axial velocity deficit. The streamlines are also superimposed to contour plots of mean radial velocity. The negative sign of radial component represents inward flow (towards the centre of the rotor), while the positive sign corresponds to the outward flow (towards the tip of the blade). One can consider the presence of these regions as the cross-section of a vortex which causes the inward and outward motion of the fluid within this area. However, due to the intermittent behavior of the tip vortex, this mean flow structure is only depicted as deflections in streamlines of mean velocity field. Comparison of the contours of radial velocity component at different azimuth angles displays the gradual movement of the vortex region in the axial direction. In the blade frame of reference (similar to Dobrev et al. (2008) and Yang (2011)), this axial movement can be attributed to the dynamics of the helical tip vortices which after generation from the tip, rotate with respect to the blade and move in the axial direction due to the axial momentum of the flow (see Figure 1-2 (b) and Figure 3-9 (b)). For  $\theta \geq 90^\circ$ , the vortex region represents the tip vortex originating from the next blade. This vortex region (area of deflected streamlines) is mainly located at  $r > 110\text{ cm}$  ( $r/R > 1$ ) which demonstrates the wake expansion. In addition, as shown in streamlines, one can infer that the flow within the tip region ( $r > 100\text{ cm}$ ,  $r/R > 0.9$ ) is strongly phase dependent.

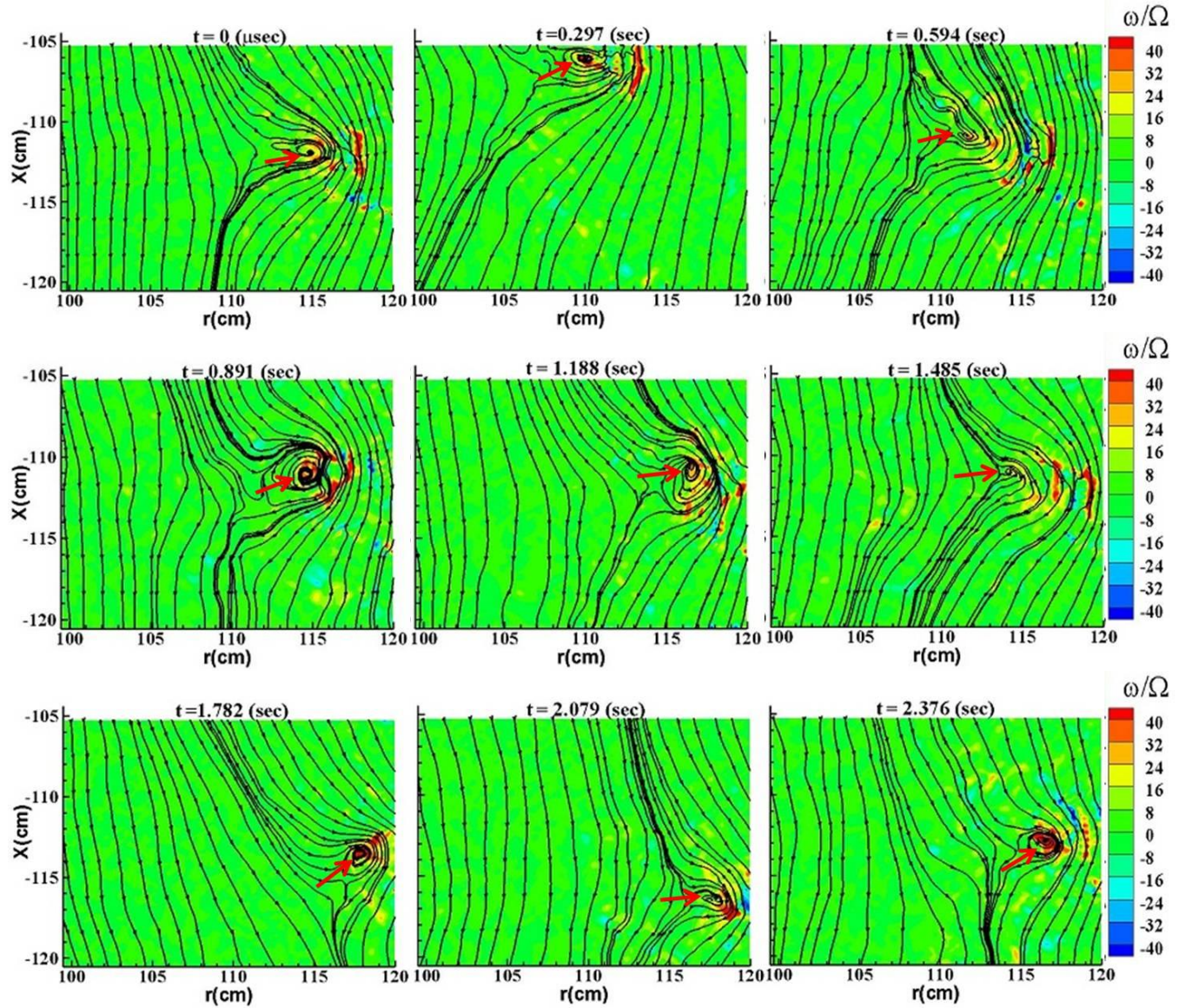
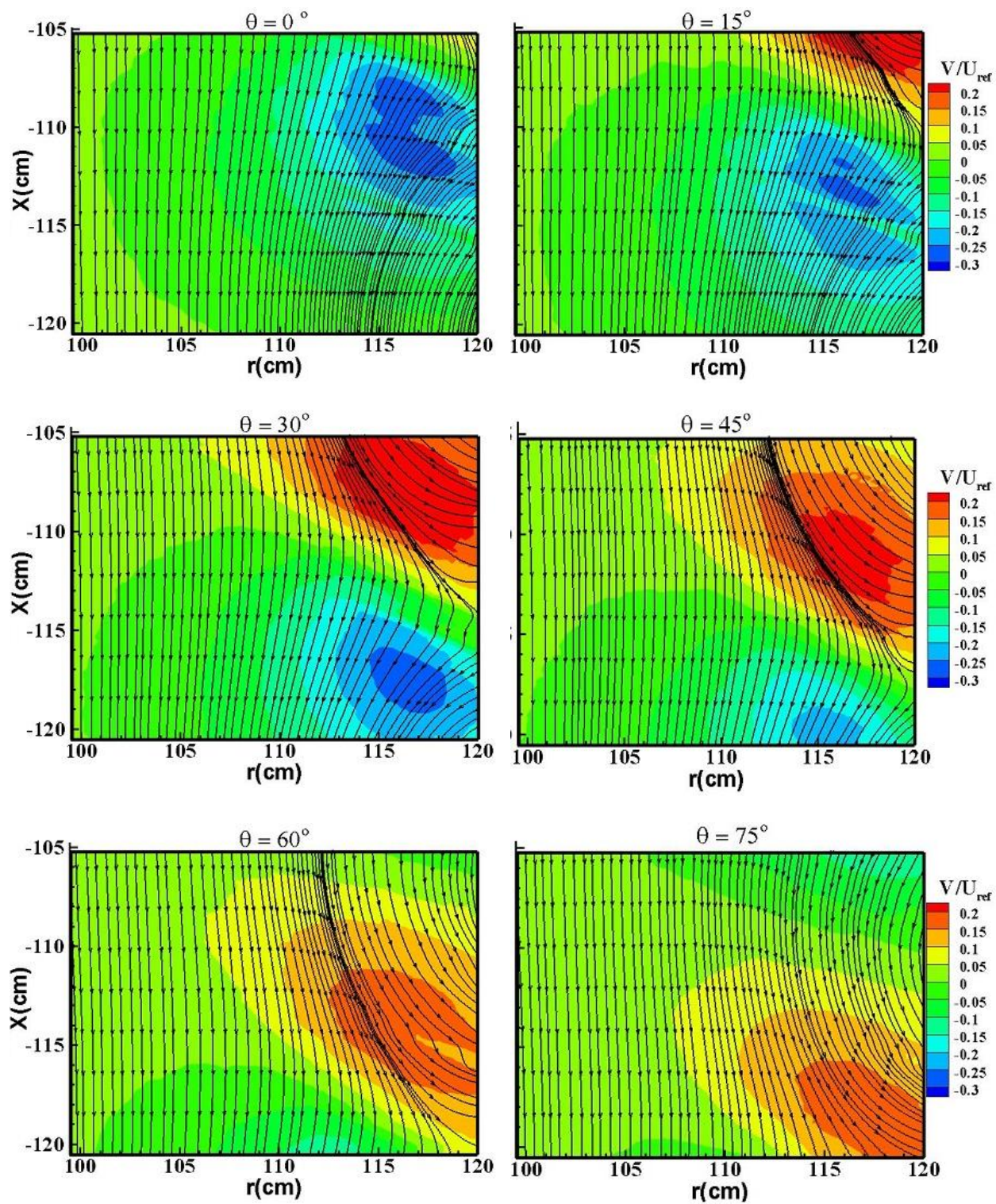


Figure 4-1: Streamlines of instantaneous velocity field behind the rotor for  $105\text{cm} < X < 120\text{cm}$  downstream of the turbine. Streamlines are presented for  $30^\circ$  azimuth angle. The streamlines are superimposed to instantaneous contour plots of vorticity normalized by rotational speed of rotor. The location of tip vortex in each instantaneous plot is shown by a red arrow.



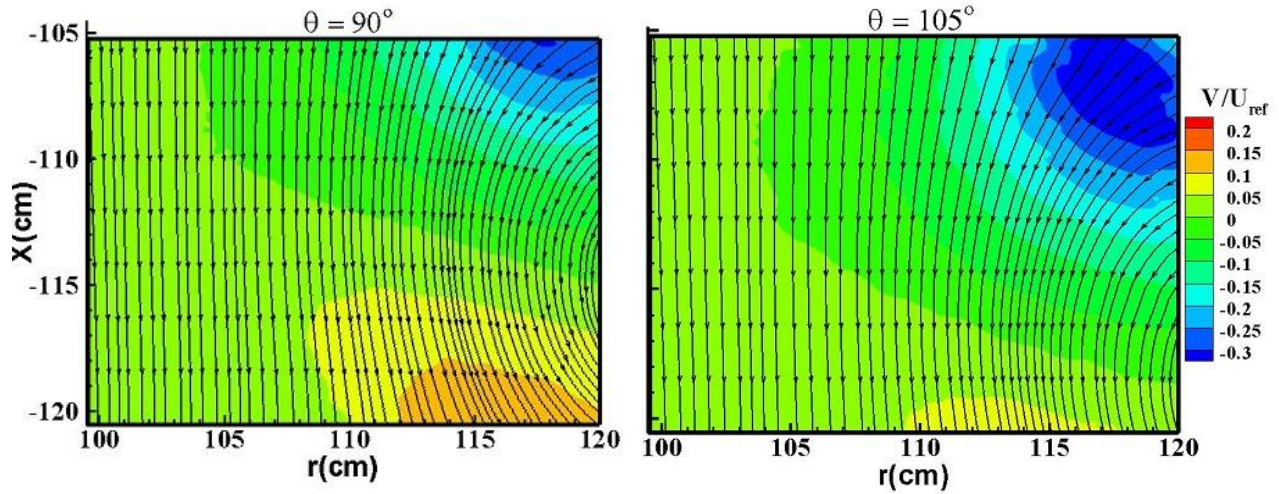


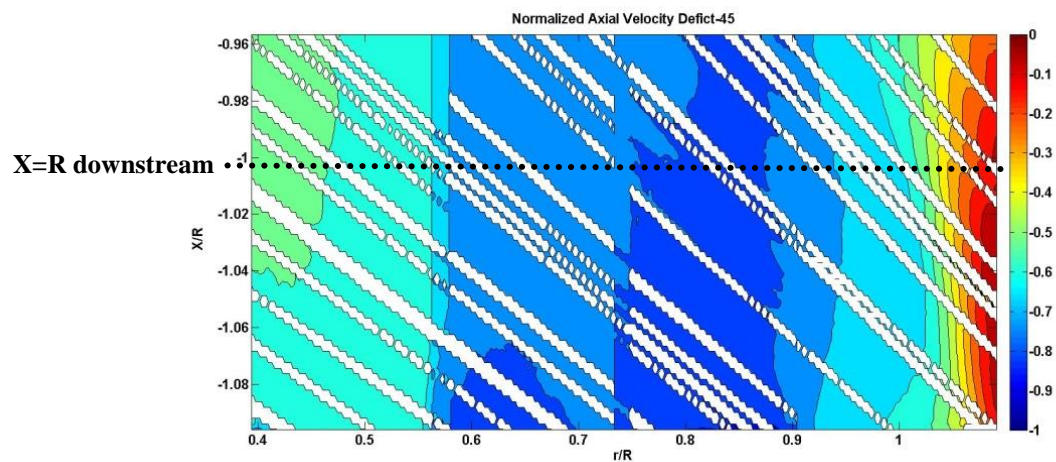
Figure 4-2: Streamlines of mean velocity field behind the rotor for  $105\text{cm} < X < 120\text{cm}$  downstream of the turbine for eight different azimuth angles of the blade:  $0^\circ$ ,  $15^\circ$ ,  $30^\circ$ ,  $45^\circ$ ,  $60^\circ$ ,  $75^\circ$ ,  $90^\circ$  and  $105^\circ$ . The streamlines are superimposed to contour plots of mean radial velocity normalized by reference wind speed.

### 4.1.2 Quantification of the Mean Flow Field in the Near-wake Region

To obtain the mean velocity field for a given experimental run, the time series were extracted at each grid point from the sequence of corrected instantaneous velocity vector fields. The mean velocity was obtained at each grid point by averaging the time series. Note that in a given time series, all points associated with the blanked regions in the vector field (with NaN values / non-numeric values) were excluded from the mean velocity computation.

#### 4.1.2.1 Axial Velocity

Figure 4-3 displays the patched contour plots of axial velocity deficit, for  $0.96 < X/R < 1.08$  downstream of the rotor for three different blade azimuth angles of  $45^\circ$ ,  $60^\circ$  and  $90^\circ$ . The axial velocity deficit is defined as  $-(1-U/U_{ref})$  where  $U$  is the time averaged velocity. It can be seen that the velocity magnitude increases closer to the blade tip; however, the complete recovery of the axial velocity component only occurs at  $r/R > 1$  (Vermeulen, 1978; Vermeer et al., 2003). This demonstrates the expansion of the rotating wake.



(a)

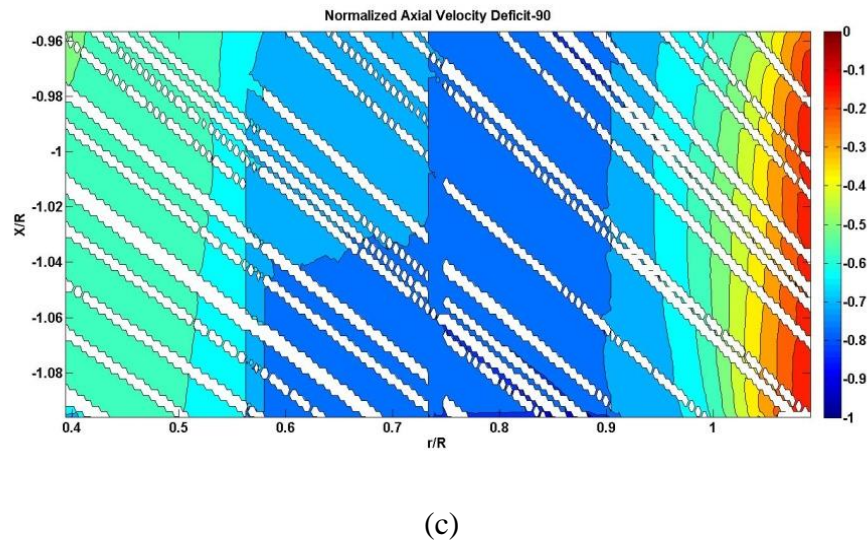
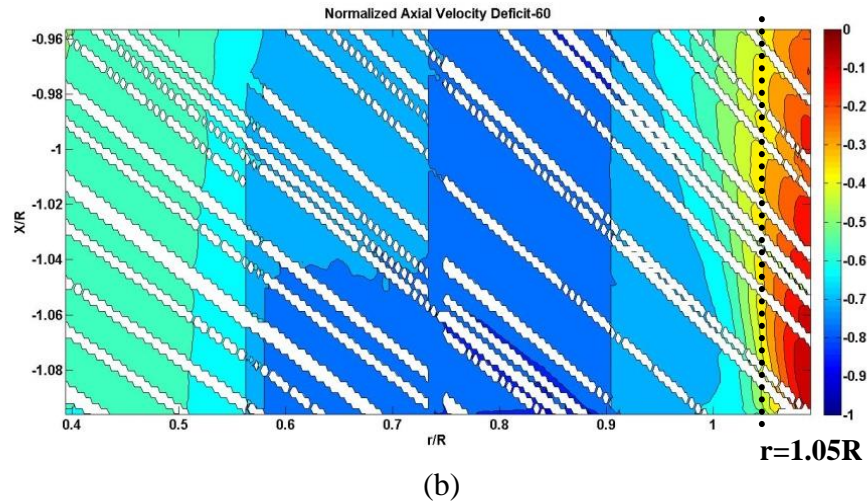


Figure 4-3: Contours of mean axial velocity deficit ( $-[1-U/U_{ref}]$ ) behind the rotor for  $0.96 < X/R < 1.08$  for three different azimuth angles of the blade: a)  $45^\circ$ , b)  $60^\circ$ , c)  $90^\circ$

Figure 4-4 present radial profiles of normalized axial velocity deficit for eight different azimuth angles at  $X=R$  (see Figure 4-3 (a)) and  $X=2R$  downstream of the turbine, respectively. It can be seen that in accordance with previous investigations (Magnusson, 1999; Sørensen and Shen, 2002; Watters and Masson, 2007), at  $X=R$ , the maximum axial velocity deficit ( $-0.7 \sim -0.75$ ) occurs at  $0.55 < r/R < 0.9$ . This indicates that the maximum power extraction from the wind is happening in the median to tip part of the blade section. At  $X=2R$  downstream of the rotor, the

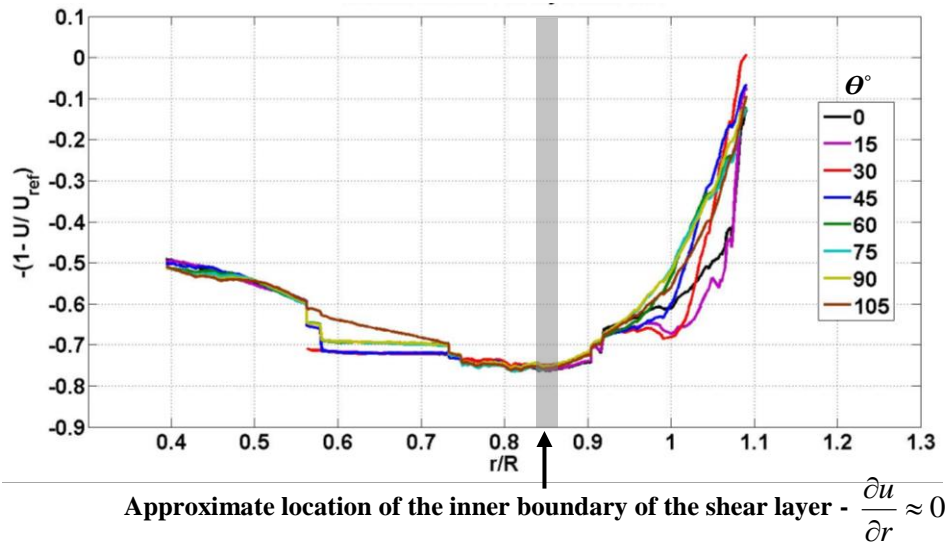
region at which the maximum velocity deficit occurs, corresponds to  $0.4 < r/R < 0.8$  which is closer to the center of the wake. This indicates the momentum transport toward the centre of the wake and therefore, wake development (Magnusson, 1999; Watters and Masson, 2007). It is expected that farther downstream, the peak of velocity deficit would decrease due to the process of momentum transport. This is the location where the shear layer reaches the axis of the wake.

As the wake develops downstream, it expands in the crosswind direction (see Figure 3-9 (b)). The wake expansion can be determined by tracing the radial location at which the axial velocity reaches the reference wind speed. While this happens at  $r/R \sim 1.1$  for  $X=R$ , it shifts to  $r/R \sim 1.2$  for  $X=2R$ .

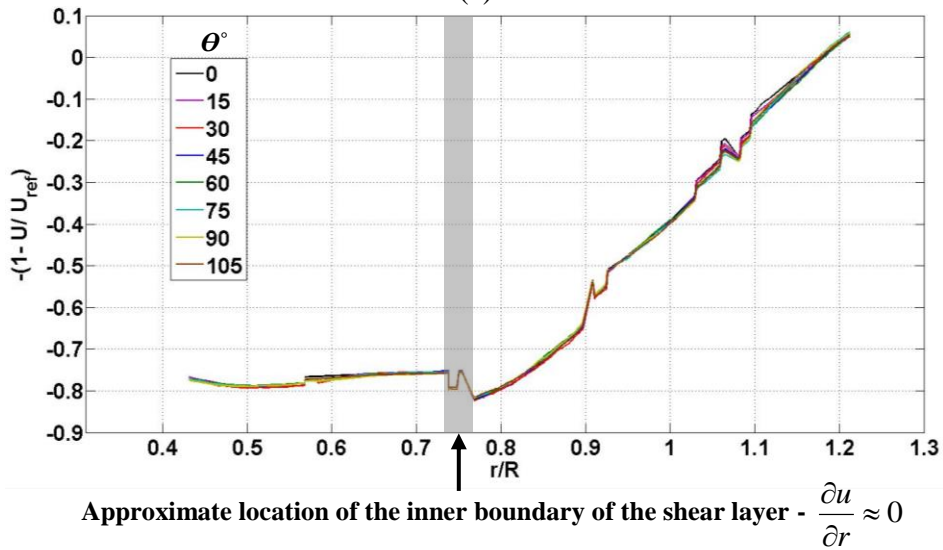
The shear zone is the zone at which large velocity gradients are expected. Theoretically, the location of the maximum gradient of the streamwise velocity ( $(\frac{\partial u}{\partial y})_{\max}$ ) is at the center of the shear layer, while the velocity gradient is zero at the boundaries of the shear layer. In the present experiment, the location of inner boundary of the shear layer is determined by finding the location where the gradient of streamwise velocity is approximately zero ( $\frac{\partial u}{\partial r} \approx 0$ ). The approximate radial position of this location is displayed in Figure 4-4 (a) and (b). It can be observed that for  $X=R$  the shear zone is located at  $0.85 < r/R < 1.1$ , while it expands  $0.75 < r/R < 1.2$  further downstream at  $X=2R$ .

In terms of phase dependence, it can be observed (Figure 4-4 (a)) that at  $X=R$ , the axial velocity deficit is phase dependent for  $r/R > 0.9$  and almost independent of phase for  $r/R < 0.9$  (similar to the behavior reported by Schepers et al., 2012). Further downstream, at  $X=2R$  the axial velocity is independent of azimuth angle in the entire measurement region. Close to the rotor, at  $X=R$ , the flow structure is dominated by the tip vortex while further downstream, at  $X=2R$ , the tip vortex

structure seems to weaken. This behavior is clearer in the downstream evolution of the axial velocity deficit at  $r=1.05R$  (see Figure 4-3 (b)) shown in Figure 4-4 (c) for four different azimuth angles.

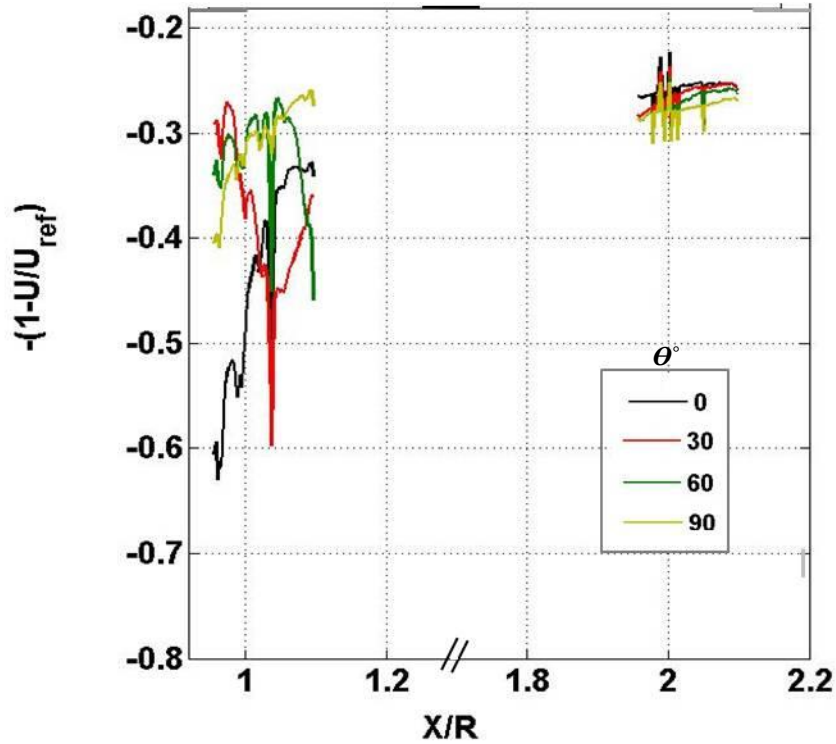


(a)



(b)





(c)

Figure 4-4: Radial profiles of axial velocity deficit for eight azimuth angles of blade a) at  $X=R$ , b) at  $X=2R$ , c) Axial Profiles of axial velocity deficit for four azimuth angles of blade at  $r=1.05R$ .

#### 4.1.2.2 Radial Velocity

Contour plots of radial velocity component are displayed in Figure 4-5 at three different azimuth angles of the blade, for  $0.96 < X/R < 1.08$  downstream of the turbine. For  $r/R < 0.9$ , the magnitude of radial velocity is very small ( $-0.05 < V/U_{ref} < 0.05$ ) for the three azimuth angles. The region corresponding to  $r/R > 0.9$  is where the tip vortices appear. As discussed in the qualitative analysis of the velocity field (see 4.1.1), contours of radial velocity within the tip region for different azimuth angles display the gradual movement of the vortex region in the axial direction which can be associated to the dynamics of the helical tip vortices (see Figure 1-2 (b) and Figure 3-9 (b)).

Figure 4-6 (a) and (b) display the radial profiles of normalized radial velocity for eight azimuth angles of the blade at  $X=R$  and  $X=2R$  downstream, respectively. Similar to the behavior of the axial velocity, the radial velocity is strongly dependent on phase near the rotor at  $X=R$  while it becomes independent of phase angle further downstream at  $X=2R$ . The phase dependency at  $X=R$  is very pronounced for  $r/R > 0.9$  as a result of the passage of the tip vortex in the axial direction dynamics. For  $0.6 < r/R < 0.9$  the radial velocity magnitude is very small and independent of azimuth angle. For  $r/R < 0.6$ , the magnitude increases with small variation due to root vortices. Moreover, comparison of different radial profiles at  $X=R$  shows that the maximum radial velocity is associated with the azimuth angle of  $30^\circ$  with the magnitude of 0.24 at  $r \sim 1.05R$ . A plausible reason can be the fact for this azimuth angle of the blade the region of high outward flow motion corresponding to the tip vortex is exactly located at  $X=R$  (see also Figure 4-2).

Axial profiles of normalized radial velocity at three different radial positions,  $r=0.45R$ ,  $r=0.85R$  and  $r=1.05R$  (see Figure 4-5 (b)) are presented in Figure 4-7 (a), (b) and (c), respectively. As shown in Figure 4-7 (a) and (b), the radial velocity magnitude is very small at  $r=0.45R$  and  $r=0.85R$ . It can also be observed that at  $r=0.85R$ , the radial velocity is independent of azimuth angle; however, at  $r=0.45R$  it varies with respect to the phase angle because of the influence of root vortices (see Figure 1-2 (b)). At  $r=1.05R$ , the axial profiles clearly show the vortex structure of the wake at this region (See Figure 4-7 (c)). The peak of each profile represents the position of the tip vortex. Hence, the axial movement of the peaks can be interpreted as the helical path of the tip vortex. Note that the peak corresponding  $\Theta \geq 90^\circ$  represents the vortex originating from the next blade. The patterns of these profiles are comparable with those shown in Figure 3-9 (b) and represent the helical trajectories of the tip vortices.

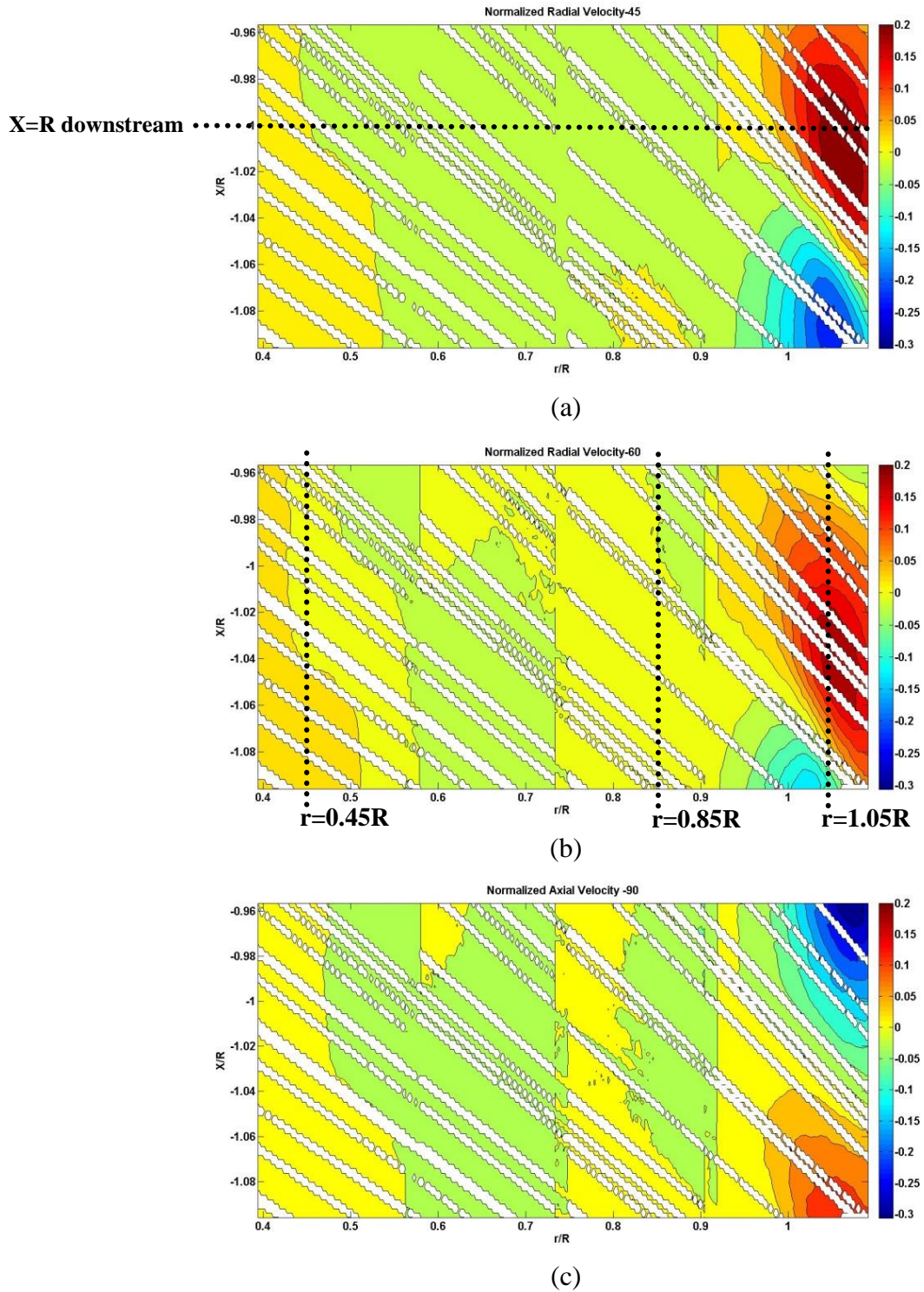
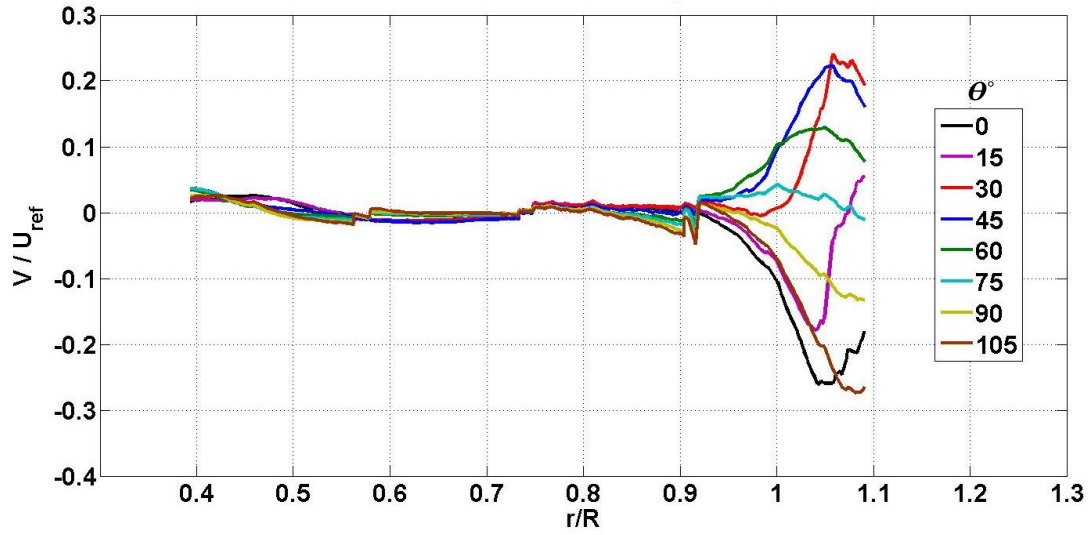
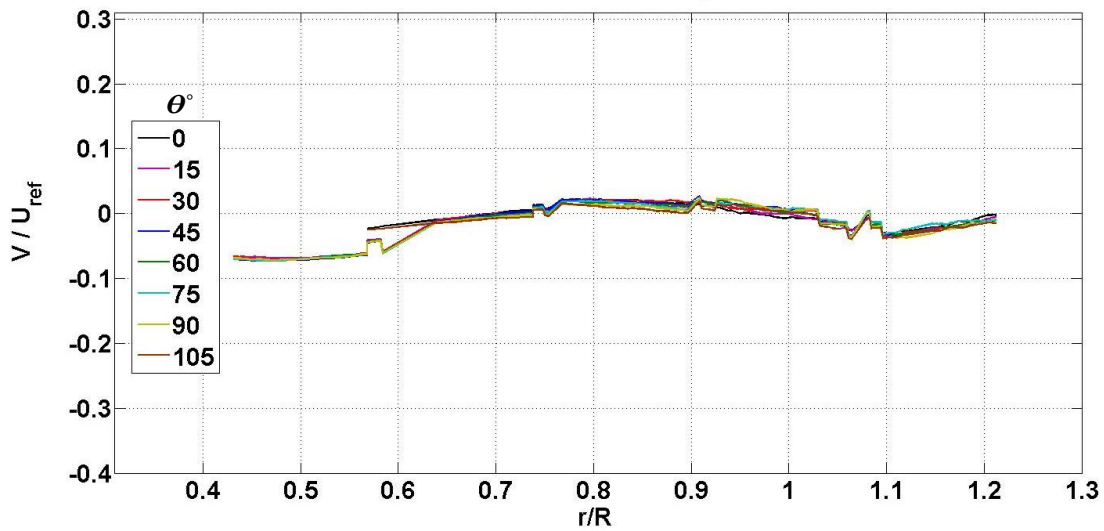


Figure 4-5: Contours of the normalized radial velocity for  $0.96 < X/R < 1.08$  downstream the turbine for three different azimuth angles of the blade: a) 45°, b) 60°, c) 90°



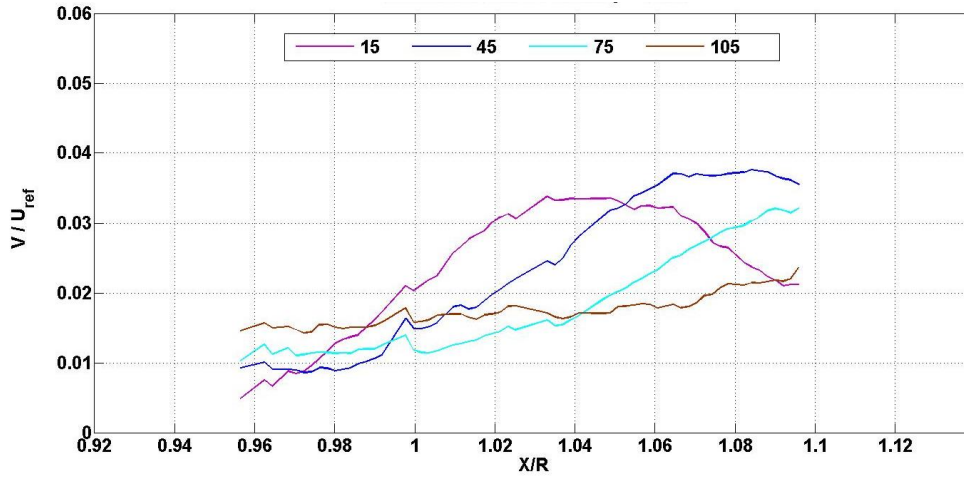
(a)



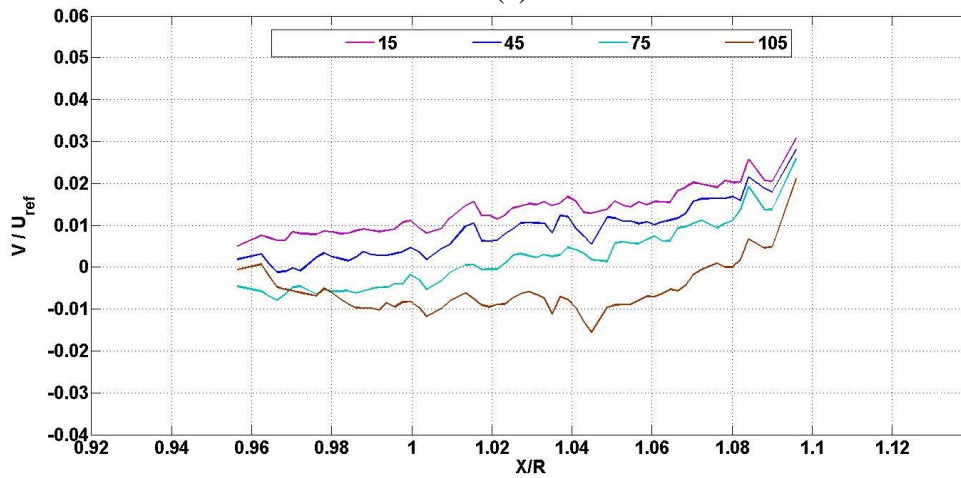
(b)

Figure 4-6: Radial profiles of normalized radial velocity for eight azimuth angles of blade at a)  $X=R$  b)

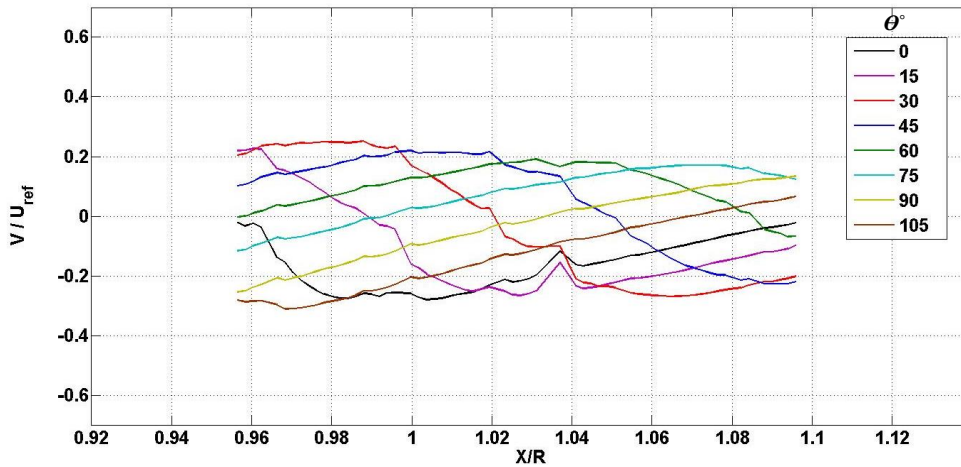
$X=2R$ .



(a)



(b)



(c)

Figure 4-7: Axial profiles of normalized radial velocity at a)  $r=0.45R$   
 b)  $r=0.85R$  c)  $r=1.05R$  for eight azimuth angles.

#### 4.1.2.3 Comparison with the MEXICO Experiment

In the following sub-sections, the velocity profiles from the present study are compared with those obtained from the MEXICO experiment. The MEXICO experiment performed at DNW German-Dutch wind tunnels (Snel et al., 2007; Schepers et al., 2012)) is the only to date large scale wind tunnel experimental campaign that aimed at using Particle Image Velocimetry (PIV) technique to characterize the rotating wake flow field of a 4.5 meters diameter wind turbine.

##### *Radial Profiles*

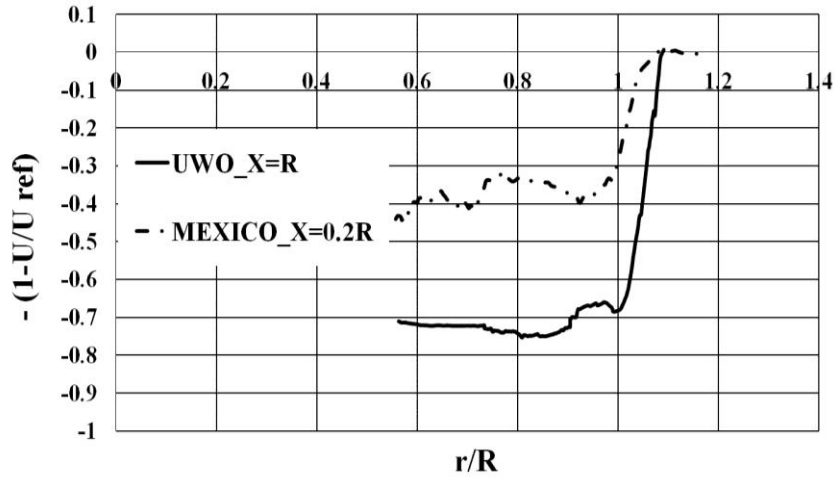
Figure 4-8 (a) shows the present radial profile of the axial velocity deficit for the blade azimuth angle of  $30^\circ$ ,  $X=R$  downstream of the turbine compared to the MEXICO experiment results. The tip speed ratio at which the MEXICO PIV measurements were performed is  $\lambda=6.67$  as opposed to  $\lambda=5.67$  for the present case. The MEXICO velocity field is determined for  $X=0.2R$  downstream of the turbine as opposed to  $X=R$  for the present case.

The comparison shows that the trend of the present profile (referred to as UWO hereafter) is similar to those of the MEXICO experiments; however, the magnitudes are different. The radial profiles of the axial velocity are influenced by the tip speed ratio at which the turbine operates (Vermeulen, 1978; Vermeer et al., 2003; Whale et al., 1996) as well as the axial location of the measurement (Sorenson and Shen, 2002). The axial velocity deficit, in the mid-section of the blade, increases as tip speed ratio increases, as observed by previous investigations (Vermeulen, 1978; Krogstad and Adaramola, 2012). This is because the wind turbine behaves more like a rotating disc for higher tip speed ratios and thus a larger decrease in axial velocity occurs at the central part of the rotor. Moreover, close to the rotor, for  $r/R < 3$  (near-wake region), the axial velocity deficit increases in the mid-section of the blade for larger downstream distances, as observed by previous investigations (Sørensen and Shen, 2002; Troldborg et al., 2007), mainly

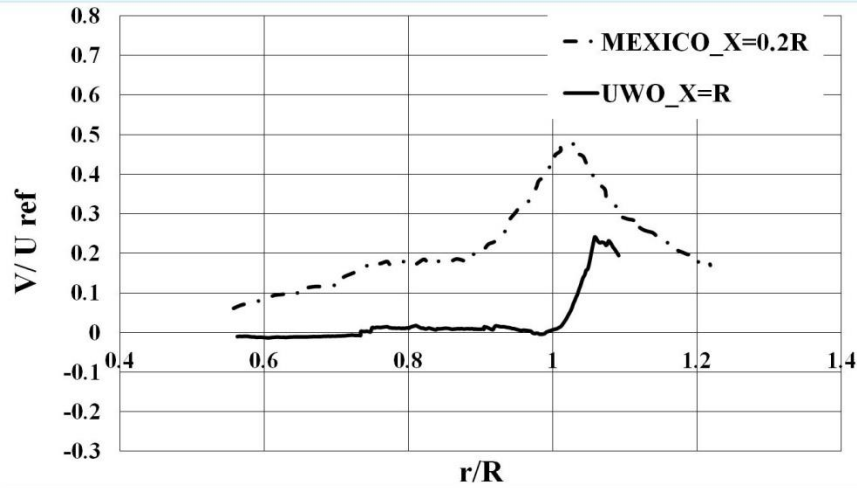
because the wake is at the stage of formation. Similar behavior has also been observed in axial profiles of axial velocity obtained from MEXICO experiments (see Figure 1-6). However, out of this region as the wake convects downstream, the axial velocity deficit decreases due to growth of the shear layer and turbulent mixing.

The difference between the present results and those obtained in the MEXICO experiments can be assessed using the above-mentioned effects. The difference in tip speed ratio is not the most important parameter to explain the differences since both turbines are operating at their optimal tip speed ratios and therefore similar behavior in flow field for both rotors is expected. On the other hand, since the MEXICO profile has been obtained in an axial location closer to rotor within the near-wake region, the axial velocity deficit is lower in magnitude as it is expected. It should be noticed that both results correspond to the same azimuth angle of blade (the  $0^\circ$  azimuth angle in the case of the MEXICO experiment is equivalent to  $30^\circ$  in present results).

The radial profiles of the radial velocity obtained from present measurements and the MEXICO experiments are compared in Figure 4-8 (b). Similar to the variations in the axial velocity, the profiles of the radial velocity show good agreement in trend; however, they do not match in magnitude. In particular, the radial velocity is larger in magnitude at  $X=0.2R$  downstream of the turbine in the MEXICO profile in comparison with the UWO experiment. A plausible reason can be that the axial location at which the MEXICO measurements are performed is closer to the rotor and thus the wake is still in the formation stage. In both radial profiles, the peaks represent the center of the tip vortices. Since the measurements were not at the same axial locations, one can expect to find the peaks at different radial positions due to wake expansion. This can clearly be observed in Figure 4-8 (b).



(a)



(b)

Figure 4-8: Comparison of the cross wind profiles of non-dimensional axial velocity deficits (a) and radial velocity (b) from the present experiments and the results obtained from the MEXICO experiment. The tip speed ratios, at which the experiments were performed, are 5.67 and 6.67 for UWO and MEXICO, respectively.

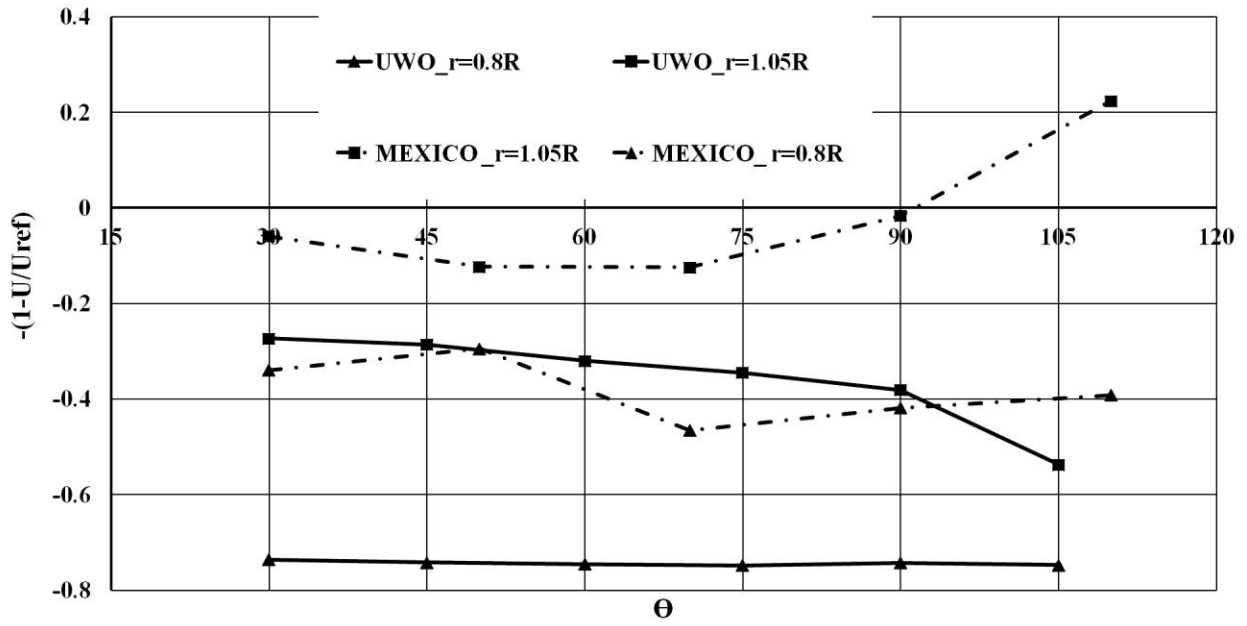


### *Azimuthal Profiles*

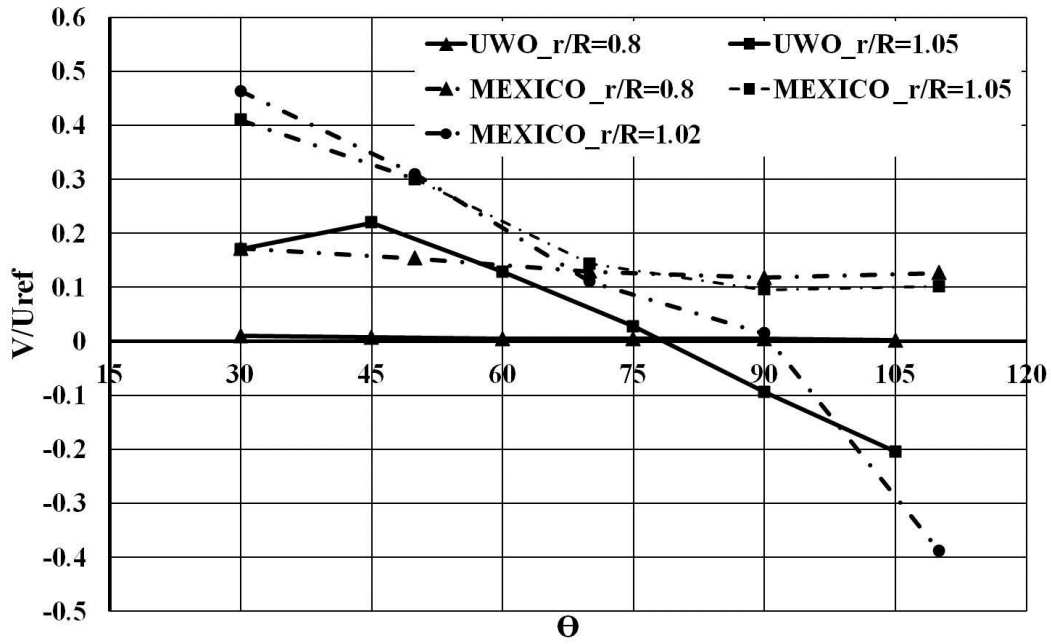
Figure 4-9 (a) presents the azimuthal profiles of axial velocity deficit obtained at  $X=R$  downstream of the rotor at  $r=0.8R$  and  $r=1.05R$ , reconstructed from the phase locked measurements at multiple phase angles. The profiles are compared with those provided by the MEXICO experiment obtained at  $X=0.2R$  for the same radial locations. In accordance with previous discussions, at  $r=1.05R$ , the axial velocity is dependent of phase angle for both experiments. For  $\theta < 90$ , the profiles show a good agreement in trend, even though they are different in magnitude. The reasons can be the difference in tip speed ratios and in particular the axial locations of the measurements. At  $r=0.8R$ , the UWO results indicate that the velocity is phase independent outside the tip region; however, for the MEXICO experiments, the profiles corresponding to  $r/R=0.8$  show small variation with respect to the phase angle. This can be resulted from the fact the MEXICO measurements are at  $X=0.2R$  downstream where the wake is still in the formation stage and thus more phase dependent.

The azimuthal profiles of radial velocity obtained at  $X=R$  are presented in Figure 4-9 (b) for two radial locations,  $r=0.8R$  and  $r=1.05R$ . The profiles are also compared with the profiled obtained in the MEXICO experiment at  $X=0.2R$  for three radial locations of  $r=0.8R$ ,  $r=1.02R$ ,  $r=1.05R$ . Note that the spanwise area associated with the tip vortex structure grows as the vortex convects downstream. In the case of the MEXICO experiment, where the measurements are at an axial location closer to the rotor, this area is thinner compared to the present (UWO) measurements. Therefore, the variations at  $r=1.02R$  are added for a more consistent comparison of the behavior of the radial velocity in the tip region. It can be seen that similar to the profiles of axial velocity, the profiles of radial velocity are highly variable with respect to the phase angle in the tip region at  $r=1.02R$ , while for  $r=0.8R$ , profiles obtained from both experiments are phase independent.

The profiles at  $r=1.05R$  for UWO experiment and at  $r=1.02R$  for MEXICO experiment (the radial positions corresponding to the location of the dominant vortical structure) match well in trend, although they are different in magnitude due to the aforementioned reasons.



(a)



(b)

Figure 4-9: Comparison of the circumferential profiles of non-dimensional (a) axial velocity deficits and (b) radial velocity between the present profiles corresponding to  $X=R$  and the profiles obtained from MEXICO experiment corresponding to  $X=0.2R$ . The tip speed ratios, at which the simulations were performed, are 5.67 and 6.67 for UWO and MEXICO, respectively.

### 4.1.3 Quantification of the Turbulent Flow Field in the Near-wake Region

To quantify the turbulent flow field for each experimental run corresponding to one phase angle, the time series of fluctuating components of velocity were extracted at each grid point from the sequence of corrected instantaneous velocity fields. The turbulence characteristics presented in this section are time averaged for each specific azimuth angle of the blade. Note that in each time series, all points at which no numerical data were available due to inadequate light intensity were excluded from the computation of turbulence characteristics.

#### 4.1.3.1 Reynolds Stresses and Turbulent Kinetic Energy

The relation between the mean flow and turbulence can be expressed through the Reynolds-averaged Navier-Stokes equation (Pope, 2000):

$$\frac{\partial \overline{U}_i}{\partial t} + \overline{U}_j \cdot \frac{\partial \overline{U}_i}{\partial x_j} = -\frac{1}{\rho} \frac{\partial}{\partial x_j} [p \delta_{ij} - 2\mu S_{ij} + \rho \overline{u'_i u'_j}] \quad 3.1$$

The above equation is adapted from Tom (2010) who presented the original equation from Pope (2000) in a slightly different form. The right-hand side of the equation represents the mechanisms of momentum transfer, which constitutes mean pressure field, viscous stress and fluctuating velocity field (Reynolds stress), respectively (Pope 2000). According to Eq. 3.1, the mean momentum is transported by the pressure gradient, viscosity and turbulent fluctuations. The Reynolds stresses,  $\overline{u'_i u'_j}$ , emerge from the Navier-Stokes equations via Reynolds decomposition and taking the time average, in the process known as Reynolds averaging. Reynolds stresses quantify the interaction between the mean and turbulent components of the flow.

Herein, the results acquired for the Reynolds stresses, including root mean square of axial and radial velocity,  $\sqrt{u'^2}$  and  $\sqrt{v'^2}$ , respectively, and Reynolds shear stress,  $\overline{u'v'}$ , are presented.

Figure 4-10 shows contour plots of normalized  $U_{rms}$  (i.e. axial component of Reynolds stress) for  $0.96 < X/R < 1.08$  downstream of the rotor for eight different azimuth angles of the blade. In the shear layer zone, for  $0.96 < X/R < 1.08$  the turbulence intensity is larger than 10%. This region is associated with the tip vortex, and thus the  $U_{rms}$  values are highly dependent on the azimuth (phase) angle. As it can be seen in Figure 4-10, the area associated with high  $U_{rms}$  values moves gradually in the axial direction when the azimuth angle increases. In the blade frame of reference, this can be interpreted as a signature of the helical path of the tip vortices generated from the blades (see Figure 1-2 (b)). Note that for  $\Theta \geq 90^\circ$ , the area with high Reynolds stress is associated to the tip vortex generated from the next blade of the turbine. This is best illustrated in the contour plot for  $\Theta = 105^\circ$  (see Figure 4-10 (h)).

Figure 4-11 (a) displays the radial profiles of normalized  $U_{rms}$  at  $X=R$  (see also Figure 4-10) for different azimuth angles. As expected, the turbulence intensity varies with respect to the azimuth or phase angle at  $r/R > 0.9$ . The highest value of  $U_{rms}$ , which is 0.43 at  $r \sim 1.05R$ , occurs at the azimuth angle of 15 at which the core of the tip vortex is exactly located at  $X=R$  (see Figure 4-10 (b)). The  $U_{rms}$  value decreases for higher azimuth angles, since the vortex moves both in axial and circumferential directions (while moving downstream, it also moves out of the measurement plane) (see Figure 4-10). Note that the discontinuity in the profiles for  $0.55 < r/R < 0.75$ , which is most prominent at  $\Theta = 105^\circ$ , is because of the patching process. The radial profiles of turbulence intensity are plotted for  $0.4 < r/R < 0.9$  in Figure 4-11 (b). Similar to the behavior of the mean component of velocity, the turbulence intensity is almost independent of azimuth angle for  $0.6 < r/R < 0.9$ . For  $r/R < 0.6$  the  $U_{rms}$  changes with respect to phase due to the root vortices.

Although  $U_{\text{rms}}$  increases for  $r/R < 0.6$ , it is still smaller compared to the turbulence intensity resulting from the tip vortex.

Figure 4-11 (c) shows the radial profiles of normalized  $U_{\text{rms}}$  at  $X=2R$  downstream of the turbine. In accordance with the mean flow field, the results show that at  $X=2R$ , the turbulence intensity is independent of azimuth phase angle. The magnitude of  $U_{\text{rms}}$  reduces at larger distances from the rotor (Vermeer, 2003). Nevertheless, higher values of turbulence intensity are found in the shear layer,  $r/R > 0.75$ , with a maximum value of 0.18 at  $r \sim 1.05R$ . It can be inferred that the location of the maximum  $U_{\text{rms}}$  remains at almost the same radial distance from the center of the rotor from  $X=R$  to  $X=2R$ .

Comparison between Figure 4-11 (a) and Figure 4-11 (c) indicates that the shear layer shifts from  $r/R > 0.9$  at  $X=R$  to  $r/R > 0.75$  at  $X=2R$  downstream, while the turbulence intensity is still larger than 10% within the layer. This confirms the development of the shear layer in the axial direction resulting in momentum transport towards the center of the rotor. It can be concluded that as the flow convects downstream in the wake, the turbulence acts as the mixing mechanism, transporting the momentum toward the centre of the wake while the turbulence intensity decreases.

Figure 4-12 displays contour plots of normalized  $U_{\text{rms}}$ , at  $1.96 < X/R < 2.08$  downstream of the turbine for three different azimuth angles of the blade. Similar to the radial profile, it can be seen that at  $X=2.02R$ ,  $U_{\text{rms}}$  is phase independent. The turbulence intensity acquires its highest value at  $r/R > 0.75$ , which is the region dominated by the shear layer. A comparison between Figure 4-12 and Figure 4-10 clearly reveals that the shear layer, which corresponds to  $r/R > 0.9$  for  $0.96 < X/R < 1.08$  and to  $r/R > 0.75$  for  $1.96 < X/R < 2.08$ , grows downstream of the rotor.

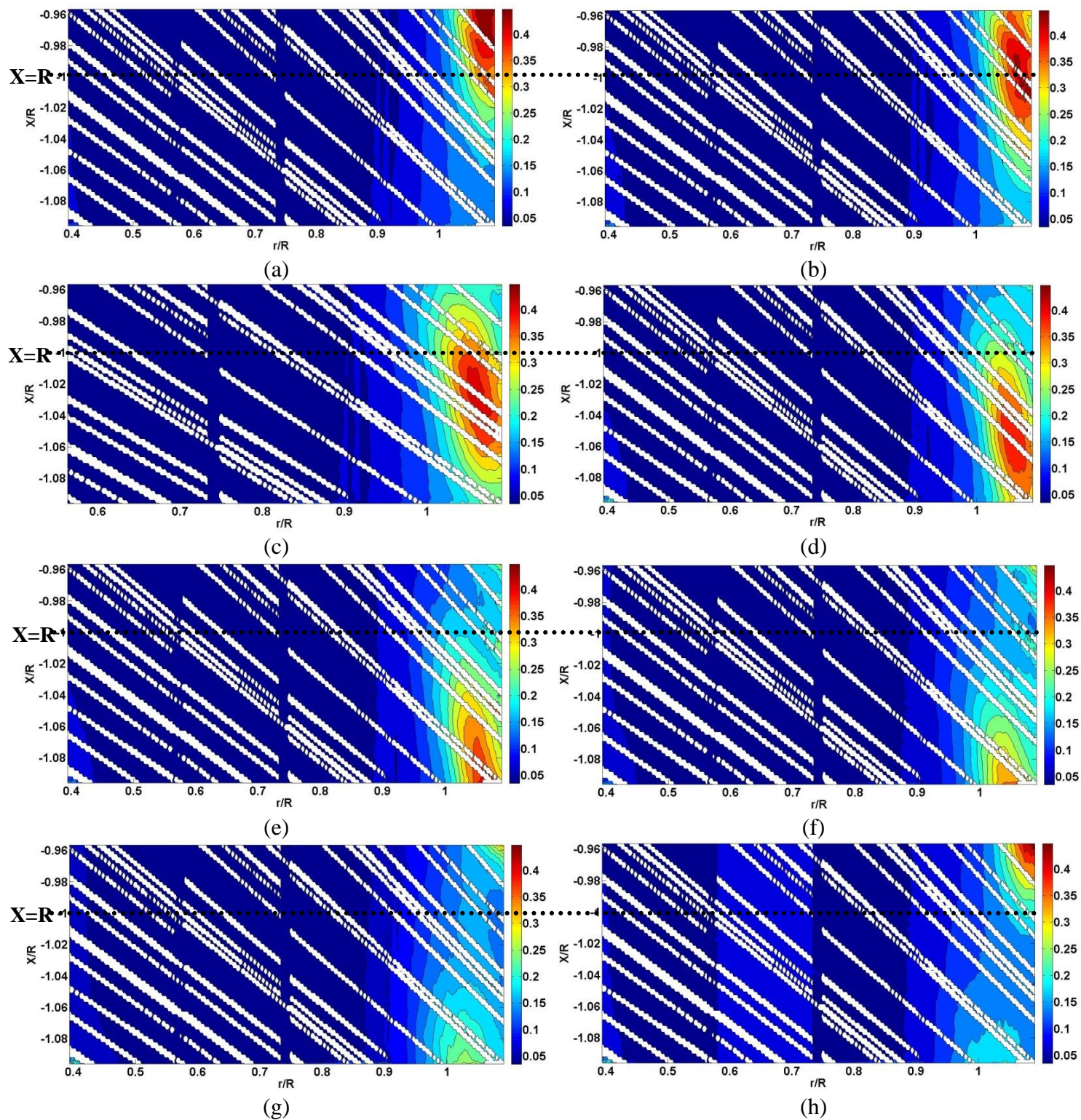
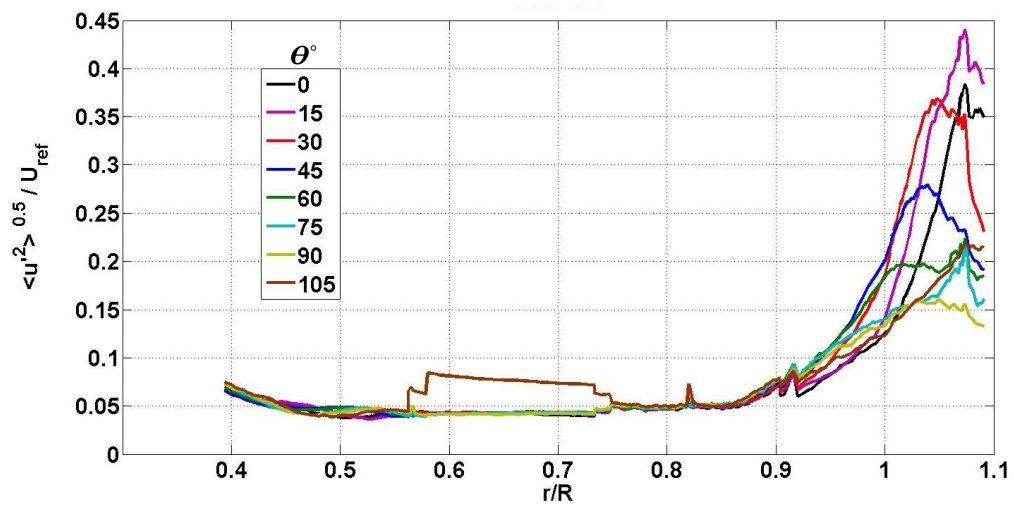
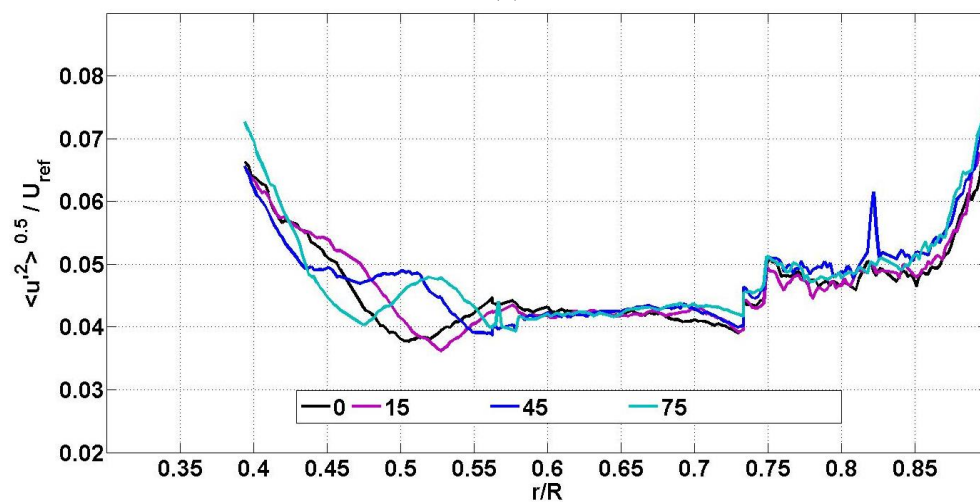


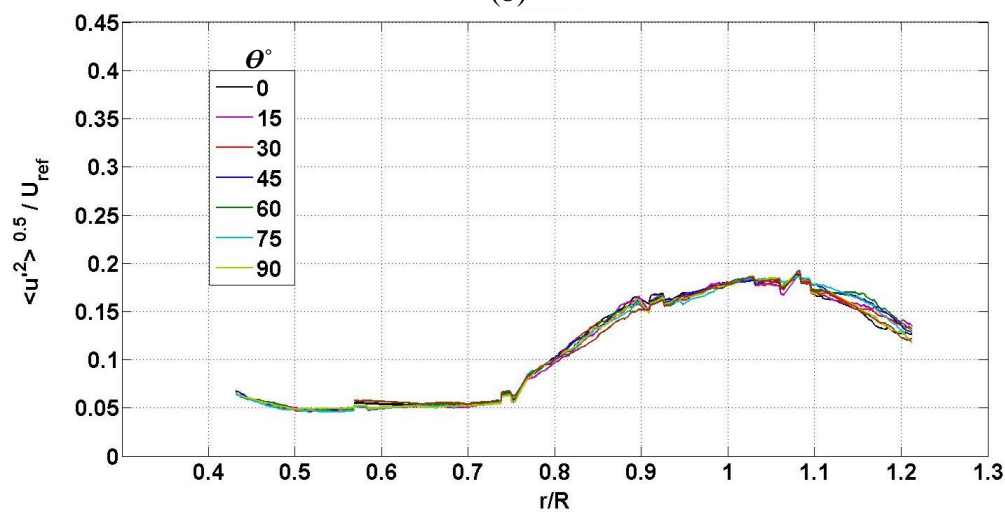
Figure 4-10: Contour plots of normalized  $U_{rms}$  at  $0.96 < X/R < 1.08$  downstream of the turbine for eight different azimuth angles of the blade: a)  $0^\circ$ , b)  $15^\circ$ , c)  $30^\circ$ , d)  $45^\circ$ , e)  $60^\circ$ , f)  $75^\circ$ , g)  $90^\circ$ , h)  $105^\circ$ .



(a)



(b)



(c)

Figure 4-11: Radial profiles of normalized  $U_{rms}$  at a)  $X=R$  b)  $X=R$  for  $0.4 < r/R < 0.9$  c)  $X=2R$ .



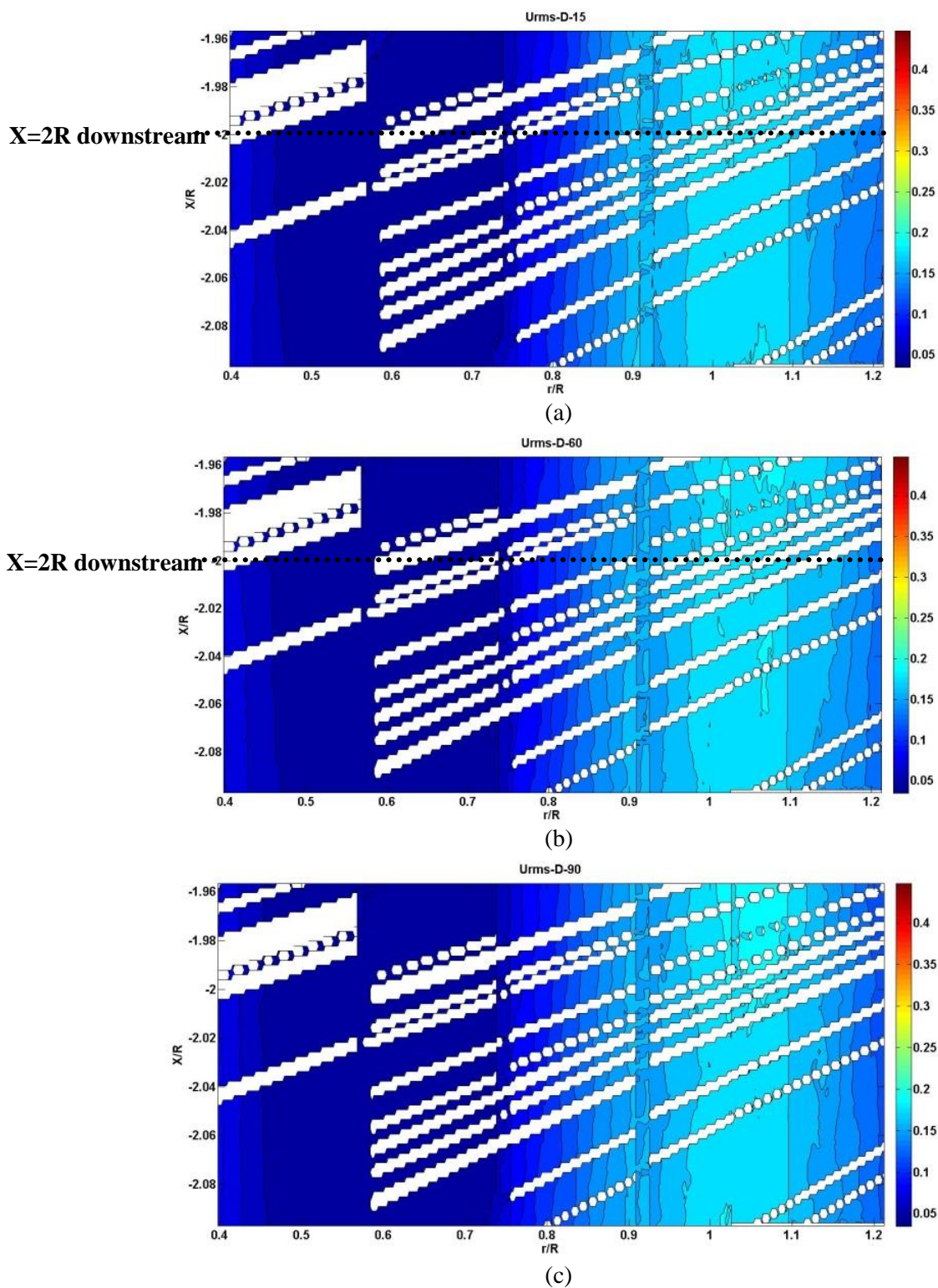


Figure 4-12: Contours of normalized  $U_{rms}$  at  $1.96 < X/R < 2.08$  downstream the turbine for: a)  $15^\circ$ , b)  $60^\circ$ , c)  $90^\circ$ .

Figure 4-13 displays the contour plots of  $V_{rms}$  at  $0.96 < X/R < 1.08$  downstream. The results are presented for three azimuth angles of the blade:  $15^\circ$ ,  $45^\circ$ ,  $75^\circ$ , in order to assess the variation the  $V_{rms}$  with respect to phase. It can be seen that similar to the variation of  $U_{rms}$ , the radial turbulence intensity reaches a maximum in the tip region ( $r/R > 0.9$ ). The axial movement of the region with high  $V_{rms}$  is consistent with the helical trajectory of the tip vortex (as it was discussed in the case of  $U_{rms}$ ), which also explains the dependency of the  $V_{rms}$  on the phase angle. Moreover, similar to contour plots of  $U_{rms}$ , the high turbulent intensity region at  $r/R > 0.9$  can be considered as the trace of the shear layer.

The radial profiles of  $V_{rms}$  are presented in Figure 4-14 for eight different azimuth angles of the blade at  $X=R$  downstream of the rotor. It can be observed that the peak of  $V_{rms}$  occurs at  $30^\circ$  with a magnitude of 0.37 at  $r \sim 1.03R$ . This peak corresponds with the high radial velocity at the same azimuth angle (see Figure 4-6 (a)). As the azimuth angle increase for  $30 < \Theta < 90$  the turbulence intensity components decrease. The values increase for  $\Theta \geq 90^\circ$ , due to the tip vortex generated from the next blade. Moreover, similar to the profiles of  $U_{rms}$ , for  $r/R > 0.9$ ,  $V_{rms}$  is phase dependent due to the passage of the tip vortex. For  $0.6 < r/R < 0.9$  the results are independent of the azimuth angle. For  $r/R < 0.6$ ,  $V_{rms}$  varies with respect to the azimuth angle due to the root vortex.

The contour plots of Reynolds shear stresses,  $\overline{u'v'}$ , are presented in Figure 4-15 for three azimuth angles of the blade:  $15^\circ$ ,  $45^\circ$ ,  $75^\circ$ , at  $0.96 < X/R < 1.08$  downstream of the rotor. Similar to the contour maps of  $U_{rms}$  and  $V_{rms}$ , the highest values of Reynolds shear stress occurs at the tip region indicating high shear due to turbulence in this region. Based on the contour plots of normal and shear components of Reynolds stress, one can infer that the highest turbulence generation occurs at  $r/R > 0.9$ , due to tip vortices and large velocity gradients. In the mid section of the blade, the Reynolds shear stress becomes almost zero, while it tends to increase in

magnitude for  $r/R < 0.6$ , with the opposite sign. The change in sign is resulted from the change in direction of velocities, mainly the radial component and the opposite sense of rotation of the root vortex.

Figure 4-16 displays the radial profiles of  $\overline{u'v'}$  at  $X=R$  downstream of the turbine for eight different azimuth angles. It can be seen that similar to the profiles of  $U_{\text{rms}}$ , the maximum values occur for the azimuth angle of  $15^\circ$  at  $r \sim 1.05R$ . Similar to  $U_{\text{rms}}$ , this maximum is associated to the tip vortex which for  $\Theta = 15^\circ$  is located at  $X=R$ . The values reduce as the phase increases. For  $\Theta \geq 90^\circ$  the  $\overline{u'v'}$  increases due to the effect of the tip vortex generated from the next blade. In accordance with the profiles of  $U_{\text{rms}}$  and  $V_{\text{rms}}$ ,  $\overline{u'v'}$  is phase dependent for  $r/R > 0.9$  and  $r/R < 0.6$  due to the passage of tip and root vortices, respectively. However, it is phase independent in the region which is unaffected by the two vortices ( $0.6 < r/R < 0.9$ ).

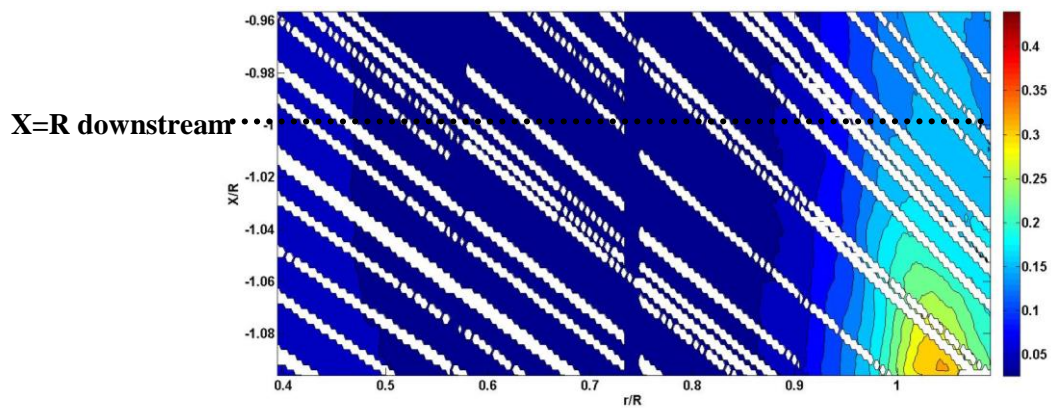
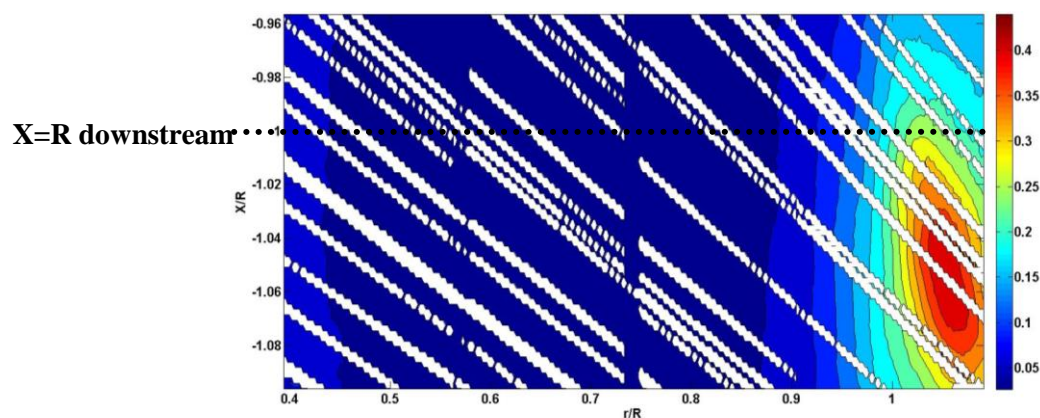
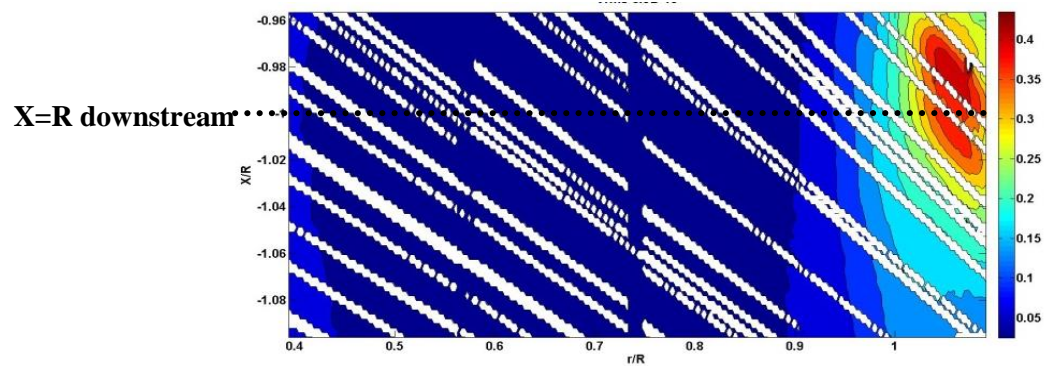


Figure 4-13: Contour plots of normalized  $V_{rms}$  for three azimuth angles of the blade at  $0.96 < X/R < 1.08$  downstream of the turbine: a)  $15^\circ$ , b)  $45^\circ$ , c)  $75^\circ$ .

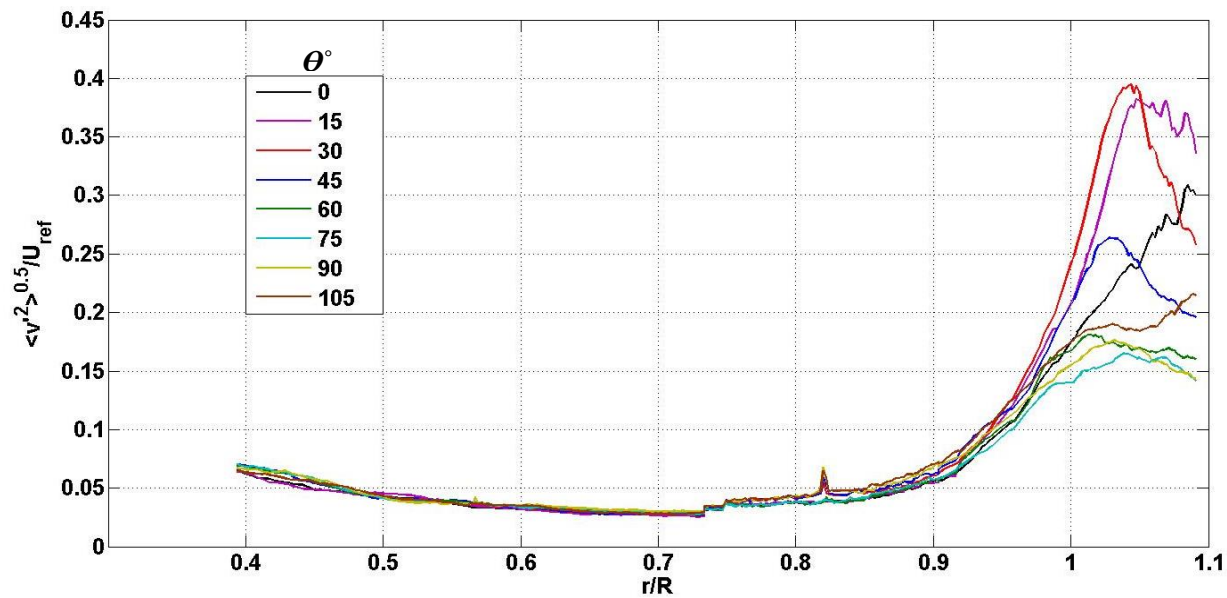


Figure 4-14: Radial Profiles of normalized  $V_{rms}$  at  $X=R$  downstream the turbine for eight different azimuth angles of the blade

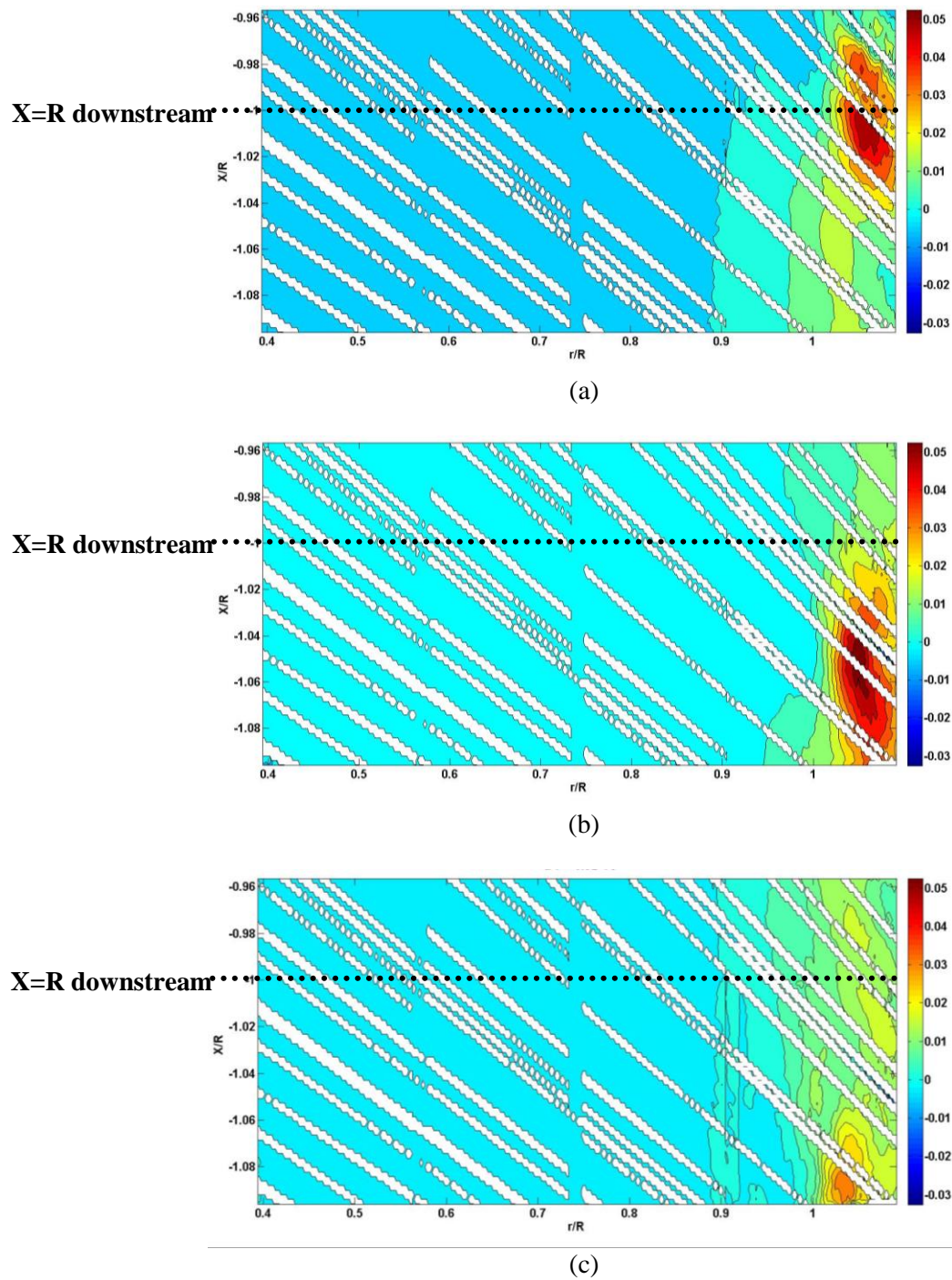


Figure 4-15: Contour plots of normalized  $\overline{u'v'}$  for three azimuth angles of the blade at

$0.96 < X/R < 1.08$  downstream of the turbine: a)  $15^\circ$ , b)  $45^\circ$ , c)  $75^\circ$ .

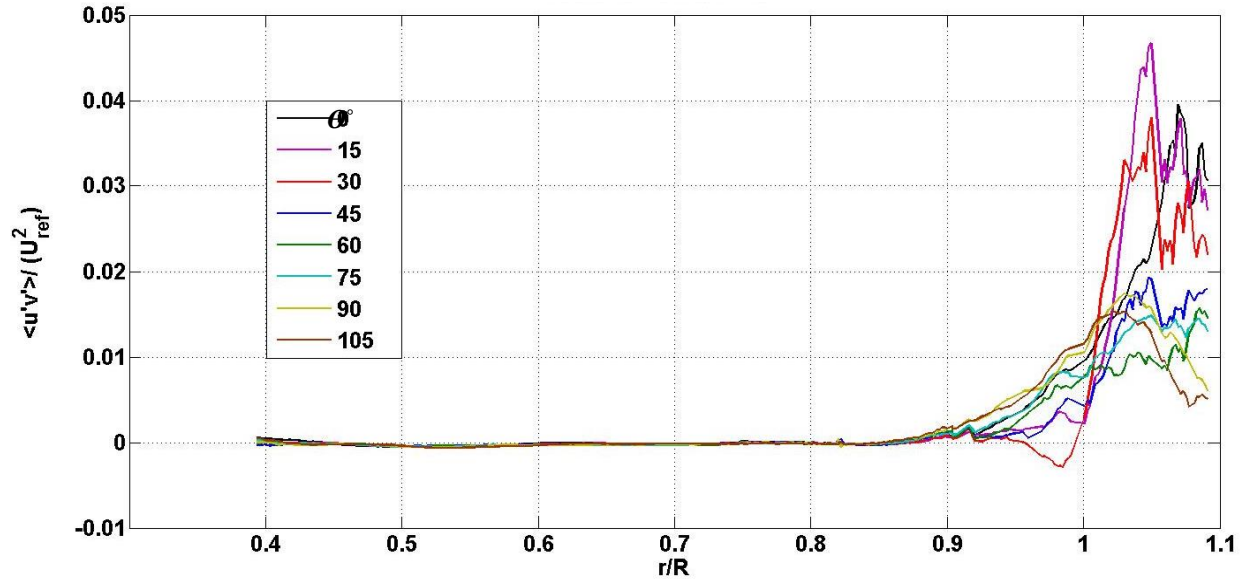


Figure 4-16: Radial Profile of normalized  $\overline{u'v'}$  at X=R downstream of the turbine for eight different azimuth angles of the blade

The radial profiles of  $V_{rms}$  and  $\overline{u'v'}$  at X=2R downstream the turbine as well as the axial profiles of the corresponding parameters are not presented due to the similarity of the behavior between these profiles and those shown for  $U_{rms}$ .

Physically, the turbulent kinetic energy is defined as the root mean square of fluctuating components of velocity. TKE is produced by large scale eddies representing the forcing of the flow with large time scales, or in other words by fluid shear, friction and buoyancy. At smaller time scales, (Kolmogorov scale is the small scale which corresponds with higher frequencies), TKE is dissipated by viscous forces. The energy is transported by the medium scale eddies. The process of production, transport and dissipation can be described by the following equation (Pop, 2000):

$$\underbrace{\frac{\partial k}{\partial t}}_{\text{Local derivative}} + \underbrace{\bar{u}_j \frac{\partial k}{\partial x_j}}_{\text{Advection}} = - \underbrace{\frac{1}{\rho_o} \frac{\partial \overline{u'_i p'}}{\partial x_i}}_{\text{Pressure diffusion}} - \underbrace{\frac{\partial \overline{k u_i}}{\partial x_j}}_{\substack{\text{Turbulent} \\ \text{transport} \\ \mathcal{T}}} + \underbrace{\nu \frac{\partial^2 k}{\partial x_j^2}}_{\substack{\text{Molecular} \\ \text{viscous} \\ \text{transport}}} - \underbrace{\overline{u'_i u'_j} \frac{\partial \bar{u}_i}{\partial x_j}}_{\text{Production } \mathcal{P}} - \underbrace{\nu \frac{\partial \overline{u'_i} \partial \overline{u'_i}}{\partial x_j \partial x_j}}_{\substack{\text{Dissipation} \\ \epsilon_k}} - \underbrace{\frac{g}{\rho_o} \overline{\rho' u'_i} \delta_{i3}}_{\substack{\text{Buoyancy flux} \\ b}} \quad 3.2$$

where  $k$  represents the TKE, and  $u_i'$  represents the fluctuating components of velocity. According to Eq. 3.2, normal and shear components of Reynolds stress, are the main sources of the production of the TKE. In the present experiments, the results corresponding to the Reynolds Stresses, presented in the previous sub-section, indicate that the turbulence production occurs mostly in the tip region of the blade ( $r/R > 0.9$ ) within the near-wake region, in particular for  $X < R$ . In this section, the contour plots, and the axial and radial profiles of TKE are also presented. The turbulent kinetic energy is approximated using ,  $TKE = \frac{1}{2}(u'^2 + 2v'^2)$ , where  $u'$  and  $v'$  are the streamwise and radial components of the fluctuating velocity. Note that the circumferential component of turbulent velocity is assumed to be equal to the radial component of turbulent velocity.

Figure 4-17 presents the contour plots of normalized Turbulent Kinetic Energy (TKE). The results correspond to  $0.96 < X/R < 1.08$  downstream of the turbine for three azimuth angles of  $15^\circ$ ,  $45^\circ$ ,  $75^\circ$ . Similar to the contour plots shown for previous turbulent components, it can be clearly observed that the highest values of TKE occurs at  $r/R > 0.9$ . One can assume this region as general location of the shear layer characterized by the large velocity gradients resulting from the tip vortex.

Radial profiles of (TKE) are displayed in Figure 4-18. The maximum value of TKE corresponds to the azimuth angle of  $15^\circ$  at  $r \sim 1.08R$  with a magnitude of 0.26. The maximum clearly corresponds with the existence of the vortex structure at  $X=R$ . For  $\Theta > 15^\circ$ , TKE decreases, as the vortex is convected further downstream from the  $X=R$  axial location, and goes out of plane (the



helical vortex tube.). The values increase for  $\Theta \geq 90^\circ$  due to the tip vortex generated from the next blade. Also, in accordance with previous results, the TKE is highly dependent on the phase angle in the tip region,  $r/R > 0.9$ , while it becomes phase independent in  $0.6 < r/R < 0.9$ .

Figure 4-19 (a) displays the axial profiles of normalized TKE at  $r=1.05R$  for eight different azimuth angles. The peak of each profile represents the position of the tip vortex. Hence, the axial movement of the peaks clearly shows the helical path of the tip vortex. Note that the peak corresponding to  $90^\circ$  and  $105^\circ$  represents the vortex produced by the next the blade. The patterns of these profiles are similar to those shown in Figure 3-9 (b) representing the helix trajectory. The similarity between the patterns confirms the existence of the vortex and its helical trajectory in this region. Figure 4-19 (b) presents the axial profile of normalized TKE at  $r=0.85R$  for four different azimuth angles. In accordance with the flow parameters discussed previously, the TKE is independent of azimuth angle at this radial position. For  $X > 1.09R$  TKE increases due to expansion of the shear zone as the as the flow is convected downstream in the wake.

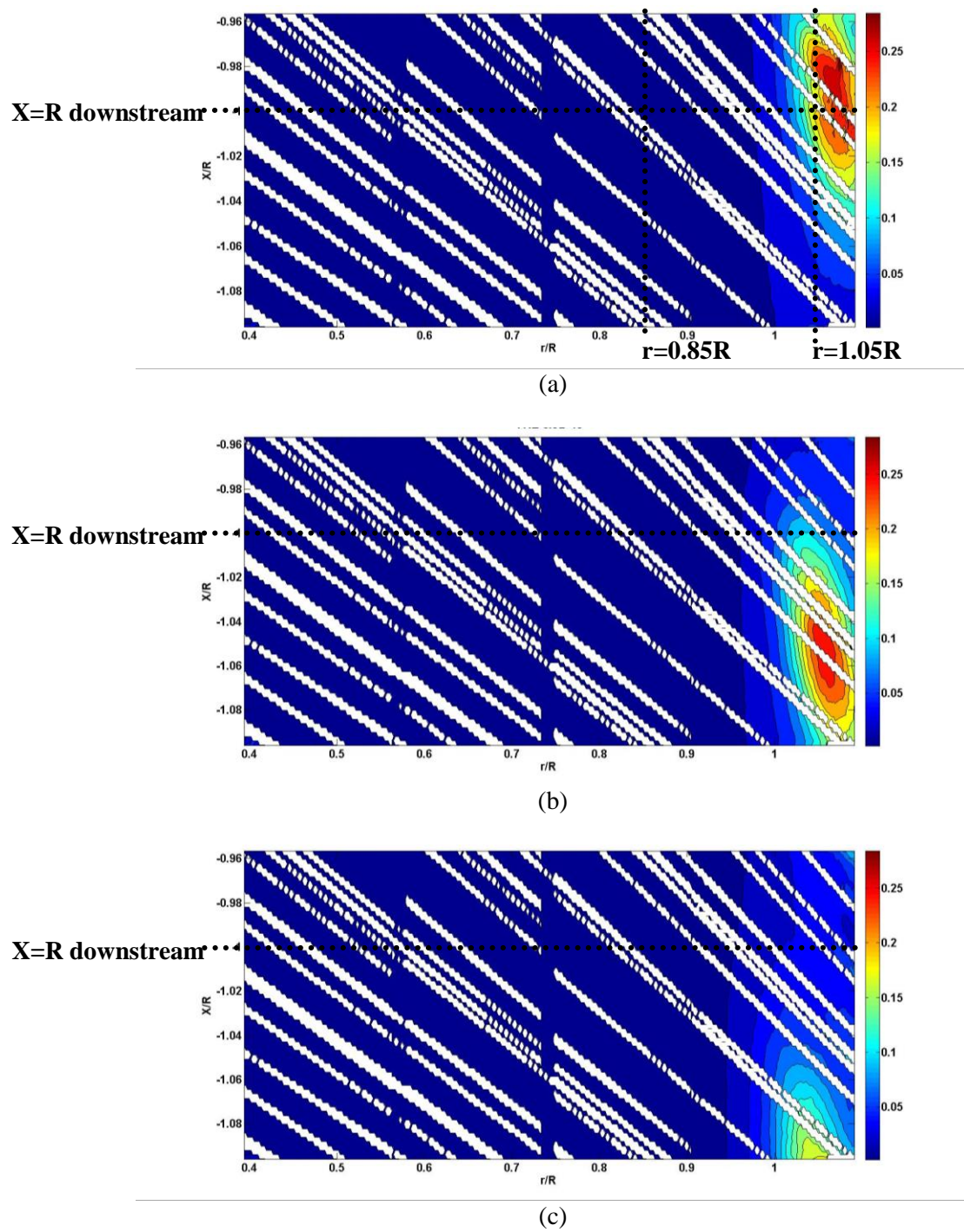


Figure 4-17: Contour plots of normalized TKE for three azimuth angles of the blade at  $0.96 < X/R < 1.08$  downstream the turbine: a)  $15^\circ$ , b)  $45^\circ$ , c)  $75^\circ$ .

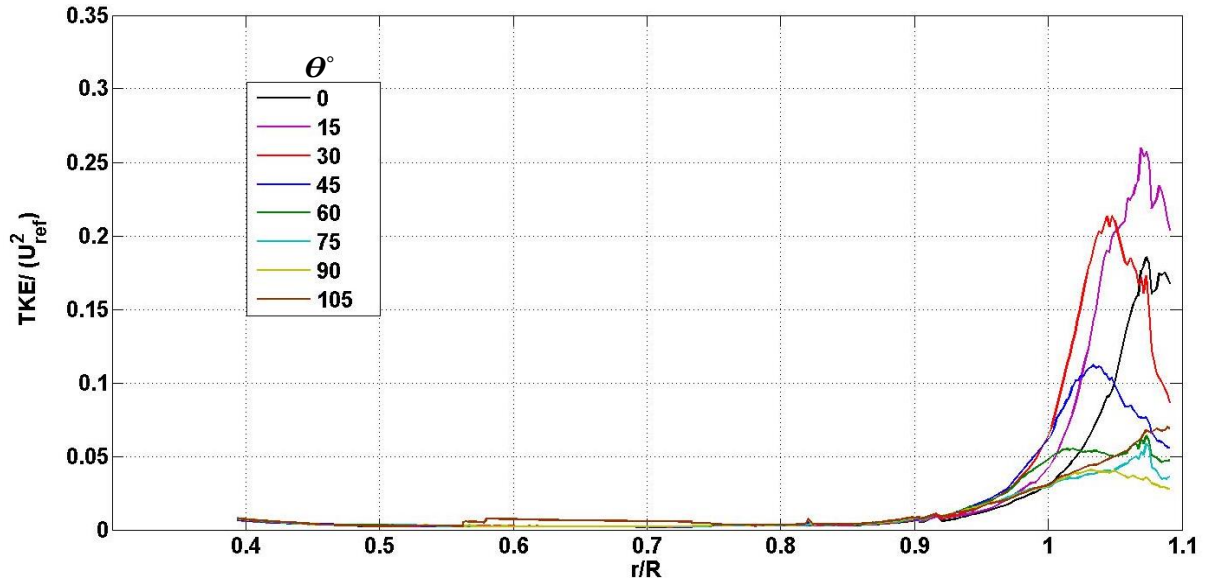


Figure 4-18: Radial profiles of normalized TKE at  $X=R$  downstream for eight different azimuth angles of blade.

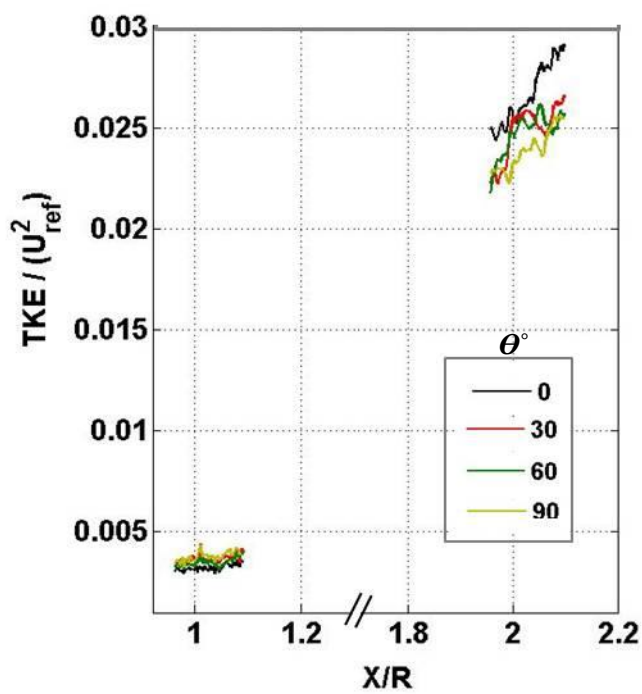
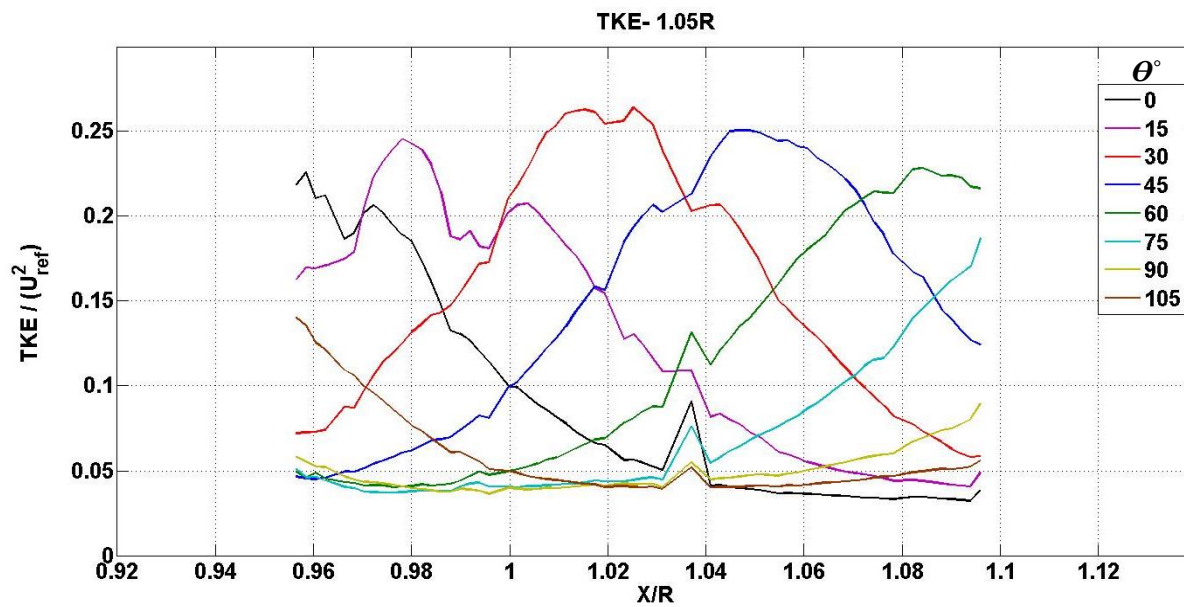


Figure 4-19: Axial profiles of normalized TKE at a)  $r=1.05R$ , b)  $r=0.85R$ .

## 4.2 Comparison with the Blade Element Momentum (BEM) method

The BEM method is a popular aerodynamic modeling approach for wind turbines. The assumptions employed by this method were described in the first chapter of this thesis, (see 1.3.1.1). In this section, an attempt is made to compare the PIV results with the results obtained using the BEM method in order to assess the capability and limitations of the BEM method in predicting axial velocity profiles at the location of rotor disc.

As mentioned earlier, in this method the induced velocities and aerodynamic forces are determined through an iterative solution for  $a$  (the axial induction factor) and  $a'$  (the angular induction factor) by employing the conservation equations for axial and angular momentum, and 2D airfoil section data (See Figure 1-7). The iterative solution is performed for each element of the blade; therefore, the aerodynamic forces and the power output are computed by integrating over the blade span. Moreover, using the axial induction factor for each element of the blade, the radial profiles of axial velocity can be obtained using the relation  $a=(1-U_d/U_\infty)$ , where  $U_d$  is the axial velocity at the rotor disk.

Refan and Hangan (2012) employed the BEM approach to quantify the induction factors and consequently the power curve of the wind turbine studied in the present experiments (see also Refan (2009)). A series of corrections, including tip loss, stall delay and thrust coefficient corrections, were applied to obtain a more accurate prediction of the power curve.

The tip loss correction is meant to account for the reduction in lift and power generation close to the tip of a blade. This reduction is associated to the difference in the pressure on the suction side of the blade and pressure side of the blade causing the air to flow around the tip from the pressure side to the suction side. To account for this effect, a correction factor developed by Prandtl (Manwell et al., 2002) was added to the classic BEM approach. This factor adds the

reduction in the forces at each radial position on the blade, resulting from the tip loss at the end of the blade. The factor varies between 0 and 1, depending on the distance from the tip (More details can be found in Refan (2009)). The correction factor is computed using the following relation:

$$F = \left(\frac{2}{\pi}\right) \cos^{-1} \left[ \exp \left( - \left\{ \frac{(B/2)[1 - (r/R)]}{(r/R) \sin \phi} \right\} \right) \right] \quad 3.3$$

where  $F$  is the tip loss correction factor,  $B$  is number of blades,  $r$  represents the radial position of each element of the blade and  $\phi$  is the angle of relative wind speed. The tip loss correction factor affects the forces derived from the momentum theory; however it does not change the equations obtained from blade element theory. Therefore, the tip loss correction is added to the previous blade element theory equations (see Eq. 1.3) to obtain the new momentum theory equations.

According to Himmelskamp (1945), since the angle of attack of a rotating blade is smaller compared to a stationary one, there is a reduction in the adverse pressure gradient on a rotating blade. This phenomenon is called stall-delay, and should be taken into account to correct the BEM equations. The correction method is based on the empirical relationship between two dimensional and three dimensional lift proposed by Snel et al. (1993) (See Refan (2009) for more details). Following equation is used to determine the stall-delay correction (Burton et al., 2001).

$$C_{l_{3D}} = C_{l_{2D}} + 3 \left(\frac{c}{r}\right)^2 \Delta C_l \quad 3.4$$

Where  $C_{l_{3D}}$  and  $C_{l_{2D}}$  represent the three- and two-dimensional lift, respectively,  $c$  is the chord length at each radial position,  $\Delta C_l$  is the difference between the actual two-dimensional  $C_l - \alpha$  curve and the curve resulting from extension of the linear part of the static (two-dimensional) curve beyond the stall.

The next correction applied to the calculation of axial induction factor, is the thrust coefficient correction. The thrust is determined using the equation  $C_T=4a(1-a)$  obtained from the linear momentum theory. However, the equation can only be employed for  $a < 0.4$  (Hansen, 2008). In other words, for the higher induction factors, where the state of the wake is turbulent, the thrust predicted by the momentum theory is no longer valid. Thrust coefficient and axial induction factor are related using different empirical equations. Eq. 3.5 shows an empirical relationships developed by Glauert (1935) which is valid for  $C_T > 0.96$  or equivalently, for  $a > 0.4$  (See Refan (2009) for more details).

$$a = \left(\frac{1}{F}\right) \left[ 0.143 + \sqrt{0.0203 - 0.6427(0.889 - C_T)} \right] \quad 3.5$$

Figure 4-20 presents the radial profile of normalized axial velocity deficit obtained from the PIV measurements at  $X=0.96R$  downstream of the turbine. The profile is circumferentially averaged. The result is also compared with the profiles obtained based on BEM modeling using the program developed by Refan (2009). In the BEM modeling, the flow is assumed to be axisymmetric; hence, the results are considered to be phase independent. It should be noted that the BEM approach provides the axial induction factor at the rotor disk; therefore, the profiles of axial velocity are also at the rotor location. Different corrections are taken into account to assess the validity of the results of the BEM method. The profiles shown in Figure 4-20 correspond to the cases with all corrections, without tip loss correction, without stall-delay correction and without both tip loss and stall-delay corrections. Note that all the profiles are acquired at the same tip speed ratio as that of the present experiments ( $\lambda=5.67$ ).

As indicated by Figure 4-20, the radial profiles obtained from BEM modeling show good agreement in trend with the PIV result, particularly for  $r/R < 0.75$ . The difference in magnitude can be attributed to the difference in the axial locations at which the results are obtained. As it is

expected, the profiles, obtained using BEM method, are lower in magnitude compared to the profile acquired from PIV measurements, since the axial location where the BEM results are obtained is closer to the rotor. This development of axial velocity profiles close to the rotor (at  $r/R < 3$ ) has been also observed by previous investigation (Sørensen and Shen, 2002; Troldborg et al., 2007) and also in the comparison between present results and those obtained by MEXICO experiments. Moreover, for  $r/R < 0.75$ , the profiles obtained from the BEM modeling show that the corrections do not influence the profiles. However, for  $r/R > 0.75$ , two different behaviors can be observed in the profiles acquired from BEM modeling.

Figure 4-20 indicates that the stall correction has no effect on the behavior of the profiles, because the angle of attack, at each section of the blade, is smaller than the angle of stall due to the low wind speed. In other words, for the case of low wind speed, all the elements are in the fully attached flow regime. In this regime, the tip loss correction is the main correction factor influencing the profiles. For  $r/R > 0.75$ , the profiles corresponding to the cases without tip loss correction do not match with the PIV measurements in trend and in magnitude. In the profile obtained from PIV measurements,  $r/R > 0.85$  is the region with high velocity gradient associated with the shear layer. It is expected that this region becomes smaller by getting closer to the rotor, since the shear layer grows downstream of the rotor, in the wake. In other words it is expected that the high-velocity-gradient region in the profile corresponding to the location of the rotor disk shifts toward the tip ( $r=R$ ). Therefore, for  $r/R > 0.75$ , the case without tip loss correction does not behave as it is expected, since the axial velocity changes at  $r \sim 0.75R$  with a positive slope. One can infer that, for  $r/R > 0.75$ , the profiles with the tip-loss correction match well in trend with the experimental results, regardless of stall-delay correction, due to the aforementioned reason.



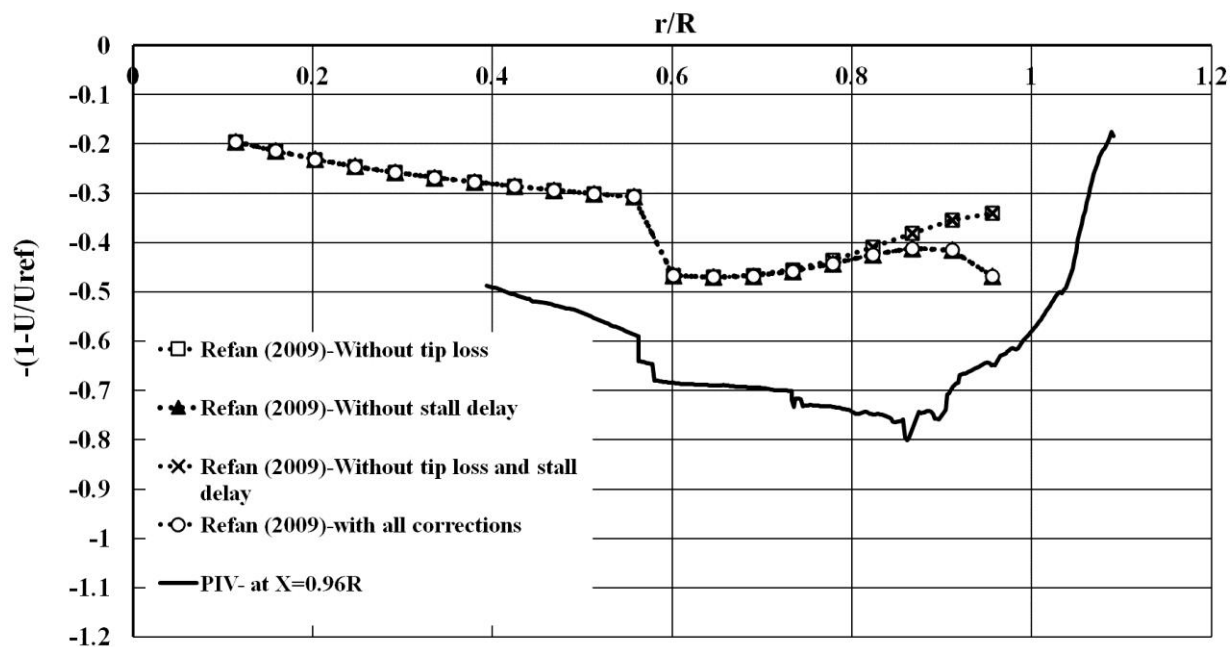


Figure 4-20: Radial profiles of normalized axial velocity acquired from PIV measurements and BEM

Modeling. The profiles are obtained at the same tip speed ratio. The profiles acquired from BEM

modeling are generated at the location of the rotor disk.

### 4.3 Scaling effects

In wind tunnel measurements, three different types of scaling are taken into account, including geometric scaling, kinematic scaling and dynamic scaling. These scaling ratios need be equated between the wind tunnel measurements and the full-scale phenomena to satisfy the similarity conditions. Having considered this, one can extrapolate the results acquired from wind tunnel measurements to the full scale phenomena. As mentioned earlier in the first chapter, it is an easy task to obtain identical geometric and kinematic similarity. Kinematic similarity can be achieved by equating the velocity ratios, that is, the tip speed ratios in the case of a wind turbine. The geometric similarity can be achieved by equating the ratios between dimensions. The dynamic scaling, however, cannot be satisfied in wind tunnel experiments, due to limitations in the wind tunnel facilities including the achievable wind speed, and more importantly the size of wind tunnels. Because of the size restrictions, the modeled rotors are usually smaller than the full-scale turbine by a factor of 10-100. Therefore, the Reynolds numbers corresponding to the wind tunnel experiments are usually much smaller than those of full scale wind turbines.

In this section, the radial profiles of axial velocity acquired from wind tunnel set-ups of different scales are presented. The specifications of the different experiments are presented in Table 4-1. These include rotor diameter, number of blades, tip speed ratio at which the turbine has been operated, the local chord Reynolds number and the measurement technique. Note that most of the wind turbines described in the table are horizontal axis and three bladed. The tip speed ratio is the criterion used to choose the experiments for comparison. Most of the velocity measurements in the experiments, compared herein, were conducted at tip speed ratios close to one another. Therefore, the kinematic scaling can be assumed to be satisfied. On the other hand, the local chord Reynolds number varies in different experiments. Hence, one can compare

different profiles and quantitatively assess the scaling effects, in particular the effect of Reynolds number.

<b>Descriptive Name/Year</b>	<b>Rotor Diameter (m)</b>	<b>Number of Blades</b>	<b>TSR (<math>\lambda</math>)</b>	<b>Local Chord Reynolds Number, <math>Re_c</math></b>	<b>Measurement Techniques</b>
<b>UWO (WT)</b>	2.2	3	5.67	93,000 at 0.6R	PIV
<b>MEXICO (WT)</b>	4.5	3	6.67	200,000 at 0.6R	PIV
<b>Whale et al. (1996) (WT)</b>	0.19	3	4.8	10,000	PIV
<b>Ebert and Wood (1997) (WT)</b>	0.25	2	6	255,000 at 0.75R	Hot Wires
<b>Vermeulen (1978) (WT)</b>	0.36	2	5	25,000	Hot Wires
<b>Magnusson et al. (1996) (Field)</b>	23	3	6	3,000,000 at 0.75R	Cup Anemometer System

Table 4-1: Specifications of various wind tunnel (WT) and field set-ups

Figure 4-21 (a) displays the radial profiles of normalized axial velocity deficits acquired by the present study, the MEXICO experiment and Ebert and Wood (1997). The profiles provided by UWO is obtained from the velocity measurements at  $X=0.96R$ . For the MEXICO experiment and Ebert and Wood (1997), the profiles correspond to  $X=0.2R$  and  $X=0.8R$ , respectively. The

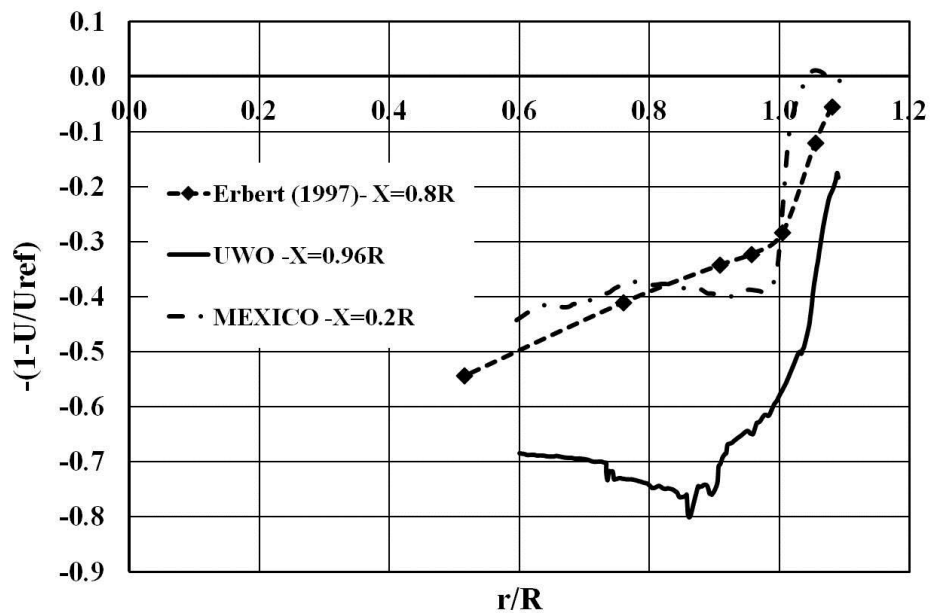
tip speed ratios corresponding to different experiments are very close in value. The profiles are circumferentially averaged.

The velocity profile acquired by Ebert and Wood (1997) shows acceptable agreement in trend, with the other two profiles, obtained from PIV measurements in large wind tunnel set-ups (UWO and MEXICO experiments). This can be attributed to the fact that measurements were performed at a relatively high wind speed of 17 m/sec, resulting in a high local chord Reynolds number of 225,000. Moreover, the magnitude of axial velocity is similar to the velocity profiles obtained by MEXICO experiment. This is despite the fact that their (Ebert and Wood's) measurements are performed in different axial locations using rotors with different number of blades.

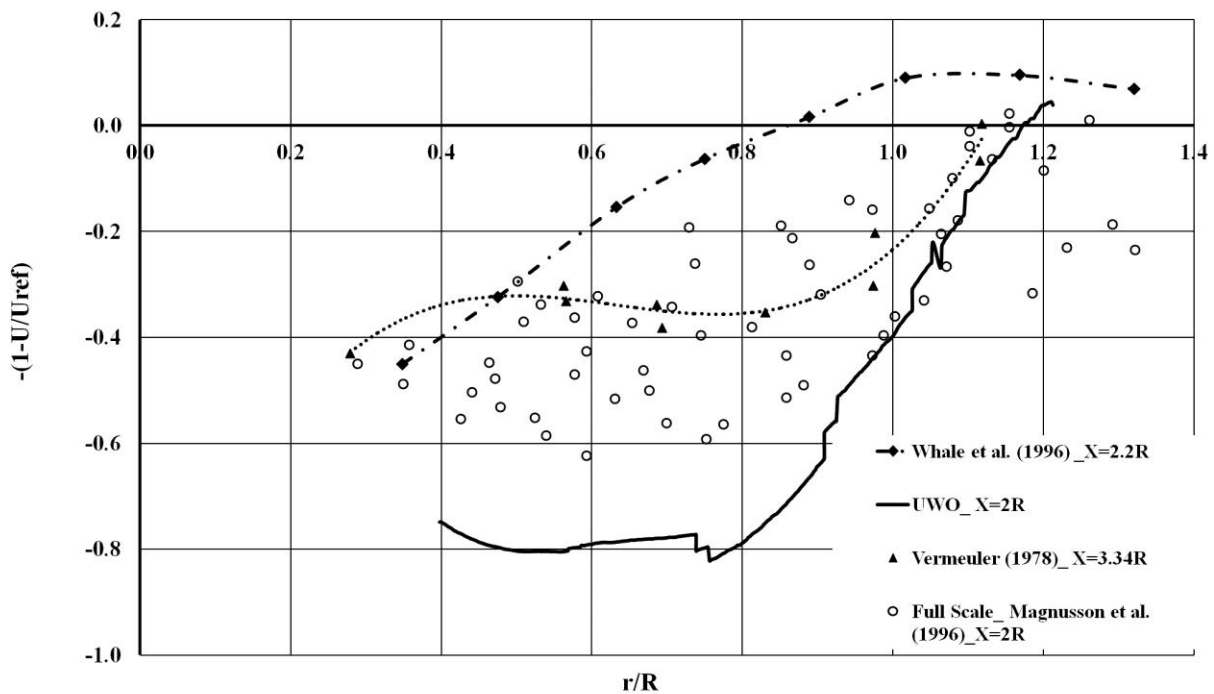
Figure 4-21 (b) presents the radial profiles of normalized axial velocity deficits acquired by present study, Whale et al. (1996), Vermeulen (1978) and Magnusson et al. (1996). The profiles are obtained from the velocity measurements at  $X > 2R$ , and are circumferentially averaged. The tip speed ratios at which the measurements are performed are in the same order of magnitude. The velocity measurements performed by Whale et al. (1996) are carried out at  $0.42R$  from the rotor centerline. The comparison between the present results and those of Whale et al. (1996) indicates that the result do not match in magnitude and in trend, particularly for  $r/R > 0.6$  where the profiles have different slopes. Also, the magnitude of axial velocity in the profile reported by Whale et al. (1996) is higher than the other profiles. A considerable difference can also be observed between the Whale et al. (1996)'s result and the profiles obtained by Vermeulen (1978). Comparison of the present results and the profile reported by Vermeulen (1978) reveals that the profiled do not match in magnitude; however, they show acceptable agreement in trend for  $r/R > 0.9$ .

The comparison between the UWO profile and the results obtained from field measurements performed by Magnusson et al. (1996) indicates that the profiles show similarity in trend. Although both profiles were obtained at same axial location downstream of the turbines, they are different in magnitude. The difference may be attributed to the fact that the full-scale rotor is performing at the tip speed ratio which is lower than its optimum; therefore, lower level of axial velocity deficit at the mid section of the blade is expected. Furthermore,  $C_T$  on the rotor for present measurements is 1.06 which is larger than the value obtained from the field measurements ( $C_T=0.82$ ). The difference may also result from the difference between upstream flow conditions. The upstream turbulence intensity for the field measurements is about 13% which is three times larger than the one for present measurements (2%).

Based on Figure 4-21, one can infer that the Reynolds number has a significant influence on the profiles of axial velocity both in trend and magnitude. One can infer that measurements with lower Reynolds numbers underestimate the magnitude of the axial velocity deficit within the wake. Therefore, it can be concluded that local chord Reynolds number can influence the velocity field with the near-wake of a horizontal axis wind turbine.



(a)



(b)

Figure 4-21: Radial profiles of normalized axial velocity acquired from different experiments presented in Table 4-1, a)  $X < R$  b)  $X > 2R$ .

## 5 Concluding Remarks

### 5.1 Conclusions

The flow structure in the near-wake region of a horizontal axis wind turbine has been studied experimentally in a large wind tunnel set-up, using PIV technique. The challenges and findings of the study are summarized in the following paragraphs:

#### 5.1.1 Challenges related to velocity measurements in the wake of a HAWT in a large wind tunnel set-up

A series of preliminary experiments were conducted, which revealed a number of technical challenges including synchronization, seeding, assembling the measurement area from smaller measurement windows and performing phase-locked measurements. The actions taken to address each of these are summarized below:

- The uniform distribution of particles and adequate particle density was a major challenge for PIV measurements in such a large wind tunnel. It was observed that seeding the entire volume of the closed-loop wind tunnel using particles generators located far from the turbine was not sufficient, and additional particles needed to be injected locally, in the region immediately behind the turbine rotor, to ensure uniform particle distribution in the PIV measurement planes.
- Another challenge in using the PIV technique for the flow field measurement in the turbine wake, was the size of the measurement area, which could not be covered by a single measurement window, and was therefore divided into smaller measurement windows.

- These windows then needed to be properly patched to construct the velocity field for the entire area of interest. It has been shown that the proper size of the overlap zone between two adjacent measurement windows and the proper calibration grid are crucial for the accurate patching of the tiles, which would ensure continuous variation of variables across the boundaries of the adjacent windows.
- To extract phase information and compute phase-averaged characteristics, the measurements needed to be phase-locked. Hence, a phase-locking technique was employed using a photo emitter/detector (E/D) device. The device provided a trigger signal for the PIV system. The appropriate time delay between the trigger signal from the device and the signal provided by the synchronizer to trigger camera and laser was defined based on the rotational speed of the rotor. Using the time delay, different angular positions of the blade were covered at each measurement window for two axial locations.

The results demonstrated that when these challenges are addressed properly, PIV can be used successfully to construct the flow field in the near-wake of a HAWT in a large wind tunnel setup. As a result of these enhancements, the present experimental program is a unique measurement campaign that enabled the characterization of both the mean and the turbulent flow fields in the near wake of a HAWT in a large wind tunnel set-up.

### **5.1.2 Mean and Turbulent Flow Field**

The mean and turbulent components of velocity have been characterized in the present experiments. Phase-locked measurements have been performed, which make it possible to extract phase information and compute phase-averaged characteristics.

- The mean velocity field shows that the maximum power extraction from the wind by the turbine, as indicated by maximum axial velocity deficit, occurs in the radial interval of



$0.7 < r/R < 0.9$ . The axial velocity reaches its maximum value at  $r/R > 1$  (a radial position larger than the physical radius of the turbine), which indicates the expansion of the wake downstream of the rotor. The profiles of radial velocity indicate that at  $X=R$  downstream of the rotor, while the radial velocity magnitude is very small in the mid section of the blade, it acquires its highest values at  $r/R > 0.9$ . The phase-averaged contour plots of the radial component of velocity show two flow patterns: inward and outward flow at  $r/R > 0.9$ , which is indicative of the presence of tip vortices in this region. The area with inward and outward flow is convected in the axial direction when the azimuth angle of the blade (represented by the phase angle) increases, this behavior indicates the helical vortex topology of the near wake.

- The axial velocity deficit and radial velocity profiles for the case of  $30^\circ$  blade azimuth angle have been compared with the results obtained in the MEXICO experiment (Schepers et al., 2012). The axial location of measurements for the MEXICO experiment is closer to the rotor, at  $X=0.2R$ . The overall trend of the velocity profiles is very similar in the two experiments. For  $r/R < 3$ , the wake is at the stage of formation where the air, as it passes through the rotor, has an outward motion tendency. Therefore, as the wake convects downstream, the air flow loses its momentum. Therefore, for larger distances downstream the turbine, within this region, one can expect to observe a larger axial velocity deficit (Sørensen and Shen, 2002; Troldborg et al., 2007) and lower radial velocity. Beyond the formation region, the velocity deficit follows the typical decreasing trend with increasing distance from the rotor. The differences in magnitude between the profiles obtained from MEXICO experiments and those obtained from present measurements clearly confirm this behavior.

- It has been found that close to the rotor, at  $X=R$ , the mean velocity components and turbulent characteristics vary considerably with respect to the phase angle, in particular at the regions affected by the tip and root vortices (i.e.  $r/R>0.9$  and  $r/R<0.6$ , respectively). The results indicate that the maximum values of turbulent components occur in the annular high-shear zone, located at  $r/R>0.9$ , which represents the region affected by the tip vortex, and separated from the freestream by a large velocity gradient. At  $X=R$  downstream the turbine, the maximum values of the axial component of turbulence intensity, the Reynolds shear stress, and turbulence kinetic energy occur at the phase angle of  $15^\circ$ . The maximum value of the radial component of turbulence intensity occurs at the phase angle of  $30^\circ$ , which coincides with the phase angle at which the maximum radial velocity is observed.
- It has also been observed that farther downstream, at  $X=2R$ , while the highest values of turbulence characteristics still occur within the shear layer, the magnitude of turbulent components reduces rapidly. In addition, at  $X=2R$  downstream of the rotor, the mean and turbulent flow components become independent of the azimuth angle of the blade. This behavior can be regarded as evidence that the helical vortex structure of the wake breaks down because of the turbulent diffusion.
- The profiles of mean and turbulent velocity components of the flow also show that the shear zone grows in the radial direction as the in the wake flow is convected in the axial direction. The diffusion of the shear zone results in the recovery of the axial velocity deficit, since the momentum transports towards the center of the rotor.

These results are particularly significant in wind farm studies, where the focus is on how fast the dissipation acts in the wind turbine wake and where the maximum shear is concentrated. Based

on the present findings, one can expect that in the far wake region (where the next turbine in the array is exposed to the wake), the turbulent characteristics, associated with each wind turbine, are independent of azimuth angle of the blade, which opens the possibility of generating simple and robust wind farm models. The finding is also important from structural point of view where the focus is on the strength of dynamic loads on the next turbine in the array. A downstream turbine experiences lower level of periodic loads while it is exposed to an upstream wake with phase independent flow structure.

### **5.1.3 Comparison with the Blade Element Momentum (BEM) method**

The circumferentially averaged axial velocity profile obtained from the PIV measurements at  $X=0.96R$  downstream of the rotor have been compared with the profiles obtained from the BEM approach at the rotor disc location. The effects of the three different types of correction applied to the classical BEM approach (Refan and Hangan, 2012) have been assessed using the results of the present experiments. The corrections are tip loss, stall delay and thrust coefficient corrections.

- It was observed that for  $r/R < 0.75$ , the results obtained using the BEM approach matched well in trend with the axial velocity profile obtained from PIV measurements, even without the corrections suggested by Refan and Hangan (2012).
- For  $r/R > 0.75$ , the similarity in the trends can only be achieved only when all corrections are applied. The quantitative difference in magnitudes between the experimental and BEM results can be attributed to the difference in axial locations at which the computational and experimental profiles are obtained. In particular, the profiles obtained from BEM method at the rotor disc location, are lower in magnitude, as expected, compared to those obtained from present measurement at  $X=0.96R$ . As observed by

previous investigations (Sørensen and Shen, 2002; Troldborg et al., 2007) and from the comparison between the present results and those obtained from MEXICO experiments, for  $r/R < 3$ , the axial velocity deficit increases as the wake convects downstream indicating that closer to the rotor the wake is still at the formation stage.

#### 5.1.4 Scaling Effects

The profiles of the axial velocity deficits have also been compared with the results obtained from the velocity measurements performed by previous investigators in small wind tunnel set-ups, in order to assess the scaling effects. Based on the kinematic similarity arguments presented in section 1.2.1, tip speed ratio was the criterion used to select experiments for comparison. Most of the velocity measurements were conducted at almost similar tip speed ratios. Therefore, the kinematic scaling was satisfied. On the other hand, the local chord Reynolds number varied in different experiments. The profiles were circumferentially averaged and plotted for  $X < R$  and  $X > 2R$ .

- For  $X < R$ , The axial velocity profile provided by Ebert and Wood (1997) showed a good agreement with the results obtained from PIV measurements in large wind tunnel setup, particularly the MEXICO results (Schepers et al., 2012). The reason can be the high Reynolds number at which Ebert and Wood (1997)'s measurements were performed.
- For  $X > 2R$ , the profiles obtained from different measurements (Whale et al., 1996; Vermeulen, 1978) did not match well; however, for  $r/R > 0.9$  the results provided by Vermeulen (1978) showed a good agreement in trend with the profile obtained from the present PIV measurements. The results obtained from field measurements (Magnusson et al., 1996) show similarity in trend with those acquired from present measurements. The difference in magnitude results from the fact that the full-scale rotor is performing at the

tip speed ratio lower than its optimum. Also, the difference may be associated with the difference between upstream flow conditions of the measurements in particular upstream turbulence intensities as well as the thrust coefficients over the rotors.

Overall, the comparison indicated that the mean flow field, represented in this comparison by axial velocity profiles, is highly dependent on the Reynolds number. One can infer that measurements with lower Reynolds numbers underestimate the magnitude of the axial velocity deficit within the wake.

To summarize, the main contributions of the present study to the knowledge of the flow in the wake of horizontal axis wind turbines are:

- Investigating and explaining the turbulent flow field of the near-wake region of a HAWT in a large wind tunnel set-up.
- Experimental identification and description the vortex flow dynamics in the near-wake region of a HAWT in a large wind tunnel set-up.

The partial contributions of the present study to research are:

- Enhancing the Particle Image Velocimetry (PIV) technique for velocity measurements for rotating wakes in large wind tunnel set-ups in terms of synchronization, seeding, window assembling and performing phase-locked measurements.
- Providing experimental data to assess the scaling effects for HAWT.
- Evaluating the classical BEM approach and the recently-developed corrections to the classical method using experimental data.

## 5.2 Future Work

Based on the findings and observation, the following recommendations can be made to extend and complement the present research in the future:

- To conduct experiments in test conditions more closely representative of the conditions experienced by full-scale wind turbines, including existence of an atmospheric boundary layer (ABL) upstream the turbine, and the turbulence levels representative of the atmospheric upstream flow.
- To conduct controlled experiments with various scales while everything else remains unchanged, to single out the scaling effects among all of the parameters affecting the flow. Scaling effects need to be determined in order to extrapolate the wind tunnel results to the full scale phenomena.
- In addition, the data obtained from the phase-locked PIV measurements in different axial location for different azimuth angles can be used as benchmark for CFD simulations. This can contribute to improvement of the numerical models (including turbulence closure schemes) used in CFD simulation, and can therefore lead to more accurate simulation of the turbine aerodynamics and the turbulence characteristics of the wake, for the analysis of wind turbine interactions in a wind farm.

## REFERENCES

- Adrian, R. J., 1991: Particle-imaging techniques for experimental fluid mechanics, *Ann. Rev. Fluid Mech.*, 23, 261-304.
- Alan, G. Davenport Wind Engineering Group, 2007, *Wind Tunnel Testing*, The Boundary Layer Wind Tunnel Laboratory, London, ON.
- Alino, C. and C., Masson, 2002: Aerodynamic simulations of wind turbines operating in atmospheric boundary layer with various thermal stratifications, A collection of the 2002 ASME wind energy symposium technical papers, pp 206–215.
- Ammara, I., C. Leclerc, and C. Masson, 2002: A viscous three-dimensional differential/actuator-disk method for the aerodynamic analysis of wind farms, *J. Sol. Energy Eng.*, 124:345–356.
- Bechmann, A. and N. Sørensen, 2009: CFD simulation of the MEXICO rotor wake, In European Wind Energy Conference and Exhibition, Marseille.
- Betz, A., 1919: Schraubenpropeller mit geringstem energieverlust. *Göttinger Nachr*, Germany.
- Burton, T., Sharpe, D., Jenkins, N. and Bossanyi, E., 2001: *Wind Energy Handbook*, John Wiley & Sons Ltd.
- Calaf, M., C. Meneveau and J. Meyers, 2010: Large eddy simulation study of fully developed wind-turbine array boundary layers, *Phys. Fluids*, 23, 126603.
- <http://www.canwea.ca/>, 2008.
- Crespo, A. and J. Hernandez, 1996: Turbulence characteristics in wind-turbine wakes, *J. Wind Eng. Ind. Aerodyn.*, 61:71–85.

Chamorro, L. P., M. Guala, R.E.A. Arndt and F. Sotiropoulos, 2012: On the evolution of turbulent scales in the wake of a wind turbine model, *J. Turbulence*, Vol. 13, No. 27, 1–13.

Cowen, E. A. and Monismith S. G., 1997: A hybrid digital particle tracking Velocimetry technique, *Exp. Fluids*, 22, 199-211.

Dobrev, I., B. Maalouf, N. Troldborg, F. Massouh, 2008: Investigation of the wind turbine vortex structure, 14<sup>th</sup> Int. Symp. On Applications of Laser Techniques to Fluid Mechanics, Lisbon, Portugal.

Ebert, R. and D. H. Wood, 1997: The Near Wake of a Model Horizontal-Axis Wind Turbine-I. Experimental Arrangements and Initial Results, *Renewable Energy*, Vol. 12, No. 3: 225-243.

Fletcher T. M. and R. E. Brown, 2010: Simulation of wind turbine wake interaction using the vorticity transport model, *Wind Energy*, 13: 587–602.

Glauert, H., 1935: *Airplane Propellers. Aerodynamic Theory*, Springer Verlag, Berlin (reprinted by Peter Smith, Gloucester, MA, 1976).

Gómez-Elvira, R, Crespo A, Migoya E, Manuel F, Hernández J (2005) Anisotropy of turbulence in wind turbine wakes, *J. Wind Eng. Ind. Aerodyn.*, 93:797–814.

Grant, I., and P. A. Parkin, 2000: DPIV study of the trailing vortex elements from the blades of a horizontal axis wind turbine in yaw, *Exp. Fluids*, Vol. 28: 368-376.

Grant, I., M. Mo, X. Pan, P. Parkin, J. Powell, H. Reinecke, K. Shuang, F. Coton, D. Lee, 1998: optical evaluation of the wake characteristics of a wind turbine and a prescribed wake model, paper 172, Proc 8<sup>th</sup> Int. Symp. on Flow visualization, Naples, Scotland.



Grant, I., G. Smith, A. Liu, D. In field, T. Eich, 1991: Particle Image Velocimetry measurements of the aerodynamics of a wind turbine, Int. Congr. on Instr. in Aero. Sim. Facil. Rockville IEEE.

Hamburg, M., 1970: Statistical analysis for decision making, Harcourt, Brace and World.

Hansen, M. and H. Madsen, 2011: Review Paper on Wind Turbine Aerodynamics, J. Fluids Eng., 133, 114001-1.

Hansen, M. O. L., 2008: Aerodynamics of Wind Turbines, EARTHSCAN, London.

Hansen, A. C. and C. P. Butterfield, 1993: Aerodynamics of Horizontal-Axis Wind Turbines, Annual Reviews Fluid Mechanics, 25: 115-49.

Helmis, C.G., K. H. Papadopoulos, D. N. Asimakopoulos, P. G. Papageorgas and A. T. Soilemes, 1995: An experimental study of the near-wake structure of a wind turbine operating over complex terrain, Solar Energy, 54: 413-428.

Himmelskamp, H., 1945: Profile investigations on a rotating airscrew, Ph.D. Thesis, Gottingen University, Germany.

Hojstrup, J., 1990: Wake measurements on the Nibe wind turbines in Denmark, Appendix 1, Nibe wake 2: Data report- power spectra, Final Report on CEC Contract No. EN3W.0039.UK (H1).

Ivanell, S., J. N. Sørensen, R. Mikkelsen and D. Henningson, 2009: Analysis of numerically generated wake structures, Wind Energy, 12:63–80.

Jimenez, A, A. Crespo, E. Migoya and J. Garcia, 2008: Large-eddy simulation of spectral coherence in a wind turbine wake, Environ. Res. Lett., 3:015004.

Jimenez, A., A. Crespo, E. Migoya and J. Garcia, 2007: Advances in large-eddy simulation of a wind turbine wake, *J. Phys. Conf.*, Ser. 75:012041.

Kasmi, A. and C. Masson, 2008: An extended k- $\epsilon$  model for turbulent flow through horizontal-axis wind turbines, *J. Wind Eng. Ind. Aerodyn.*, 96:103–122.

Krogstad, P. and M. S. Adaramola, 2012: Performance and near wake measurements of a model horizontal axis wind turbine, *Wind Energy*, 15, 743-756.

Loth, E., 2000: Numerical approaches for motion of dispersed particles, droplets, and bubbles, *Progress in Energy and Combustion Science*, 26, 161-223.

Magnusson, M., 1999: Near-wake behaviour of wind turbines, *J. Wind Eng. Ind. Aerodyn.*, 80, 147-167.

Magnusson, M., K. G. Rados and S. G. Voutsinas, 1996: A study of the flow downstream of wind turbine using measurements and simulations, *Wind Eng.*, 20 (6): 389–403.

Manwell, J. F., J. G. McGowan and A. L. Rogers, 2002: *Wind Energy Explained Theory, Design and Application*, John Wiley & Sons Ltd.

Massouh, H and I. Dobrev, 2007: Exploration of the vortex behind of wind turbine rotor, *J. Phys. Conf.*, Ser. 75:012036.

Papadopoulos, K.H., C. G. Helmis, A. T. Soilemes, P. G. Papageorgas and D. N. Asimakopoulos, 1995: Study of the turbulent characteristics of the near-wake field of a medium-sized wind turbine operating in high wind conditions, *Solar Energy*, 55: 61-72.

Piirto, M., P. Saarenrinne, H. Eloranta and R. Karvinen, 2003: Measuring turbulence energy with PIV in a backward facing step flow, *Experiments in Fluids*, 35, 219-236.

Pope S.B., 2000: *Turbulent Flows*, Cambridge: Cambridge University Press.

Prasad, A. K., R. J. Adrian, C. C. Landreth and P. W. Offutt, 1992: Effect of resolution on the speed and accuracy of particle image velocimetry interrogation, *Exp. Fluids*, 13, 105-116.

Refan, M. and H. Hangan, 2012: Aerodynamic performance of a small horizontal axis wind turbine, *Sol. Energy Eng.*, 134, 021013 (7 pages).

Refan, M., 2009: Aerodynamic performance of a small horizontal axis wind turbine, Master's thesis, Department of Mechanical Eng., Western University.

Ronsten, G., 1991: Static pressure measurements in a rotating and a non rotating 2.35 wind turbine blade, *Proceedings of the EWEC Conference*.

Sanderse, B., S. P. van der Pijl and B. Koren, 2011: Review of computational fluid dynamics for wind turbine wake aerodynamics, *Wind Energy*, 14:799–819.

Schepers, J.G., K. Boorsma, T. Cho, S. Gomez-Iradi, P. Schaffarczyk, A. Jeromin, W.Z. Shen, T. Lutz, K. Meister, B. Stoevesandt, S. Schreck, D. Micallef, R. Pereira, T. Sant, H.A. Madsen and N. Sørensen, 2012: Analysis of Mexico wind tunnel measurements, Final report of IEA Task 29, Mexnext (Phase 1).

Schreck, S., J. Lundquist and W. Shaw, 2008: U. S. Department of Energy Workshop Report: Research needs for wind resource characterization, National Renewable Energy Laboratory Technical Report, NREL/TP-500-43521.

Schreck, S., 2002: The NREL full-scale wind tunnel experiment introduction to the special issue, *Wind Energy*, 5 (2–3), 77–84.

Shen, W. Z., J. H. Zhang and J. N. Sørensen, 2009: The Actuator Surface Model: A New Navier–Stokes Based Model for Rotor Computations, *J. of Solar Energy Eng.*, 131, 011002-1-9.

Siddiqui, K., 2002: Laboratory measurement of the flow beneath micro scale breaking waves, PhD thesis, Department of Mechanical and Industrial Eng., University of Toronto.

Siddiqui, M. H. K., M. R. Loewen, C. Richardson, W. E. Asher and A. T. Jessup, 2001: Simultaneous particle image velocimetry and infrared imagery of microscale breaking waves, *Phys. Fluids*, 13, 1891–903.

Siddiqui, M. H. K., H. Hangan and A. Rasouli, 2008: PIV technique implementation for wind mapping in complex topographies, *Mea. Sci. Technol.*, 19, 065403 (11pp).

Smith, D., and G. J. Taylor, 1991: Further analysis of turbine wake development and interaction data. In: Q.D.C., F. V. C, editors, *Proceedings of the 13th BWEA Wind Energy Conference*, Swansea, UK, 1991, 325–31.

Snel, H., J G Schepers and B Montgomerie, 2007: The MEXICO Project (Model Experiments in Controlled Conditions): The Database and First Results of Data Processing and Interpretation, *J. of Physics: Conference Series* 75.

Snel, H. et al., 1993: Sectional prediction of three-dimensional effects for stalled flow on rotating blades and comparison with measurements, *Proceedings of the EWEC Conference*.

Sørensen, N. N., J. A. Michelsen and S. Schreck, 2002: Navier-Stokes predictions of the NREL Phase VI Rotor in the NASA Ames 80-by-120 Wind Tunnel, Report No. AIAA-2002-0032.

Sørensen, JN. and WZ. Shen, 2002: Numerical modeling of wind turbine wakes, *J. Fluid Eng.*, 124 (2), 393-9.

Sørensen, JN., WZ. Shen and X. Mundate, 1998: Analysis of wake states by a full-field actuator disc model, *Wind Energy*, 1:73–88.

Sørensen, JN. and CW. Kock, 1995: A model for unsteady rotor aerodynamics, *J. Wind Eng. Ind. Aerodyn.*, 58:259–275.

Troldborg, N., JN. Sorensen and R. Mikkelsen, 2009: Numerical Simulations of Wake Characteristics of a Wind Turbine in Uniform Inflow, *Wind Energy*, 13, 86-99.

Tom, K., 2010: Investigation of Near Wake Flow Structure of a Horizontal Axis Wind Turbine Using Particle Image Velocimetry. Masters thesis, Concordia University.

Troldborg, N., JN. Sørensen and R. Mikkelsen, 2007: Actuator line simulation of wake of wind turbine operating in turbulent inflow, *J. Phys. Conf.*, Ser. 75:012063.

Vermeer, L. J., J. N. Sorensen and A. Crespo, 2003: Wind turbine wake aerodynamics, *Aerospace Sciences*, 39, 467-51.

Vermeulen, P., 1978: A wind tunnel study of the wake of a horizontal axis wind turbine, Technical report 78-09674, TNO, 's Gravenhage, The Netherlands.

Watters, C. S. and C. Masson, 2007: Recent advances in modeling of wind turbine wake vortical structure using a differential actuator disk theory, *The Science of Making Torque from Wind*, J. Physics: Conference Series, 75: 012037.

Whale, J., C.G. Anderson, R. Bareiss and S. Wagner, 2000: An experimental and numerical study of the vortex structure in the wake of a wind turbine, *J. Wind Eng. Ind. Aerodyn.*, 84: 1-21.

Whale, J., K. H. Papadopoulos, C. G. Anderson, C. G. Helmis and D. J. Skyner, 1996: A study of the near wake structure of a wind turbine comparing measurements from laboratory and full-scale experiments, *Solar Energy*, 56 (6), 621-633.

Wu, Y. T. and F. Porté-Agel, 2011: Large-Eddy Simulation of Wind-Turbine Wakes: Evaluation of Turbine Parameterizations, *Boundary-Layer Meteorol*, 138:345–366.

Xiao, J., J. Wu, L. Chen and Z. Shi, 2011: Particle Image Velocimetry (PIV) measurements of tip vortex wake structure of wind turbine, *Appl. Math. Mech. -Engl. Ed.*, 32(6), 729–738.

Yang, Z., P. Sarkar and H. Hu, 2011: An experimental investigation on the wake characteristics of a wind turbine in an atmospheric boundary layer wind, 29th AIAA Applied Aerodynamics Conference, Honolulu, Hawaii.

## CURRICULUM VITAE

<b>Name</b>	Pooyan Hashemi Tari
<b>Academic Background</b>	<p>AmirKabir University of Technology (Tehran Polytechnic), Tehran, Iran Bachelor of Science in Fluid Mechanics, 1999 – 2005</p> <p>AmirKabir University of Technology (Tehran Polytechnic), Tehran, Iran Bachelor of Science in Solid &amp; Design Mechanics, 1999 – 2005</p> <p>University of Western Ontario (UWO), London, Ontario, Canada Master of Engineering Science in Civil and Environmental Eng., 2006-2008</p> <p>University of Western Ontario (UWO), London, Ontario, Canada Doctor of Philosophy in Civil and Environmental Eng., 2008-2012</p>
<b>Honors and Awards</b>	<p>Western Graduate Research Scholarship, 2006, 2007, 2008, 2009, 2010</p> <p>Ontario Graduate scholarship (OGS), 2011-2012.</p>
<b>Related Work Experience</b>	<p>University of Western Ontario (UWO) Teaching Assistant, 2006-2012</p>
<b>Conference Proceeding</b>	<p>Hashemi Tari, P., H. Hangan and K. Siddique 2012: PIV Measurement in the Wake of a Small Horizontal Axis Wind Turbine (HAWT), 1000 Islands Fluid Conference, Kingston, Ontario.</p> <p>Hangan, H., P. Hashemi Tari and J. Kim, 2008: Modeling of High Intensity Winds, 18th Analysis and Computation Specialty Conference, Vancouver, BC, Canada; Sponsored by the Structural Engineering Institute (SEI) of the American Society of Civil Engineers.</p> <p>Hashemi Tari, P., R. Gurka and H. Hangan, 2007: Swirl ratio effects on tornado-like vortex vortices, 60th Meeting of the Division of Fluid Dynamics, Salt lake city, Utah.</p> <p>Hashemi Tari, P., H. Hangan, 2006: Tornado vortex simulator. Preliminary surface pressure measurements. 1000 Islands Fluid Conference, Kingston, Ontario.</p>

**Publications**

Hashemi Tari P., R. Gurka and H. Hangan, 2010: Experimental investigation of tornado-like vortex dynamics with Swirl Ratio: The mean and turbulent flow fields, *J. Wind Eng. Ind. Aerodyn.*, 98: 936–944.